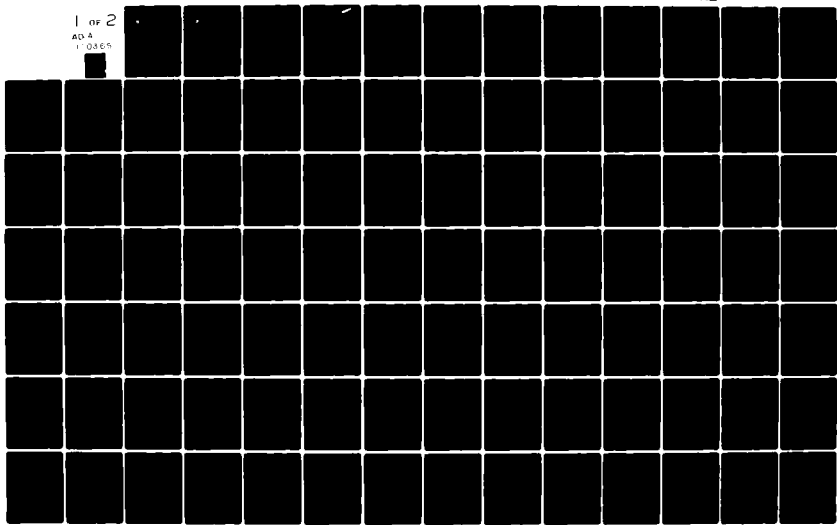


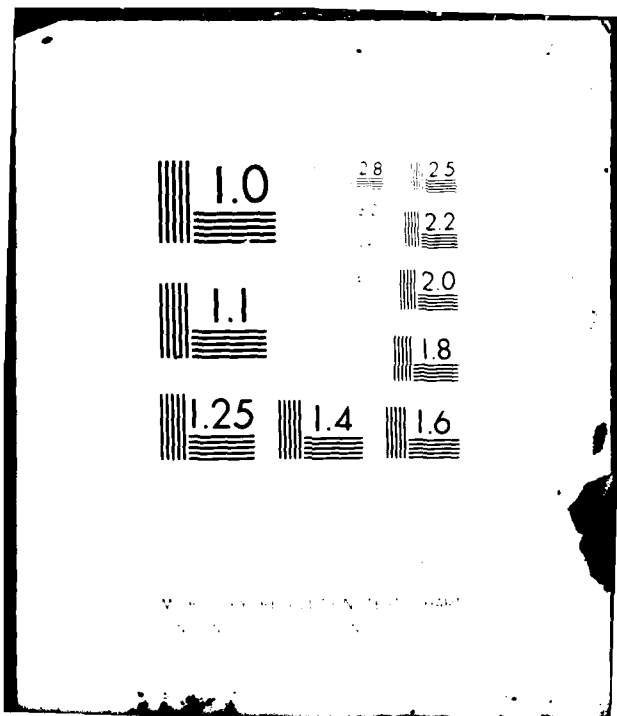
AD-A110 365 AIR FORCE INST OF TECH WRIGHT-PATTERSON AFB OH
DIGITAL METEOROLOGICAL RADAR DATA COMPARED WITH DIGITAL INFRARE--ETC(U)
MAY 79 R S HENDERSON
UNCLASSIFIED AFIT-CI-79-278T-S

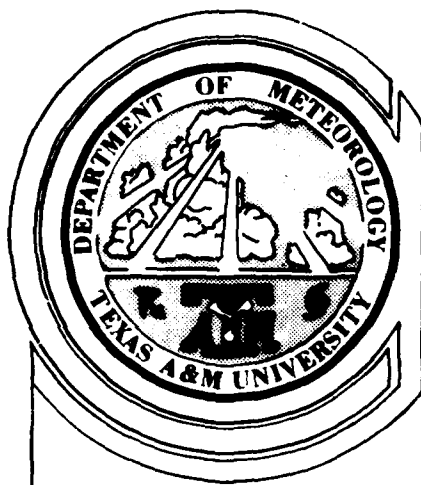
F/6 4/2

NL

1 of 2
AD A
1-0465







79-278T-S

(1)

TEXAS A&M UNIVERSITY

DEPARTMENT OF
METEOROLOGY

AD A110365

DIGITAL METEOROLOGICAL RADAR DATA COMPARED
WITH DIGITAL INFRARED DATA FROM A
GEOSTATIONARY METEOROLOGICAL SATELLITE

by

Rodney S. Henderson

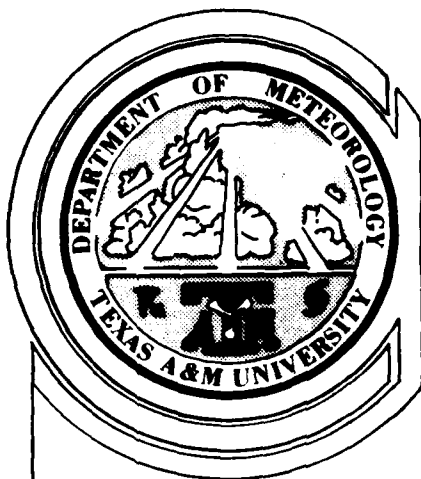
May 1979

DTIC
ELECTED
FEB 3 1982
S D

DTIC FILE COPY

DISTRIBUTION STATEMENT A
Approved for public release
Distribution Unlimited





TEXAS A&M UNIVERSITY

DEPARTMENT OF METEOROLOGY

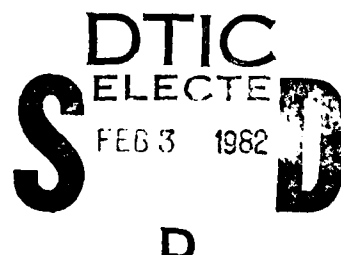
DIGITAL METEOROLOGICAL RADAR DATA COMPARED
WITH DIGITAL INFRARED DATA FROM A
GEOSTATIONARY METEOROLOGICAL SATELLITE

by

Rodney S. Henderson

May 1979

Accession For	
NTIS GRAF	<input checked="" type="checkbox"/>
DTIC TAB	<input type="checkbox"/>
Unannounced	<input type="checkbox"/>
Justification	
By	
Distribution/	
Availability Codes	
Dist	Avail and/or Special
A	



DISTRIBUTION STATEMENT A
Approved for public release;
Distribution Unlimited



UNCLASS

SECURITY CLASSIFICATION OF THIS PAGE (Block 10a, If different from Block 1)

AFIT- REPORT DOCUMENTATION PAGE

1. REPORT NUMBER 79-278T-S		2. GOVT ACCESSION NO. 47-2943365	3. READ INSTRUCTIONS BEFORE COMPLETING FORM 4. RECIPIENT'S CATALOG NUMBER
4. TITLE (and Subtitle) Digital Meteorological Radar Data Compared With Digital Infrared Data From a Geostationary Meteorological Satellite		5. TYPE OF REPORT & PERIOD COVERED THESIS/DISSERTATION	
7. AUTHOR(S) Capt Rodney Stuart Henderson		6. PERFORMING ORG. REPORT NUMBER	
9. PERFORMING ORGANIZATION NAME AND ADDRESS AFIT STUDENT AT: Texas A&M University		10. PROGRAM ELEMENT, PROJECT, TASK AREA & WORK UNIT NUMBERS	
11. CONTROLLING OFFICE NAME AND ADDRESS AFIT/NR WPAFB OH 45433		12. REPORT DATE May 1979	
14. MONITORING AGENCY NAME & ADDRESS (if different from Controlling Office)		13. NUMBER OF PAGES 116	
16. DISTRIBUTION STATEMENT (of this Report) APPROVED FOR PUBLIC RELEASE; DISTRIBUTION UNLIMITED		15. SECURITY CLASS (of this report) UNCLASS	
17. DISTRIBUTION STATEMENT (of the abstract entered in Block 20, if different from Report)		15a. DECLASSIFICATION DOWNGRADING SCHEDULE	
18. SUPPLEMENTARY NOTES APPROVED FOR PUBLIC RELEASE: IAW AFR 190-17		22 JAN 1982 <i>Fredric C. Lynch</i> FREDRIC C. LYNCH, Major, USAF Director of Public Affairs Air Force Institute of Technology (ATC) Wright-Patterson AFB, OH 45433	
19. KEY WORDS (Continue on reverse side if necessary and identify by block number)			
20. ABSTRACT (Continue on reverse side if necessary and identify by block number)			
ATTACHED			
82 02 01 085			

TEXAS A&M UNIVERSITY
COLLEGE OF GEOSCIENCES
COLLEGE STATION, TEXAS 77843

79-278 T-S

23 April 1979

Reply to
Department of
METEOROLOGY/Capt Henderson
Telephone (713) 845-6011

AFIT/CIRF
Wright-Patterson AFB

The following information is submitted as required by AFITR
53-1:

- a. Author/Title: Rodney Stuart Henderson,
Digital Meteorological Radar Data Compared
With Digital Infrared Data From a Geostationary
Meteorological Satellite.
- b. Rank/Service: Capt, USAF.
- c. Year: 1979.
- d. Number of Pages: 116.
- e. Degree: M.S./Meteorology, Texas A&M University.
- f. Abstract:

Digital 10 cm radar data were collected using the Texas A&M University weather radar system. The digital radar data were then compared with GOES-East infrared imagery mapped to the digital radar grid projection. Point values of infrared digital count were correlated with point values of zero-tilt reflectivity, low-level PVSZ, mid-level PVSZ, upper-level PVSZ, and VIL for selected portions of two digital radar tilt-sequences. Correlations were also performed using thresholded infrared images and thresholded digital radar data.

The results indicated a positive correlation between infrared digital count and the digital radar data. Thresholding the infrared imagery was found to improve the correlation between infrared digital count and digital radar data. Thresholding the digital radar data produced less conclusive results.

- g. A list of key primary and secondary sources is attached.

Rodney S. Henderson
RODNEY S. HENDERSON, Capt, USAF

Atch:
References.

Subject: Thesis Abstract.

REFERENCES

Adler, R.F., and D.D. Fenn, 1977: Satellite-based thunderstorm intensity parameters. Preprints 10th Conf. on Severe Local Storms, Omaha, Amer. Meteor. Soc., 8-15.

Blackmer, R.H., Jr., 1961: Satellite observations of squall line thunderstorms. Proc. 9th Radar Meteor. Conf., Kansas City, Amer. Meteor. Soc., 76-82.

—, 1975: Correlation of cloud brightness and radiance with precipitation intensity. Tech. Rpt. NEPRF TR 8-75(SRI), Contract N66314-74-C-2350, Stanford Research Institute, 134 pp.

—, and S.M. Serebreny, 1968: Analysis of maritime precipitation using radar data and satellite cloud photographs. J. Appl. Meteor., 7, 122-131.

Boucher, R.J., 1967: Relationships between the size of satellite-observed cirrus shields and the severity of thunderstorm complexes. J. Appl. Meteor., 6, 564-572.

Cheng, N., and D. Rodenhuis, 1977: An intercomparison of satellite images and radar rainfall rates. Preprints 11th Technical Conf. on Hurricanes and Tropical Meteorology, Miami Beach, Amer. Meteor. Soc., 224-226.

Fujita, T.T., 1977: Meteorological satellite observations and army operations. Tech. Rpt. ECOM 77-6, University of Chicago, 37 pp.

Gerrish, H.P., 1970: Satellite and radar analysis of mesoscale features in the tropics. Tech. Rpt. ECOM-0205-F, University of Miami, 45 pp.

—, 1975: Satellite and radar analysis of mesoscale weather systems. Tech. Rpt. ECOM-0014-F, University of Miami, 34 pp.

Griffith, C.G., and W.L. Woodley, 1973: On the variation with height of the top brightness of precipitating convective clouds. J. Appl. Meteor., 12, 1086-1089.

—, W.L. Woodley, P.G. Grube, D.W. Martin, J. Stout, and D.N. Sikdar, 1978: Rain estimation from geosynchronous satellite imagery - visible and infrared studies. Mon. Wea. Rev., 106, 1153-1171.

Gruber, A., 1973: Estimating rainfall in regions of active convection. J. Appl. Meteor., 12, 110-118.

Nagle, R.E., 1963: Comparisons of time integrated radar detected precipitation with satellite observed cloud patterns. Proc. 10th Radar Meteor. Conf., Washington, Amer. Meteor. Soc., 13-16.

—, and S.M. Serebreny, 1962: Radar precipitation echo and satellite cloud observations of a maritime cyclone. J. Appl. Meteor., 1, 279-295.

Negri, A.J., D.W. Reynolds, and R.A. Maddox, 1976: Measurements of cumulonimbus clouds using quantitative satellite and radar data. Proc. 7th Conf. on Aerospace and Aeronautical Meteor. and Symp. on Remote Sensing from Satellites, Melbourne, Amer. Meteor. Soc., 119-124.

Phillips, J.F., 1975: Cloud structures from Defense Meteorological Satellite data. M.S. thesis, Texas A&M University, 142 pp.

Reynolds, D.W., 1978: An intensive analysis of digital radar, raingage, and digital satellite data for a convective cloud system on the High Plains of Montana. Preprints 4th Symp. on Meteorological Observations and Instrumentation, Denver, Amer. Meteor. Soc., 310-317.

—, and T.H. Vonder Haar, 1973: A comparison of radar-determined cloud height and reflected solar radiance measured from the geosynchronous satellite ATS-3. J. Appl. Meteor., 12, 1082-1085.

—, T.H. Vonder Haar, and L.O. Grant, 1978: Meteorological satellites in support of weather modification. Bull. Amer. Meteor. Soc., 59, 269-281.

Sieland, T.E., 1977: Real-time computer techniques in the detection and analysis of severe storms from digital radar data. Ph.D. dissertation, Texas A&M University, 141 pp.

Sikdar, D.N., 1972: ATS-3 observed cloud brightness field related to a meso-synoptic scale rainfall pattern. Tellus, 24, 400-413.

Smith, E.A., and D.W. Reynolds, 1978: The generation and display of digital radar-satellite composites using analytic mapping techniques and solid state video refresh technology. Preprints Conf. on Wea. Forecasting and Analysis and Aviation Meteor., Silver Spring, Amer. Meteor. Soc., 201-205.

Vonder Haar, T.H., 1969: Meteorological applications of reflected radiance measurements from ATS 1 and ATS 3. J. Geophys. Res., 74, 5404-5412.

—, and R.S. Cram, 1970: A pilot study on the application of geosynchronous meteorological satellite data to very short range terminal forecasting. Tech. Rpt. AFCRL 70-0493, Space Science and Engineering Center, University of Wisconsin, 116 pp.

Wexler, R., and L.J. Allison, 1972: Radar and Nimbus IV infrared measurements of the Oklahoma City tornadoes, 30 April 1970. Preprints 15th Radar Meteor. Conf., Champaign-Urbana, Amer. Meteor. Soc., 77-82.

DIGITAL METEOROLOGICAL RADAR DATA COMPARED
WITH DIGITAL INFRARED DATA FROM A
GEOSTATIONARY METEOROLOGICAL SATELLITE

A Thesis

by

RODNEY STUART HENDERSON

Submitted to the Graduate College of
Texas A&M University
in partial fulfillment of the requirement for the degree of

MASTER OF SCIENCE

May 1979

Major Subject: Meteorology

DIGITAL METEOROLOGICAL RADAR DATA COMPARED
WITH DIGITAL INFRARED DATA FROM A
GEOSTATIONARY METEOROLOGICAL SATELLITE

A Thesis

by

RODNEY STUART HENDERSON

Approved as to style and content by:

George E. Huebner
(Chairman of Committee)

Aylmer W. Thompson
(Member)

Karen Moyer
(Member)

John Sherrill
(Member)

K.C. Brundidge
(Head of Department)

May 1979

ABSTRACT

Digital Meteorological Radar Data Compared with
Digital Infrared Data from a Geostationary
Meteorological Satellite. (May 1979)

Rodney Stuart Henderson, B.A.E.,
Georgia Institute of Technology

Chairman of Advisory Committee: Dr. George Huebner

↓
Digital 10 cm radar data were collected using the Texas A&M University weather radar system. The digital radar data were then compared with GOES-East infrared imagery mapped to the digital radar grid projection. Point values of infrared digital count were correlated with point values of zero-tilt reflectivity, low-level PVSZ, mid-level PVSZ, upper-level PVSZ, and VIL for selected portions of two digital radar tilt-sequences. Correlations also were performed using thresholded infrared images and thresholded digital radar data.

The results indicated a positive correlation between infrared digital count and the digital radar data. Thresholding the infrared imagery was found to improve the correlation between infrared digital count and digital radar data. Thresholding the digital radar data produced less conclusive results.

ACKNOWLEDGMENTS

The author's graduate program was sponsored and financed by the Air Force Institute of Technology, United States Air Force.

I wish to express sincere appreciation to the following individuals whose guidance and assistance have made this endeavor possible:

Dr. George Huebner, my committee chairman, for his encouragement, advice, and support throughout this program.

Dr. Aylmer Thompson, for serving patiently on my committee and for his many contributions to the development of this study.

Dr. Vance Moyer, for serving on my committee and for his support and assistance in developing this manuscript and others.

Dr. Glen Williams, for serving on my committee and reviewing this manuscript.

Mr. J. T. Young of the Space Science and Engineering Center, University of Wisconsin, for providing the satellite data and advice regarding its use.

Mr. Ray McAnelly, for his generation of the digital radar data used in this study.

Mr. T. O. Haig, also of the Space Science and Engineering Center, for information on the McIDAS system.

Mrs. Jane Kraft for her patience and efforts in typing this
manuscript.

DEDICATION

To my wife, Sandra, whose patience and understanding have made this thesis possible, and to my sons, Bryan and Jeremy, for their support and encouragement.

TABLE OF CONTENTS

	Page
ABSTRACT	iii
ACKNOWLEDGMENTS	iv
DEDICATION	vi
TABLE OF CONTENTS	vii
LIST OF TABLES	ix
LIST OF FIGURES	x
LIST OF ACRONYMS	xii
CHAPTER	
I. INTRODUCTION	1
1. The Need for This Investigation	1
2. Present Status of Research Relating to This Investigation	3
3. Objectives of the Investigation	7
4. Techniques and Scope of the Investigation	8
II. METEOROLOGICAL RADAR DATA	10
1. Basic Radar Theory	10
2. Earth Curvature Correction	13
3. The TAMU Weather Radar System	15
4. Data Reduction and Display	17
III. GEOSTATIONARY METEOROLOGICAL SATELLITE DATA	20
1. The SMS/GOES Spacecraft	20
2. The Visible and Infrared Spin Scan Radiometer	22
3. Data Distribution and Processing	23

TABLE OF CONTENTS (Continued)

CHAPTER	Page
4. Basic Characteristics of Infrared Satellite Data	26
5. McIDAS Data	27
6. Data Reduction and Display	29
IV. COMPARISON OF DIGITAL RADAR AND SATELLITE DATA	38
1. The Basis for the Comparison	38
2. First Tilt-sequence and Corresponding GOES Images	40
3. Tenth Tilt-sequence and Corresponding GOES Images	50
4. Correlations Between the Radar and Satellite Data	66
5. The Effect of Thresholding the Data	71
V. CONCLUSIONS AND RECOMMENDATIONS	83
1. Conclusions	83
2. Recommendations	86
REFERENCES	90
APPENDIX A	94
VITA	103

LIST OF TABLES

TABLE	Page
1 Displacement corrections for cloud height	36
2 Displacement correction for each image	37
3 Values of r and p for the first tilt-sequence and corresponding GOES images	68
4 Values of r and p for the tenth tilt-sequence and corresponding GOES images (southwest sector)	70
5 Values of r and p for the tenth tilt-sequence and corresponding GOES images (northwest sector)	72
6 MB enhancement (after Corbell <i>et al.</i> , 1976)	75
7 Values of r and p for the first tilt-sequence and thresholded GOES images	77
8 Values of r and p for thresholded radar data and GOES images	80

LIST OF FIGURES

FIGURE	Page
1 SMS/GOES Data Distribution.	25
2 Navigated points and mapping to the digital radar grid	32
3 Tilt-sequence one, zero-tilt reflectivity (dBZ)	41
4 Tilt-sequence one, low-level PVSZ (dBZ)	42
5 Tilt-sequence one, mid-level PVSZ (dBZ)	43
6 Tilt-sequence one, upper-level PVSZ (dBZ)	44
7 Tilt-sequence one, VIL (kg m ⁻²)	45
8 0015 GMT, 3 May 1978 infrared image.	46
9 0030 GMT, 3 May 1978 infrared image.	47
10 GOES infrared digital count to temperature calibration.	48
11 Tilt-sequence ten, southwest sector, zero-tilt reflectivity (dBZ)	51
12 Tilt-sequence ten, southwest sector, low-level PVSZ (dBZ)	52
13 Tilt-sequence ten, southwest sector, mid-level PVSZ (dBZ)	53
14 Tilt-sequence ten, southwest sector, upper-level PVSZ (dBZ)	54

LIST OF FIGURES (Continued)

FIGURE	Page
15 Tilt-sequence ten, southwest sector, VIL (kg m^{-2})	55
16 0215 GMT, 3 May 1978 infrared image, southwest sector	56
17 0230 GMT, 3 May 1978 infrared image, southwest sector	57
18 Tilt-sequence ten, northwest sector, zero-tilt reflectivity (dBZ)	58
19 Tilt-sequence ten, northwest sector, low-level PVSZ (dBZ)	59
20 Tilt-sequence ten, northwest sector, mid-level PVSZ (dBZ)	60
21 Tilt-sequence ten, northwest sector, upper-level PVSZ (dBZ)	61
22 Tilt-sequence ten, northwest sector, VIL (kg m^{-2})	62
23 0215 GMT, 3 May 1978 infrared image, northwest sector	63
24 0230 GMT, 3 May 1978 infrared image, northwest sector	64
25 MB enhancement curve (after Corbell, <u>et al.</u> , 1976). 74	

LIST OF ACRONYMS

AOIPS	Atmospheric and Oceanic Information Processing System
ATS	Applications Technology Satellite
CDA	Command and Data Acquisition station
CDDF	Central Data Distribution Facility
DMSP	Defense Meteorological Satellite Program
DVIP	digital video integrator and processor
ESSA	Environmental Science Services Administration
GMT	Greenwich Mean Time
GOES	Geostationary Operational Environmental Satellite
McIDAS	Man-computer Interactive Data Access System
NESS	National Environmental Satellite Service
NOAA	National Oceanic and Atmospheric Administration
NSSL	National Severe Storms Laboratory
PPI	plan position indicator
PVSZ	partial vertically-summed reflectivity
SAS 76	Statistical Analysis System 76
SEM	Space Environmental Monitor
SFSS	Satellite Field Service Station
SMS	Synchronous Meteorological Satellite
SSEC	Space Science and Engineering Center

LIST OF ACRONYMS (Continued)

TAMU	Texas A&M University
TIROS	Television and Infrared Observation Satellite
TTC	Telemetry, Tracking, and Command
VIL	vertically-integrated liquid water content
VISSR	visible and infrared spin scan radiometer

CHAPTER I

INTRODUCTION

The importance and use of weather radar as a means of detecting, observing, and forecasting severe weather phenomena is firmly established. Meteorological satellite data, particularly data from geostationary satellites, have also proved to be of great value in detecting, observing, and forecasting severe weather phenomena. The increasing availability of digital data from both meteorological radars and geostationary satellites makes ready comparison of both types of data feasible and useful in the analysis of severe weather phenomena. The possibility that characteristics of severe weather phenomena shared in common by the two types of data can be used in the real-time analysis and forecasting of severe weather has made comparisons of these data attractive to both operational and research meteorologists.

1. The Need for This Investigation

The increasing automation of systems for handling large volumes of meteorological data and the proliferation of interactive systems

The citations on the following pages follow the style of the Journal of Applied Meteorology.

designed to display and compare fields of satellite, digital radar, and conventional surface and upper-air data have focused increased interest on the development of procedures to acquire and analyze such data on a real-time basis for the forecasting of severe weather development. Interactive meteorological data handling systems are in use at some universities and within government agencies charged with research and development responsibilities. Interactive systems are expected to be in use at selected central forecasting facilities within the National Weather Service and the Air Weather Service in the near future. These systems must allow for rapid analysis of all data fields and ready comparison of significant features in each field of data with features in the other data fields. Maximizing the usefulness of such systems in forecasting applications also requires an understanding of the significant relationships between data fields such as digital satellite data and digital radar data. The large volume of high resolution digital data available at frequent intervals from the geostationary satellites such as the GOES (Geostationary Operational Environmental Satellite) spacecraft suggests that significant relationships may be established between the satellite data and simultaneous digital radar data which may be useful in the development of rainfall and flood forecasting techniques.

2. Present Status of Research Relating to This Investigation

Comparisons of meteorological satellite imagery with radar data have generally been either of a qualitative or a quantitative nature. Qualitative comparisons began shortly after the launch of TIROS 1 (Television and Infrared Observation Satellite 1), the world's first full-time meteorological satellite. Blackmer (1961) and Nagle (1963) used TIROS 1 imagery in comparison with available radar precipitation patterns to study squall line activity. Nagle and Serebreny (1962) compared TIROS 1 imagery with scope photographs from ground-based and airborne radars in studying the precipitation patterns associated with a maritime cyclone. Boucher (1967) compared imagery from several TIROS spacecraft with available radar data and mesoscale analyses in examining the relationship of satellite-observed cirrus shields to the severity of thunderstorm systems. Boucher found that the diameter of the cirrus shield resulting from the integration of all anvil clouds within a thunderstorm complex was an indicator of storm severity. Blackmer and Serebreny (1968) developed models of cloud and precipitation patterns associated with maritime cyclones based on TIROS 9 imagery, shipborne and shore-based radar data, and surface and upper-air data.

Vonder Haar (1969) employed data from the geostationary satellites ATS 1 (Applications Technology Satellite 1) and ATS 3 in a study

of reflected radiance applications which presented a detailed composite of a reflected radiance field and meteorological radar reports.

Vonder Haar and Cram (1970) also used ATS 3 imagery in a short-range forecasting study which included radar data as well as surface observations within a mesonetwok. SMS/GOES (Synchronous Meteorological Satellite/GOES) imagery, raingage data, and radar data provided the data base for Fujita's (1977) study of meteorological satellite applications for army operations.

Quantitative comparisons of meteorological radar and meteorological satellite data have been made using data from both polar-orbiting and geostationary satellites. Wexler and Allison (1972) employed Nimbus 4 infrared data and a reflectivity map from the National Severe Storms Laboratory (NSSL) WSR-57 radar to study a tornado outbreak that occurred near Oklahoma City. Gruber (1973) also used Nimbus 4 infrared data to determine areas of deep convection and compared his findings to radar data as part of a study concerned with estimating rainfall in convective areas.

ESSA 5 (Environmental Science Services Administration 5) and ESSA 7 satellite digital cloud mosaic films were examined by Gerrish (1970) to determine the cloudiness in each element of a grid array centered south of Miami, Florida. Gerrish used those data along with WSR-57 radar data, raingage data, and upper-air data in

examining the relationship between rainfall and cloudiness within the grid area. Gerrish (1975) later used DMSP (Defense Meteorological Satellite Program) satellite visible and infrared data and ATS 3 visible data in a similar study of cloudiness and precipitation. Gerrish determined that radar echo area correlated best with DMSP infrared cloud area at 18,000 ft and at 30,000 ft and that, on the average, radar echoes occupied only 42 per cent of the cloud area at those altitudes. DMSP data also were used by Phillips (1975) in a study that compared infrared satellite data with digital radar data from the NSSI. Phillips concluded that the DMSP imagery could be studied in greater detail when digitized using a microdensitometer but that detailed determination of the structure of convective storm activity did not seem possible with the infrared sensors then in use.

Blackmer (1975) studied the extent to which a combination of visible and infrared data indicated the presence and intensity of precipitation within a cloud and concluded that departures of brightness or radiance in small areas from the average value within the

cloud cover over a large area could be used to infer precipitation.

Cheng and Rodenhuis (1977) used NOAA 2 (National Oceanic and Atmospheric Administration 2) visible and infrared imagery along with WSR-57 radar data in comparing satellite images with radar rainfall rates. They found correlation coefficients between satellite data

and radar rainfall rates of from 0.23 to 0.34 for visible data and from 0.17 to 0.27 for infrared data.

Sikdar (1972) evaluated the relationship of rainfall patterns to cloud brightness fields and found that all of the radar echoes were included in the upper 36 to 40 per cent of the ATS 3 brightness range for the two cases considered. He indicated an excellent correlation between positive brightness anomaly area, radar echo area, and the precipitation pattern. Reynolds and Vonder Haar (1973) claimed that when growth of clouds could be detected by radar a corresponding increase in reflected radiance could be detected in ATS 3 visible imagery. Griffith and Woodley (1973) compared reflected radiances with radar-measured echo heights and found a positive correlation between cloud brightness and echo height. However, Negri et al. (1976) reported that brightness did not seem to correlate well with any echo parameters. Negri et al. also indicated that cloud area changes led echo area changes for the storm they examined. Adler and Fenn (1977) found that duration of cloud elements, minimum cloud-top temperature, and cold area rate of increase seemed to be correlated with the occurrence of severe weather.

Reynolds (1978) used an interactive computer system to evaluate digital radar and digital GOES data. Reynolds indicated that infrared

data show relative changes in top height which are related well to rainfall and that maximum rainfall occurs before the coldest cloud-top temperature is reached. Reynolds et al. (1978) also considered the use of meteorological satellites in weather modification projects and included comparisons of radar data and geostationary satellite data in seeking further to explore satellite-rainfall relationships. Smith and Reynolds (1978) have developed procedures to produce numerical composites of digital radar and digital satellite data for use in analyzing precipitation patterns.

Griffith et al. (1978) employed ATS 3 and SMS/GOES imagery in rainfall estimation applications using digital radar and rain gauge data for ground truth. They developed a rainfall estimation procedure based on the growth of radar echoes and satellite cloud areas and examined the procedure for potential real-time applications and automation.

3. Objectives of the Investigation

The primary objective of this investigation is to compare digital meteorological radar data with infrared imagery from a meteorological satellite in geostationary earth orbit by determining the correlation between point values of infrared digital count and point values of radar reflectivity and vertically integrated liquid water content (VIL). Comparisons are made between infrared digital count from the

satellite sensor and zero-tilt reflectivity, three levels of partial vertically-summed reflectivity (PVSZ), and VIL, for the purpose of determining which sets of data demonstrate the best relationship between the satellite and radar data.

A secondary objective of this investigation is to develop and implement procedures for computer processing of GOES imagery stored on magnetic tape and to map the data to points in the Texas A&M University (TAMU) digital weather radar grid.

4. Techniques and Scope of the Investigation

The radar data for this investigation were obtained from the digital weather radar system in the Department of Meteorology at TAMU. The reduction, interpolation and display of the radar data were accomplished on the Amdahl 470 V/6 computer at TAMU using the technique developed by Sieland (1977) as modified by McAnelly (1979). The digital GOES infrared data were obtained from the Man-computer Interactive Data Access System (McIDAS) at the Space Science and Engineering Center of the University of Wisconsin in Madison, Wisconsin. Reduction and display of the digital satellite data also were accomplished by the Amdahl 470 V/6 computer using a technique designed to map the satellite data to individual points in the radar grid established by the Sieland technique.

Tilt-sequence 10-cm digital radar data were collected near-simultaneously with GOES infrared imagery on 3 May 1978. The tilt-sequence data were processed to produce point values of zero-tilt reflectivity, three levels of partial vertically summed reflectivity (PVSZ), and vertically integrated liquid water content (VIL). The point values of the digital radar data were then tabulated along with GOES infrared digital count data mapped to corresponding points. The GOES infrared data were mapped from images at times corresponding to the start of the radar tilt-sequences and the end of the tilt-sequences. The tabulated data were punched onto computer cards and processed to compute correlations between each field of radar and satellite data.

Three sets of radar and satellite data were processed to reduce computer costs and meet time constraints imposed by tabulating the data and punching the data onto computer cards. One set of data was selected during the early development of radar echoes in the TAMU area and included one tilt-sequence of radar data and two infrared images for a corresponding area. The remaining two data sets were selected from a time when radar echo activity in the area appeared to be at or near its maximum intensity. The last two data sets were taken from a single tilt-sequence and from two corresponding infrared images.

CHAPTER II

METEOROLOGICAL RADAR DATA

Microwave radar is one of the many tools employed by meteorologists in studying the atmosphere. Digital radar systems have made possible quantitative comparisons of large volumes of radar data with data from other sources including the meteorological satellite data employed in this study. Much of the material in this chapter concerned with basic radar theory and the THMU weather radar system is extracted from Neyland (1978) that contains a more complete description of the digital radar system and the Sicland (1977) computer program.

1. Basic Radar Theory

The basic form of the radar equation used by radar meteorologists was derived by Probert-Jones (1962). Probert-Jones assumed a more realistic beam shape than had been used in previous derivations and further assumed that no significant attenuation existed between the radar antenna and the target and that the target completely filled the spatial volume illuminated by the radar beam. With these assumptions, the average backscattered power, \bar{P}_r (watts), received from the target at range r (km), is given by

$$\bar{P}_r = \frac{c |k|^2}{r^2} Z_e \quad (1)$$

where c ($\text{W km}^2 \text{ m}^3 \text{ mm}^{-6}$) is the radar constant unique to the individual radar, $|k|^2$ (dimensionless) is the dielectric constant from scattering theory, and Z_e ($\text{mm}^6 \text{ m}^{-3}$) is the equivalent radar reflectivity factor. An expression for the radar constant is given by

$$c = \frac{\pi^3 P_t G^2 h \theta \phi}{512 \lambda^2 2 \ln 2} \quad (2)$$

where P_t is the transmitted power during a radar pulse (W), G is the antenna gain (dimensionless), h is the pulse length in space of the transmitted pulse (cm), θ is the horizontal beamwidth (radians), ϕ is the vertical beamwidth (radians), and λ is the wavelength of the transmitted microwave energy (cm). The factor $2 \ln 2$ is the Probert-Jones correction factor. The value of c is 8.609×10^{-11} for the TAMU 10 cm radar and the value of $|k|^2$ is 0.93 (Battan, 1973).

The output of the radar system is digitized values of returned power, \bar{P}_r , which must be converted to values of reflectivity before further data reduction. The usual practice is to measure the returned power in terms of decibels with respect to a standard reference power level, normally 1 mw. Power levels are then expressed in units of dBm, either above (+) or below (-) 1 mw according to

$$P(\text{dBm}) = 10 \log_{10} \frac{P(\text{watts})}{10^{-3}(\text{watts})} \quad (3)$$

To determine values of Z_e , Eq. (1) is solved for Z_e giving

$$Z_e = \frac{r^2}{c |k|^2} \bar{P}_r . \quad (4)$$

Taking the logarithm of Eq. (4) gives

$$\log_{10} (Z_e) = 2 \log_{10} r + \log_{10} \bar{P}_r - \log_{10} c |k|^2 . \quad (5)$$

For the TAMU 10 cm radar, c is equal to 8.609×10^{-11} and $\log_{10} c |k|^2$ equals -10.1. Substituting these values into Eq. (5) gives

$$\log_{10} Z_e = 2 \log_{10} r + \log_{10} \bar{P}_r + 10.1 . \quad (6)$$

The digital value of \bar{P}_r is converted to its dBm equivalent (always negative) through the use of calibration data. The received power in watts is related to the received power in dBm by

$$\log_{10} \bar{P}_r \text{ (watts)} = 0.1 \bar{P}_r \text{ (dBm)} - 3.0 . \quad (7)$$

Substitution of Eq. (7) into Eq. (6) gives

$$\log_{10} Z_e = 0.1 \bar{P}_r + 2 \log_{10} r + 7.1 . \quad (8)$$

Finally, the value of Z_e is given by

$$Z_e = 10^{(0.1 \bar{P}_r + 2 \log_{10} r + w_c)} \quad (9)$$

where Z_e is in units of $\text{mm}^6 \text{ m}^{-3}$ and w_c is 7.1.

The several assumptions inherent in the development of Eq. (9) include:

- 1) The transmitted microwave energy is not significantly

attenuated between the radar antenna and the target. This assumption has been shown to be valid for radars with wavelengths near 10 cm (Greene, 1964).

2) The spatial volume illuminated by the radar beam is completely filled by the target. This condition is not always met, particularly on the periphery of a storm, with a resulting loss of resolution of fine scale detail in such areas (Greene, 1971). However, this effect does not significantly affect the major features in the digital data.

3) The Rayleigh approximation is used to describe the scattering properties of spherical liquid water drops having diameters on the order of 0.04λ , where λ is the radar wavelength in cm. In severe storms, the large, non-spherical water drops and hailstones which may be present do not meet the Rayleigh criteria. However, the enhanced reflectivity of these particles may be useful in identifying such storms.

4) Each digital datum value represents a point in the center of the radar volume.

5) The equivalent radar reflectivity values, Z_e , obtained from the digital data, are representative of a continuous scalar field.

2. Earth Curvature Correction

Microwave radiation propagating in free space will follow a

straightline path. However, the microwave radiation of a radar beam in the atmosphere does not follow a straightline path but instead follows a curved path due to refraction. The amount of curvature of the path depends on the index of refraction (n). Under normal atmospheric conditions where temperature and humidity decrease with height the path of the radar beam curves slightly downward toward the surface of the earth.

Ray theory may be applied to the problem if the change with height of the index of refraction, $\frac{dn}{dh}$, is small. For that case, the exact differential equation for a ray in a spherically stratified atmosphere is

$$\frac{d^2h}{ds^2} = \left(\frac{2}{R+h} + \frac{1}{n} \frac{dn}{dh} \right) \left(\frac{dh}{ds} \right)^2 + \left(\frac{R+h}{R} \right)^2 \left(\frac{1}{R+h} + \frac{1}{n} \frac{dn}{dh} \right) \quad (10)$$

where h is the height of the beam above the earth's surface at a distance s from the transmitter, R is the earth's radius, and n is the index of refraction. Since ϵ , the angle at which the beam is sent out measured from a horizontal plane, is usually very small,

$\left(\frac{dh}{ds} \right)^2 = \tan^2 \epsilon \ll 1$. Also, since $n \approx 1$ and $h \ll R$, Eq. (10) can be reduced to

$$\frac{d^2h}{ds^2} = \frac{1}{R} + \frac{dn}{dh} \quad . \quad (11)$$

In this investigation it is necessary to consider the radar beam axis

as a straight line so that a fictitious earth radius given by

$$R' = \frac{R}{1 + \frac{dn}{dh}} \quad (12)$$

must be assumed (Buttan, 1973). Since $\frac{dn}{dh}$ is small and nearly linear with a value of $-4 \times 10^{-8} \text{ m}^{-1}$, an earth curvature correction of

$R' = \frac{4}{3} R$ is used and the resultant radar beam axis may be considered to be a straight line.

3. The TAMU Weather Radar System

The TAMU Weather Radar System consists of both a 3-cm and a 10-cm radar operating in parallel. Each of the two radar systems has a nearly identical makeup and consists of the following major sub-systems: antenna, conventional analog weather radar set, digital video integrator and processor (DVIP) with plan position indicator (PPI) display, and a nine-track tape unit to record the buffered digital output of the DVIP. Since only 10-cm radar data are used in this study, the following discussion is limited to some of the characteristics of the 10-cm radar.

The 10-cm radar was constructed at TAMU using components from several different radars. The radar receiver is mounted in a CPS-9 console and uses the same synchronizing pulse generator used to trigger the 3-cm radar. This, combined with the common mounting of the 3- and 10-cm antennas, permits simultaneous scanning of the

same illuminated volume by both radars.

The DVIP is a high speed data acquisition, digitizing, and processing system which continuously averages radar logarithmic video output in range (range averaging) and in direction of antenna scan (time averaging) using exponentially weighted digital integrator techniques and synchronized by the radar system trigger. The DVIP installation provides for real-time contoured PPI displays and digital recording of the digital, integrated data.

The DVIP output signal is split into two channels, the digital channel and the display channel. The display channel provides either log video or contoured log video to the PPI scope. The digital output consists of the 1- or 2-km range increment integrated video samples, provided in a buffered 8-bit parallel binary configuration. Each digital output word represents a digital value of the integrated video intensity on a linear scale over the input dynamic range of 80 dB. At the digital output there are 215 2-km or 430 1-km digital samples representing the range increments from 21 through 450 km of range, depending on the range increment selected.

The digital output channel of the DVIP is fed into a 9-track magnetic tape recording unit. This tape drive unit records the digital data in a format that makes it readily accessible by computer and controls the azimuth increment integration of the data.

4. Data Reduction and Display

The digital output of the DVIP is recorded on 9-track magnetic tape which becomes the input to the TAMU Amdahl 470 V/6 computer. Computer processing of the digital radar data is performed using a program developed by Sicland (1977) and modified by McInnelly (1979).

The computer program begins by transforming the spherical coordinate system (r, α, ϵ) of the recorded digital radar data into a cylindrical coordinate system (r, α, h) with three separate height divisions, or partial vertically summed reflectivity (PVSZ) layers. The data are then transformed into a two-dimensional rectangular coordinate system (x, y) and five maps are produced, a zero level (zero-tilt) reflectivity map, the three PVSZ maps, and a map of vertically-integrated liquid water content (VIL). The conversion of coordinate systems requires the use of two interpolation schemes, a Lagrangian linear or cubic interpolation scheme along each radial of data and a quadratic scheme for the conversion to rectangular coordinates. An extensive explanation of these interpolation schemes is contained in Sicland (1977).

The three PVSZ maps are produced by summing the reflectivity values in a vertical column above a given (x, y) point at the surface into the lower layer (0-deg to 15 kft), the middle layer (15 to 35

kft), and the upper layer (35 to 50 kft). The summed values of reflectivity in each layer at each (x, y) point are divided by the number of tilt angles used to produce the sum so that a mean value of the reflectivity is produced. VIL is produced using an algorithm developed by Greene (1971) and is based on the relationship

$$M^* = 3.44 \times 10^{-6} \int_{h_{\text{bottom}}}^{h_{\text{top}}} z_e^{-4/7} dh \quad (13)$$

where M^* is the VIL in units of kg m^{-2} and h is the height in meters.

Because of the large amount of data processed and to reduce computation time, the Sieland program maps only a selected portion of a grid centered on TAMU. The mapped portion is selected by specifying a distance east (-) or west (+) from TAMU to the lower left corner of the 100×100 km grid, a distance north (-) or south (+) from TAMU to the lower left corner of the 100×100 km grid, a starting azimuth for data processing, and a last azimuth. Computer processing of the data on the 100×100 km grid results in a data output spatial resolution of 2-km on a 51×51 output array.

The radar data used in this investigation were produced and recorded by the TAMU Weather Radar System during the evening of 2 May 1978 (3 May 1978 GMT), as an area of light and moderate thunderstorm activity moved through the College Station area. Tilt-sequence data were recorded at times which would permit comparison

with GOES satellite data collected that evening at 15-min intervals.

This investigation used two tilt-sequences of the radar data for comparison with GOES imagery, the first tilt-sequence beginning at 0022 GMT and the tenth tilt-sequence beginning at 0215 GMT. These tilt-sequences were processed by Mr. Ray McAnelly to produce maps of zero-tilt reflectivity, PVSZ in three layers, and VIL.

The maps of zero-tilt reflectivity, PVSZ, and VIL were adjusted for ground clutter effects by excluding all data within a 40 km radius of TAMU in order to avoid data contamination and to assure comparability between results for the zero-tilt reflectivity maps and the PVSZ and VIL maps. Data at the outer edges of the radar maps and along bounding azimuths used by the Sieland program also were excluded due to suspected boundary interpolation problems in the computer program. After these adjustments, the data were tabulated for comparison with the infrared satellite data.

CHAPTER III

GEOSTATIONARY METEOROLOGICAL SATELLITE DATA

Meteorological satellites have been used by meteorologists for both qualitative and quantitative investigations of atmospheric phenomena. Geostationary satellites, by virtue of near-continuous coverage of large areas of the earth surface, permit more detailed examination of severe weather development than is possible through the use of polar-orbiting satellites. The on-board digitization of the data from the newer geostationary satellites makes possible ready comparison of these data with other digital data fields and is useful in the analysis of severe weather occurrences.

1. The SMS/COES Spacecraft

The Synchronous Meteorological Satellite/Geostationary Operational Environmental Satellite (SMS/GOES) spacecraft is a cylindrical spacecraft weighing approximately 578 kg at launch. The spacecraft are placed into a circular orbit at about 35,800 km above the earth surface. The satellites orbit the earth at a speed c about $11,000 \text{ km hr}^{-1}$. This combination of altitude and speed permits each satellite to remain continuously above the same point on the earth and produces what is referred to as a geostationary or

geosynchronous orbit.

The spacecraft is controlled for proper earth-imaging by an attitude control subsystem which maintains the spin rate at 100 rpm and aligns the spacecraft spin axis parallel to the earth's polar axis. On-board altitude sensors are used to determine the spin axis orientation and a hydrazine jet system is used to adjust the spin axis orientation, spin rate, and orbital position as necessary (Corbell *et al.*, 1976).

The primary purpose of the spacecraft is to provide earth-imaging in the visible spectrum (0.55 to 0.7 μ m) with an 0.9-km resolution at subpoint and in the infrared spectrum (10.5 to 12.6 μ m) with an 8-km resolution at subpoint. The spacecraft also possesses a capability to provide direct, quantitative measurements of solar activity and to collect and distribute environmental data measured on remotely located data collection platforms on the earth's surface and in its atmosphere.

Primary sub-systems aboard the spacecraft include the Visible and Infrared Spin Scan Radiometer (VISSR), the Space Environmental Monitor (SEM), the Telemetry, Tracking, and Command (TTC) sub-system, and an attitude-control sub-system. The VISSR provides earth-imaging in the visible and infrared spectrums. The SEM includes a magnetometer, a solar x-ray telescope, and an energetic

particle monitor. The TIC includes equipment for S-band transmission and reception (in reduced bandwidth) of VISSR data, S-band transmission of weather facsimile data, UHF reception of data from remote data collection platforms and downlink of these data to earth, and VHF and S-band communications equipment for commanding the spacecraft, for telemetry, and for transmitting SEM data. The primary instrument providing the data used by most meteorologists is the VISSR (Corbell *et al.*, 1976).

2. The Visible and Infrared Spin Scan Radiometer

The Visible and Infrared Spin Scan Radiometer scans from west to east in eight identical visible channels and two infrared channels. The sensor provides visible data at 0.9-km resolution at satellite subpoint and infrared data of 8-km resolution at satellite subpoint. The resolution in both the visible and infrared data deteriorates for points away from the satellite subpoint. With the satellite rotating at 100 rpm, the VISSR scans the earth for about one-twentieth of each complete rotation. The radiometer performs 1821 steps in successive scans from north to south in 18.2 min and provides an image of the complete earth disc or about one quarter of the earth's surface. The resulting visible images contain 14,568 lines. The infrared images have a total of 1821 lines. In addition to the normal scanning

mode, the spacecraft may be placed into a limited scan mode. In the limited scan mode the north-south scan may be limited to a fewer number of scan lines, thereby reducing the area of coverage but increasing the frequency of imaging.

The VISSR senses radiation in both the visible and infrared spectrums. Radiation is received by the VISSR's primary optics via a 45° object-space scan mirror. The mirror is an elliptically shaped plane mirror which is tilted about its minor axis to obtain the north-south scan steps. West-east scans are produced by spacecraft rotation about the spin axis. Energy from the scan mirror is collected by a Ritchey-Chretien optical system which includes a baffle that extends from the mirror to minimize the effects of scattered radiation. Radiation in the visible spectrum is detected at the prime focus using eight fiber optics in a linear array at the focal plane. The other ends of the fibers are optically integrated with eight photomultiplier tubes having the desired 0.55-to 0.70- μm response. The prime focal plane is also relayed to the long-wavelength HgCd/Te detector using two germanium relay lenses. An optical filter between the final relay lens and the detector restricts the radiation to the 10.5-to 12.6- μm wavelength band (McKowan, 1977).

3. Data Distribution and Processing

The SMS/GOES VISSR data are distributed as indicated in Fig.

1. Raw data are read out and preprocessed at the Command and Data Acquisition (CDA) station at Wallops Island, Virginia. The CDA processes the data to reduce the data rate by about 16 to 1 for simplification of data transmission and then transmits these stretched data back to the satellite. Lower resolution infrared data are formatted for analog transmission and are sent via telephone lines from the CDA to the Satellite Field Service Stations (SFSS) and to the Central Data Distribution Facility (CDDF) at Marlow Heights, Maryland.

The stretched data are retransmitted by the satellite to the National Environmental Satellite Service (NESS) facility at Suitland, Maryland, and to other facilities with a direct readout capability. The NESS-Suitland complex relays the stretched data via microwave link to the CDDF. The CDDF formats the data and prepares it for transmission to SFSS's throughout the country. Enhancement of the infrared data to emphasize specific features in the imagery can be accomplished both by the CDA at Wallops Island and by the CDDF.

GOES/SMS VISSR data are available to many users through a "GOES-Tap" program using high-quality telephone line transmission of the data from an SFSS to the user. As an alternative, some facilities have developed a direct readout capability for receiving the stretched VISSR data (Corbell *et al.*, 1976).

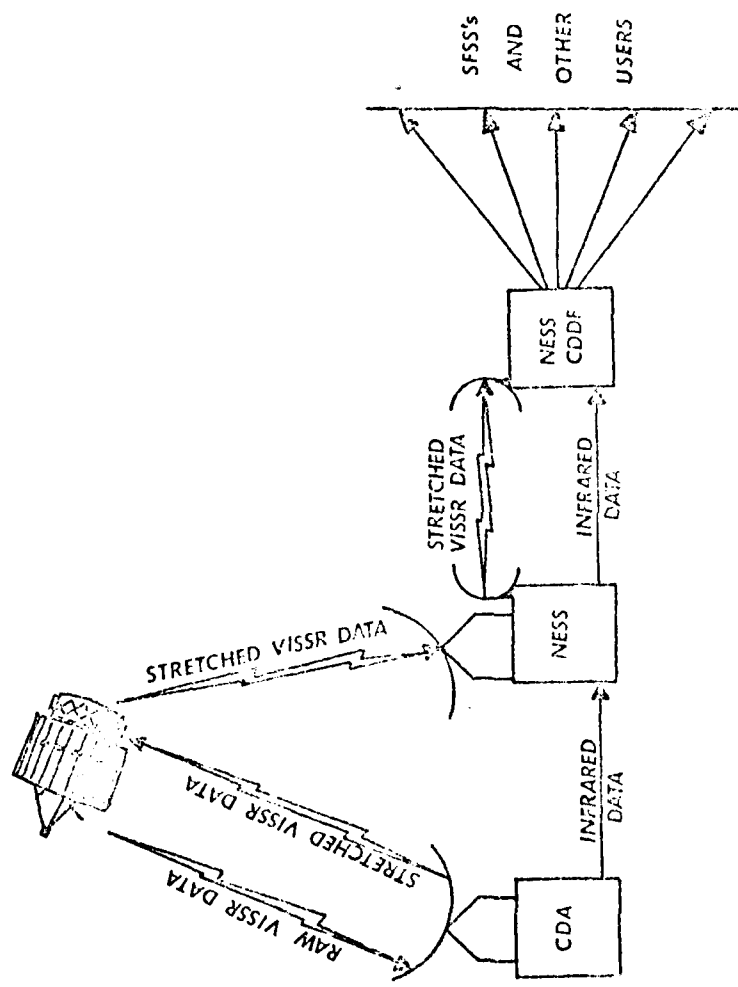


Fig. 1. SMS/GOES Data Distribution.

4. Basic Characteristics of Infrared Satellite Data

Infrared radiation is emitted by objects at an intensity that depends on the temperature of the body. If the object is assumed to emit radiation as a "black body," i.e., to absorb all radiation falling upon it without reflecting any of the incident radiation, then the monochromatic intensity of the emitted black body radiation is given by Planck's Law,

$$E = 3.74 \times 10^{-5} \lambda^{-5} \left(\exp \frac{1.4385}{T} - 1 \right)^{-1} \quad (1)$$

where λ (cm) is the wavelength of the emitted radiation and T (K) is the temperature of the black body (Haltiner and Martin, 1957). The proportionality between the temperature of the target and the intensity of the infrared radiation emitted by the target forms the basis for all infrared imaging.

Infrared sensors aboard meteorological satellites measure long-wave (usually 10.5- to 12.6- μ m wavelength) radiation emitted by cloud, land, and water surfaces. These measurements may be converted to black body temperatures which generally represent the temperatures of the surfaces viewed. This characteristic of infrared satellite imagery is especially useful in that it permits an approximate evaluation of the height of various clouds when the atmospheric temperature is known from upper-air data. The association of cold

cloud tops apparent in infrared data, convective activity, and precipitation suggested by some of the authors cited in Chapter I forms the basis for much of the following material in this investigation.

5. McIDAS Data

The Man-computer Interactive Data Access System (McIDAS) was developed by the Space Science and Engineering Center (SSEC) at the University of Wisconsin as a means of obtaining easy access to satellite data in the time domain for examining atmospheric weather systems as dynamic systems (Smith, 1975). The operator using McIDAS views image and graphics data on a large color television monitor. Images may be viewed in single frames or sequences and may be enhanced, colorized, or combined at the choice of the operator. Control of the system is effected from the operator's console by means of twin joysticks and a keyboard. The operator also may be supported by hard copy generating devices such as line printers and graphics plotters (Haig, 1978).

Image data used by the McIDAS also may be saved on magnetic tape for later use or for the use of other investigators. The imagery used in this study was produced in such a fashion by the McIDAS at the SSEC in Madison, Wisconsin.

McIDAS image save tapes contain two-dimensional image sectors prepared from a variety of image sources. The data for this study

are a sequence of infrared images from the GOES-East satellite taken between 0015 GMT and 0345 GMT on 3 May 1978. The data are stored on the tapes in a directory record which contains date, time, and line and element coordinate information necessary for image processing and in image sector records which follow the directory record. Each image sector record contains six lines of GOES data in 24-bit words so that for a complete image of 500 lines a total of 84 image sector records is required. The directory record is 225 words long and each image save record is 2241 words long (6723 8-bit bytes). 6720 bytes of each image save record are used for data with the remaining 3 bytes containing a record sequence counter (Young, 1978).

Full-resolution GOES-East infrared imagery are used in this study. Each pixel, or picture element, has a resolution of approximately 8 km in the line direction (N-S at satellite subpoint) and 4 km in the element direction (E-W at satellite subpoint). The McIDAS artificially subdivides each pixel to a 4 km by 4 km pixel on the image save tapes. Line and element numbering in the infrared data is based on the system used for full-resolution visible data (Young, 1978).

6. Data Reduction and Display

Use of the McIDAS image save tapes required development of procedures to navigate, or locate, the image pixels, to map the infrared data into the grid used for the digital radar data, and to correct the data for displacement error due to cloud height.

a. Image Navigation

Navigating the image pixels requires extensive computer software that was not available for this investigation. Instead, Mr. J. T. Young of the SSEC provided line and element navigation solutions for four latitude and longitude points in a grid around TAMU for each hour from 0000 GMT to 0400 GMT on 3 May 1978. A fourth-order polynomial was then fitted to the line and element solutions for each point to permit interpolating line and element solutions for intermediate times. The interpolated line and element solutions then were used as inputs to a computer program called MACKMAP 3 which produced mapping equations to map the satellite data into the radar grid.

b. Mapping the Satellite Data to the Radar Grid

The satellite data array is a two-dimensional array arranged by line and element number. The radar grid centered on TAMU can be regarded as an (x, y) array with a positive y-axis oriented due North and a positive x-axis oriented due East. The variation in

line and element solutions for the four points navigated by the SSEC suggested that simple bi-linear relationships of the form

$$\text{line number} = ax + by + c \quad (2)$$

$$\text{element number} = dx + ey + f \quad (3)$$

could be used to relate the digital satellite line and element numbers to the coordinates of the radar grid, where the constants a , b , c , d , e , and f are determined by solving three simultaneous equations using solutions for three of the four points navigated by the SSEC. The original mapping program, MACMAP 1, used navigation solutions for three points to produce coefficients for the mapping equations and used the remaining solution for the fourth point to check the accuracy of the equation. MACMAP 1 solutions produced results accurate to one half pixel for the fourth point for all images except two and was within one pixel for those two images.

An effort to produce more accurate mapping of the satellite data resulted in adding new terms to the mapping equations using the fourth point to determine "correction factors" k_1 and k_2 . The new equations were of the form

$$\text{line number} = ax + by + c + k_1(x-x_0)(y-y_0) \quad (4)$$

$$\text{element number} = dx + ey + f + k_2(x-x_0)(y-y_0) \quad (5)$$

where the coefficients a , b , c , d , e , and f are determined by solving simultaneous equations for the three original points and the correction

factors by determining the difference between the SSEC navigation solutions and the solutions from Eq. (2) and Eq. (3). The values of the constants x_0 and y_0 are determined from the "common values" of x and y shared by the three points used to solve the simple bilinear equations. Fig. 2 illustrates the general arrangement of the four navigated points relative to TAMU and the radar grid and illustrates how x_0 and y_0 were determined.

The MBCMAP 3 computer program produced coefficients for Eq. (4) and Eq. (5) for each of the images used in this study. The solutions produced accurate results for all four points originally navigated by the SSEC and accurate line number solutions for TAMU coordinates in a later check. A check of the element coordinate for TAMU was not accurate in the later check due to loss of the original input "gamma shifts" used to produce the SSEC solutions.

The procedure adopted in the remainder of this study depended upon the following assumptions:

- 1) The navigation solutions produced for the four points by the SSEC are accurate. Young (1978) suggests an accuracy to within one line number and within two element numbers in the full-resolution visible data. The numbering system for lines and elements in the infrared data is based on that for the visible data and is incremented by a factor of four which suggests an accuracy to the nearest pixel

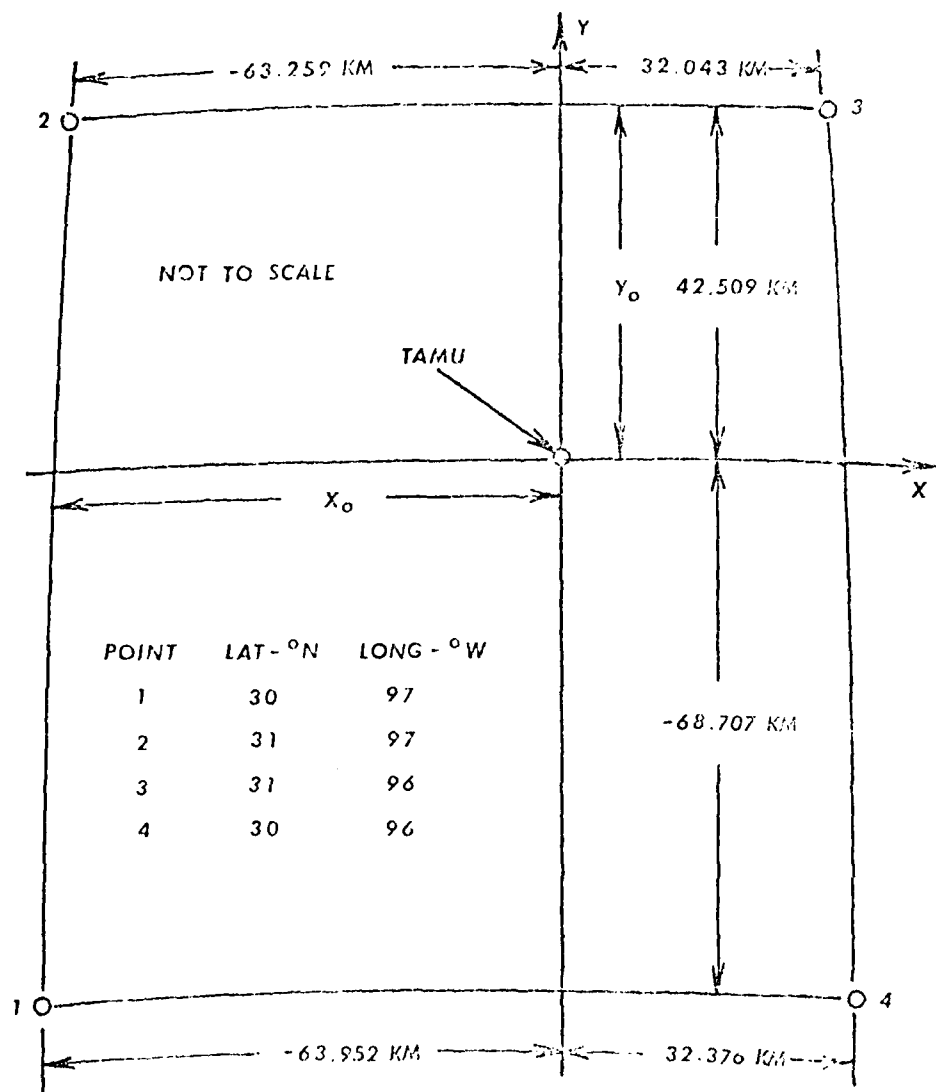


Fig. 2. Navigated points and mapping to the digital radar grid.

in the infrared data.

2) Interpolation in time using a fourth-order polynomial produces accurate solutions for intermediate image times. This assumption is required as a compromise to avoid the computer costs associated with providing SSEC solutions for images at 15-min intervals over 4 h and for four points in each image. The variation with time of the original SSEC solutions suggests that this assumption is valid.

3) Mapping equations of the form of Eq. (4) and Eq. (5) provide an accurate coordinate transformation between the line and element coordinates of the satellite image array and the (x, y) coordinates of the digital radar grid. MACMAP 3 mapping solutions provided accurate results for the SSEC solutions for all four navigated points and for TAMU coordinates. Comparisons of contoured fields of infrared data mapped using MACMAP 3 solutions to hard copy enhanced GOES infrared imagery also confirm the general accuracy of the mapping procedure. It is evident, however, that the earth curvature considerations used in establishing the radar grid for MACMAP 3 would not compensate for such effects at distances far removed from the center of the grid. For studies of data within 200 km of TAMU the MACMAP 3 procedure appears to yield satisfactory results.

Actual production of maps of satellite data depended upon development of programs designed to use MACMAP 3 solutions for the coefficients of Eq. (4) and Eq. (5). The original program was called MACVIS and was designed to map full-resolution visible GOES data to the radar grid. Problems with brightness normalization due to a very large solar zenith angle led to abandoning the use of the visible data after MACVIS was developed. The MACIR computer program was developed from the MACVIS program and is designed to use solutions to Eq. (4) and Eq. (5) to map GOES infrared satellite data into the radar grid centered on TAMU.

MACIR is a modular computer program using two function subprograms to produce solutions to Eq. (4) and Eq. (5) and using subroutines to save an array of satellite data that just overlaps the area of the radar grid that is of interest and to map the saved data array into the radar grid. Subroutine BOUND determines bounding line and element numbers so that the saved satellite data can be extracted from the image sector records on the McIDAS image save tapes. Subroutine DATSAV reads the image sector records and saves the GOES data between the bounding line and element numbers determined by BOUND. Subroutine DATMAP computes a line and element number for each (x, y) point in the portion of the radar grid selected for analysis and assigns the value of the pixel corresponding

to that (line, element) pair to the (x, y) point in the radar grid.

The data thus mapped are stored in an array called IGOES. Subroutine OUTPUT is used to print maps of the IGOES array and is readily adapted to varying grid spacing.

The MACIR program was used to produce maps of the 0015 GMT, 0030 GMT, 0215 GMT, and 0230 GMT GOES-East images for 3 May 1978 for this investigation. Maps of all the images between 0015 GMT and 0345 GMT also were produced for a different study. The maps consisted of point values of GOES-East infrared data printed at 2-km intervals for this investigation and 4-km intervals in the other maps. A listing of the MACMAP 3 and MACIR programs is contained in Appendix A.

c. Correction for Displacement Error Due to Cloud Height

Cloud interpretation near the horizon of a geostationary satellite image is complicated by the effect of curvature of the earth surface. Near the satellite subpoint on the earth's surface, the apparent and actual cloud positions coincide. However, the difference between the apparent and actual positions increases as the cloud's distance from the subpoint increases. In order to locate accurately a cloud feature in a geostationary satellite image it is necessary to compensate for this effect by making a displacement correction toward the satellite subpoint. Weiss (1978) gives a method of correcting

SMS images for this effect and that method was used to compute displacement errors for various cloud heights using a GOES-East subpoint of 0.335° S, 75.021° W. Displacement corrections were computed for TAMU for various cloud heights and are listed in Table 1.

Table 1. Displacement corrections for cloud height.

Cloud Height (km)	Displacement Correction (km)
10	9.17
12	11.00
14	12.83
16	14.66

Cloud height was determined by converting an average digital count for each image to an equivalent black body temperature and selecting the ICAO standard height corresponding to that temperature in the 2350 GMT College Station sounding. For temperatures near and above the tropopause a different procedure was used. The saturation adiabat from the convective condensation level was used to determine an equilibrium level on the sounding. Above this level a subjective estimation of the temperature of convective tops based on approximately 20 per cent mixing with environmental air was

used to determine a temperature-height relationship.

Rather than attempt to shift each point in each satellite image toward the satellite subpoint an amount dependent upon the individual digital count at each point, a uniform shift of the data toward the satellite subpoint based on the average digital count for the image was used. This procedure was adopted to avoid computational problems and to prevent creation of "shadows" in highly contoured infrared data fields. Table 2 lists the magnitudes of the corrections applied to the images in this investigation.

Table 2. Displacement correction for each image.

Image Time	Average Digital Count	x Displacement (km)	y Displacement (km)
0015Z	190	5	8
0030Z	204	6	9
0215Z	211	6	9
0230Z	218	7	11

After the GOES infrared images were mapped to the radar grid and corrected for displacement error due to cloud height, the data for these images were tabulated along with corresponding radar data in the three radar data sets. These data then formed the three data sets examined in this investigation.

CHAPTER IV

COMPARISON OF DIGITAL RADAR AND SATELLITE DATA

Comparison of the fields of digital radar and digital satellite data was performed by first qualitatively comparing contoured maps of the data and then objectively comparing the fields by computing correlation coefficients between the radar and satellite data using the SAS 76 statistical analysis system (Barr *et al.*, 1976) as implemented on the Amdahl 470 V/6 computer at TAMU.

1. The Basis for the Comparison

Meteorological radars examine the structure of weather systems by emitting electromagnetic energy in the microwave portion of the electromagnetic spectrum and measuring the amount of that energy scattered back to the radar by hydrometeors of various sizes and shapes associated with the weather system. Meteorological satellites examine weather systems by sensing the intensity of scattered or emitted electromagnetic energy from the cloud structures and, ultimately, from the hydrometeors that make up the clouds themselves. Sensors aboard meteorological satellites typically respond to electromagnetic radiation in the visible and infrared portions of the electromagnetic spectrum although ultraviolet and

microwave sensors have been used for special applications.

Since both meteorological radars and meteorological satellites examine weather systems by the use of scattered or emitted electromagnetic radiation at different wavelengths, it is reasonable to expect that some relationship should exist between meteorological radar data and meteorological satellite data that are coincident in time and space. The basic purpose of this investigation is to determine if such a relationship exists and, if so, to measure the strength of such a relationship.

To examine the relationship between meteorological radar data and meteorological satellite data, two tilt-sequences of digital radar data and four infrared GOES-East satellite images were examined. The first tilt-sequence was selected early in the data collection period when radar-detected weather activity in the area was relatively weak and just beginning to develop. GOES-East images collected just prior to initiating the tilt-sequence and at its conclusion were used for the comparison. The second tilt-sequence was selected from a later time interval in which line convective activity in the TAMU area had reached near-maximum intensity for the data collection period. Comparison GOES-East infrared images also were selected for times closely corresponding to initiation and termination of the tilt-sequence. The results of the comparisons of

these tilt-sequences with the corresponding satellite data are presented in the following sections.

2. First-Tilt-sequence and Corresponding GOES Images

The first digital radar tilt-sequence was collected from 0022 GMT to 0030 GMT on 3 May 1978. The data were collected in 14 1° inclinations of the radar antenna with each change in antenna angle being made at the conclusion of a 360° sweep. Data from the northwest sector of the tilt-sequence were processed by the Sieland (1977) computer program. The 0015 GMT and 0030 GMT GOES-East infrared images were used for comparison with this tilt-sequence. Maps of zero-tilt reflectivity (dBZ), low-, mid-, and upper-level PVSZ (dBZ), and VIL (kg m^{-2}) are presented in Figs. 3, 4, 5, 6, and 7, respectively. Contoured maps of infrared digital count for the 0015 GMT and 0030 GMT GOES-East images for corresponding areas are presented in Figs. 8 and 9, respectively. Conversion from infrared digital count to equivalent black-body temperature can be approximated by using Fig. 10.

Significant features to note in the digital radar data include a marked absence of indications of echo activity in the upper-level PVSZ map (Fig. 6) and the VIL map (Fig. 7). Echo activity of weak to moderate intensity is indicated in the zero-tilt reflectivity

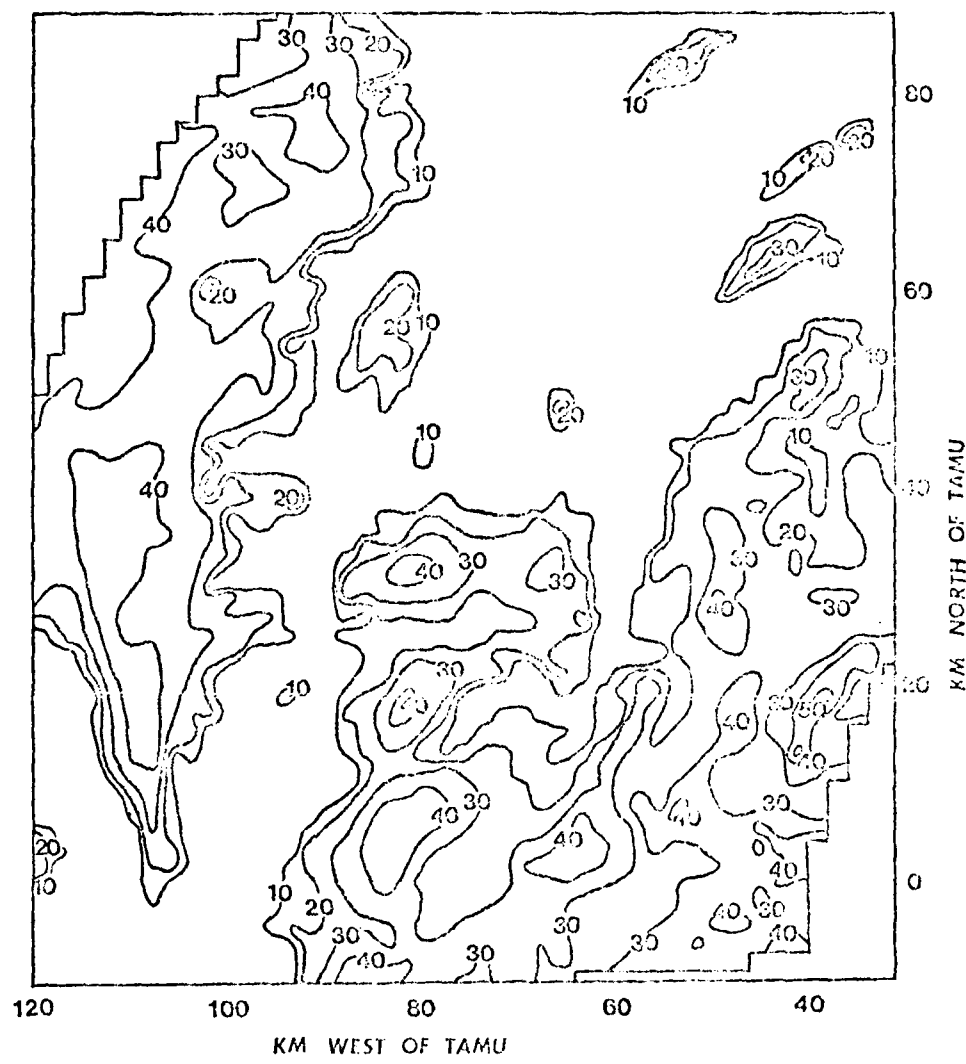


Fig. 3. Tilt-sequence one, zero-tilt reflectivity (dBZ). Data collected on 3 May 1978 at 0022 GMT.

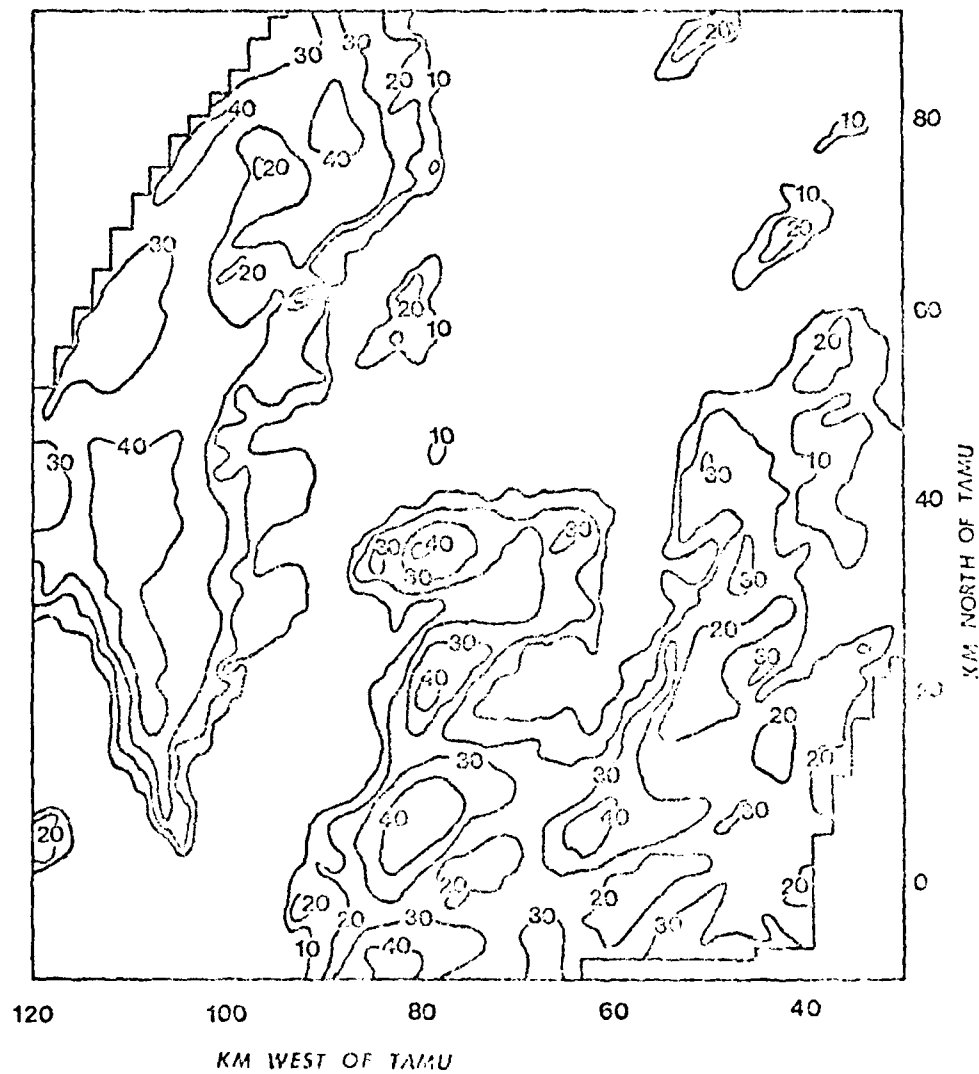


Fig. 4. Tilt-sequence one, low-level PWSZ (dBZ). Data collected on 3 May 1978 from 0022 GMT to 0036 GMT.

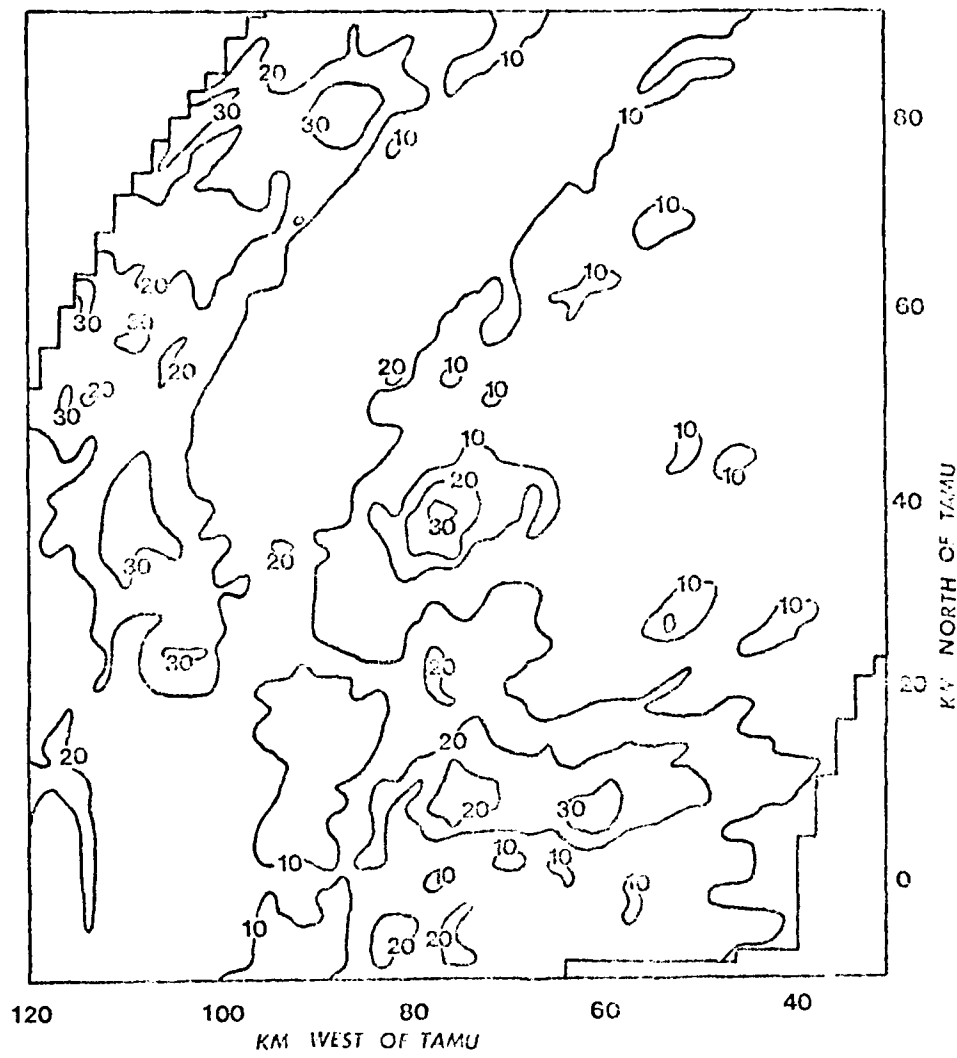


Fig. 5. Tilt-sequence one, mid-level PVSZ (dBZ). Data collected on 3 May 1978 from 0022 GMT to 0030 GMT.

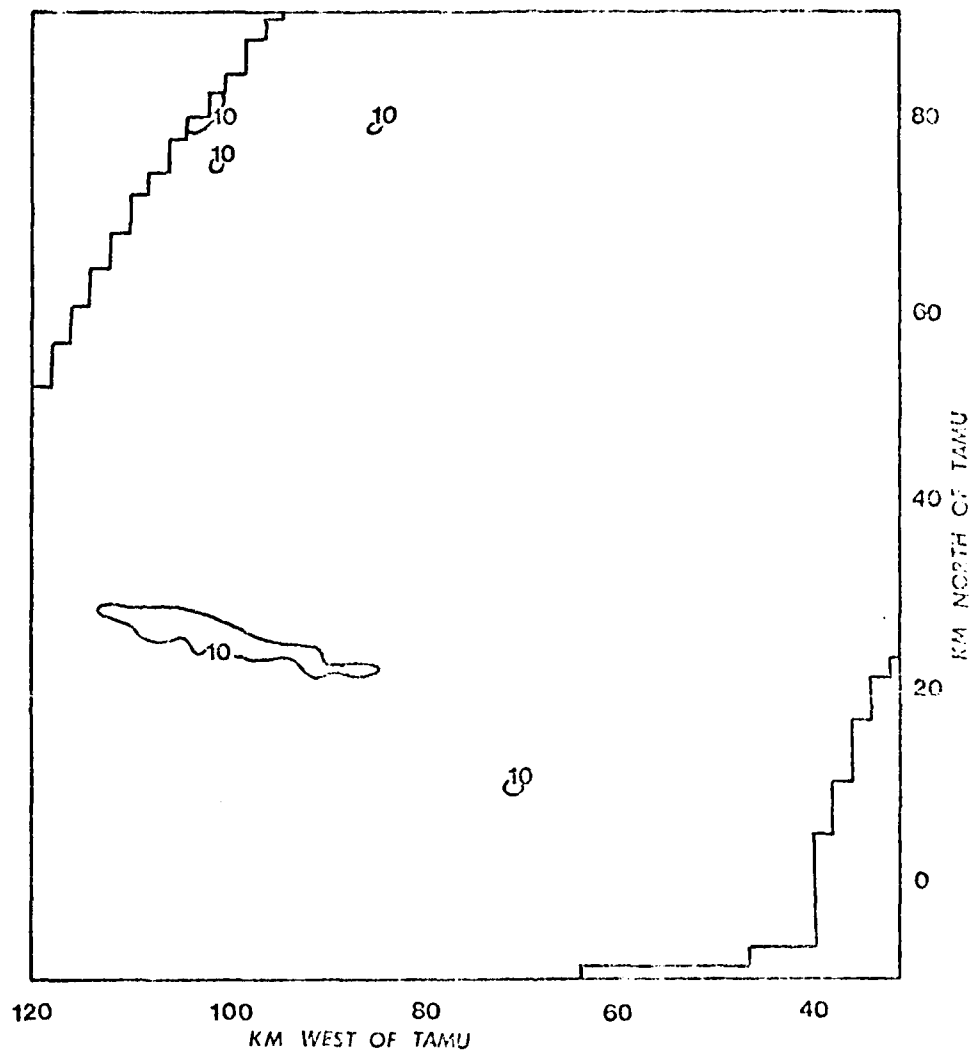


Fig. 6. Tilt-sequence one, upper-level PVSZ (dBZ). Data collected on 3 May 1978 from 0022 GMT to 0030 GMT.

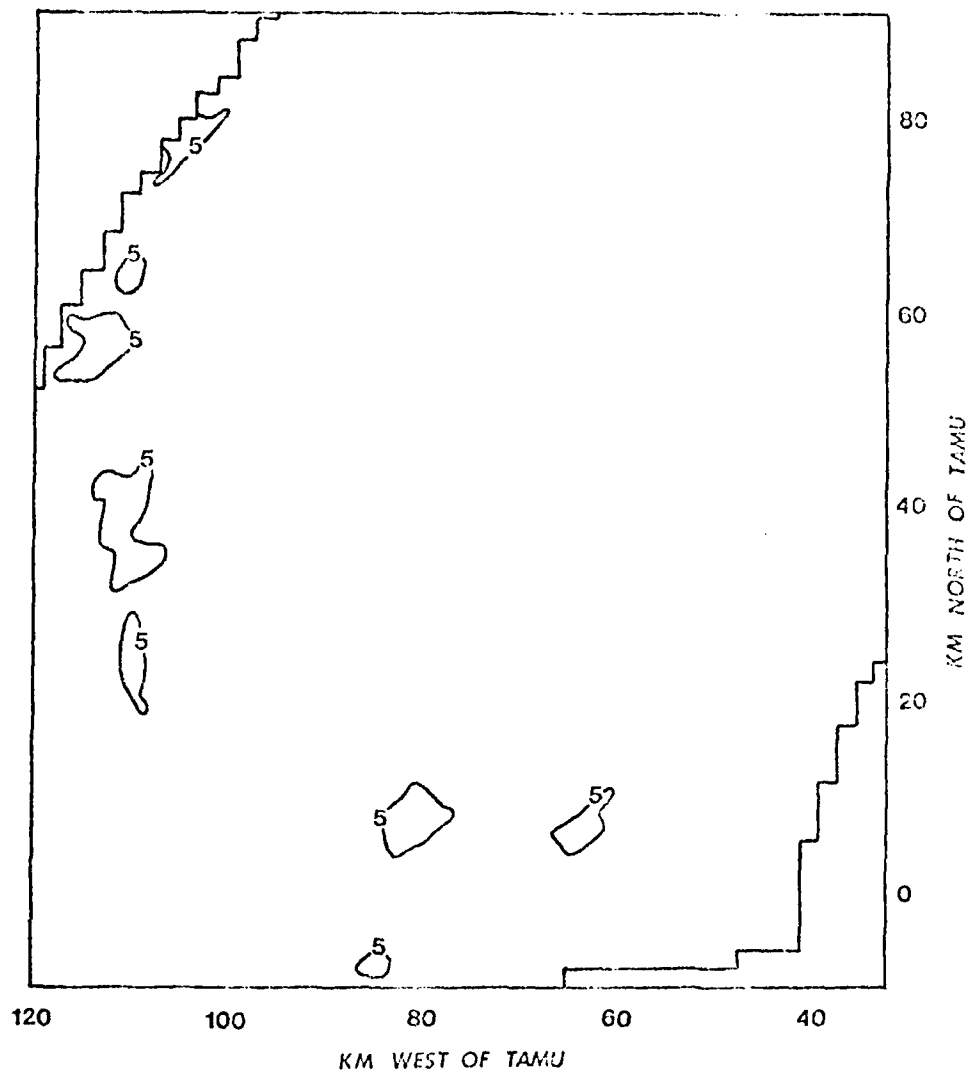


Fig. 7. Tilt-sequence one, VIL (kg m⁻²). Data collected on 3 May 1978 from 0022 GMT to 0030 GMT.

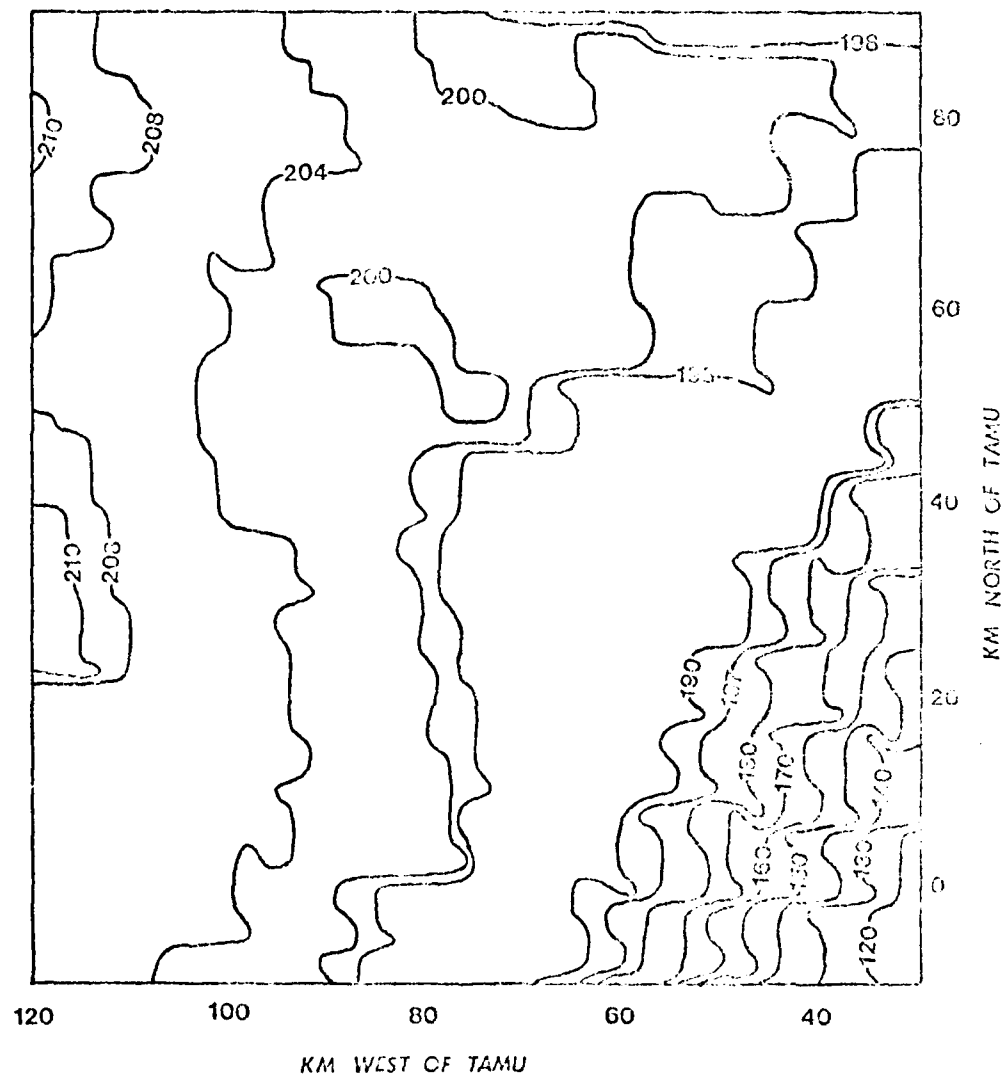


Fig. 8. 0015 GMT, 3 May 1978 infrared image.

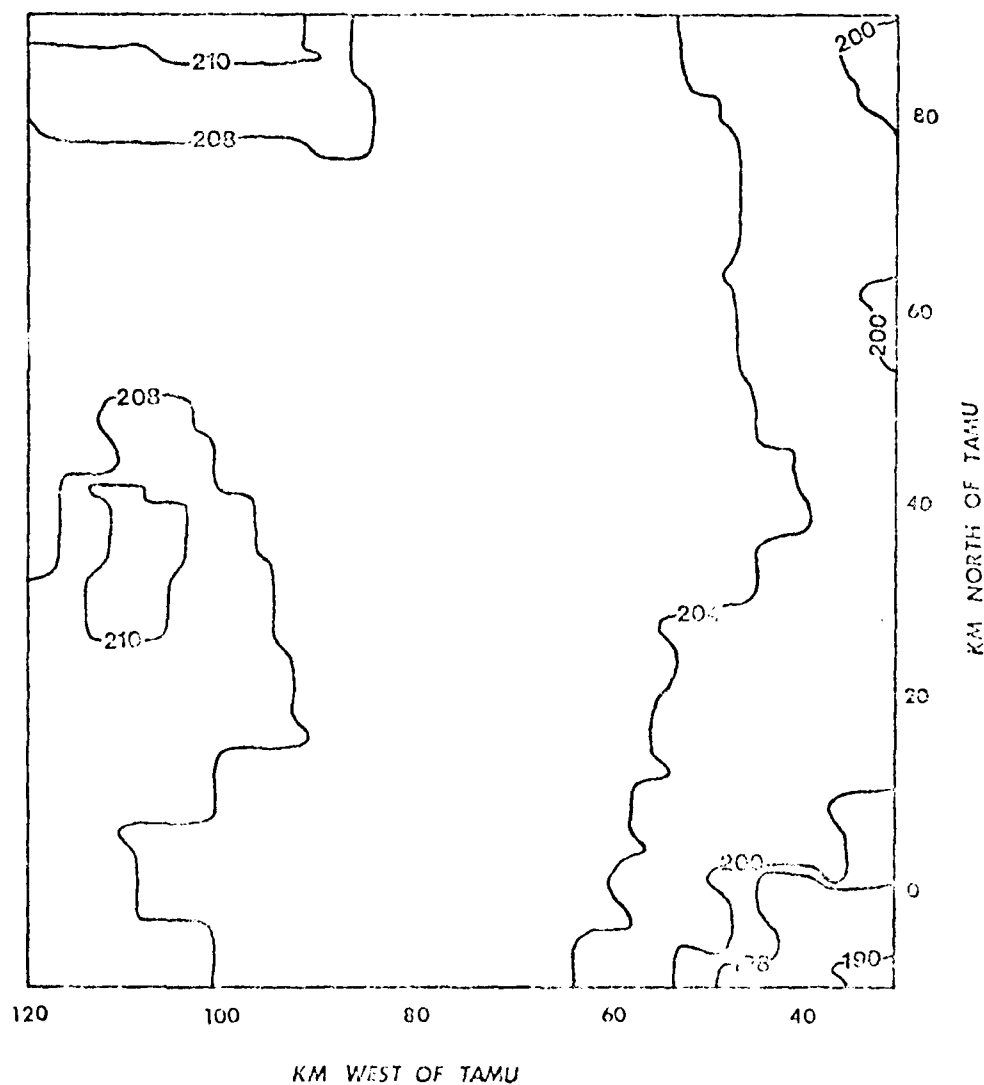


Fig. 9. 0030 GMT, 3 May 1978 infrared image.

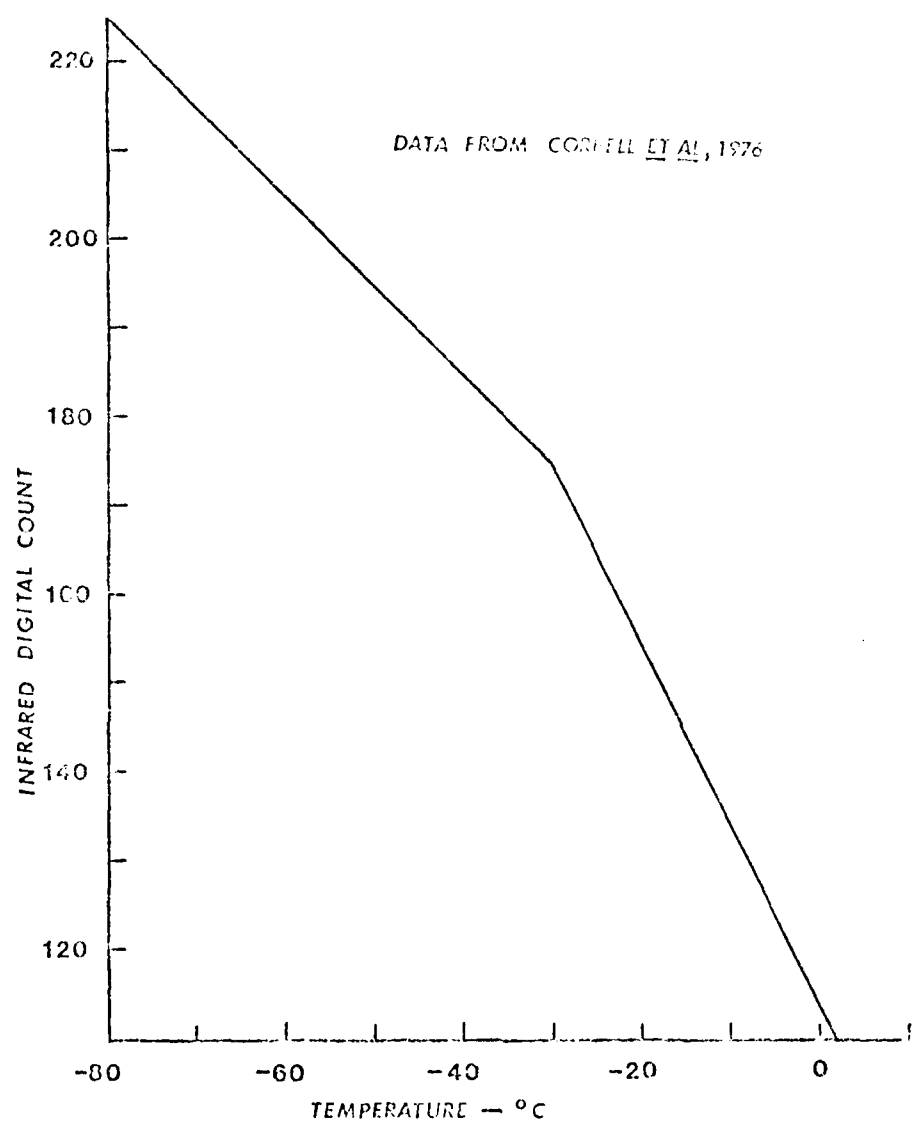


Fig. 10. GOES infrared digital count to temperature calibration.

map (Fig. 3), the low-level PVSZ map (Fig. 4), and in the mid-level PVSZ map (Fig. 5). The best-organized echo activity is located in the western and scale-central portions of Figs. 3 and 4.

The 0015Z infrared image (Fig. 8) has a near-uniform gradient of digital count from high values to low from northwest to southeast. The sharp increase in gradient in the southeastern portion of the image is probably caused by the sensor "looking at" lower-level cloud or the side of convective activity. The shapes of the contours for digital counts of 208 and 210 suggest some association with convective activity as evidenced in that area by Figs. 3, 4, and 5.

The 0030Z infrared image (Fig. 9) has a relatively flat gradient of digital count over much of the mapping. The closed 216 contour suggests its relation to convective cells shown in the same area in Figs. 3, 4, and 5. The relative flatness of the gradient of digital counts on the order of 200 and the disappearance of the low values of digital count in the southeast corner of the image suggest the spreading of cirrus cloud cover over much of the area. Obscuration by the cirrus prevents direct observation of low- and mid-level convective activity by the infrared sensor. This effect, when coupled with the coarser resolution of the infrared sensor as compared with the digital radar, is considered to be one of the chief problems in attempting to relate the two types of data.

3. Tenth Tilt-sequence and Corresponding GOES Images

The tenth digital radar tilt-sequence was collected from 0216 GMT to 0233 GMT on 3 May 1978 using 14 1° changes in antenna inclination. Data from the northwest and southwest sectors of the tilt-sequence were processed by the Sicland computer program. The 0215 GMT and 0230 GMT GOES-East infrared images were used for comparison with both sectors from this tilt-sequence. Maps of zero-tilt reflectivity (dBZ), low-, mid-, and high-level PVSZ (dBZ), and VIL (kg m^{-2}) are presented in Figs. 11, 12, 13, 14, and 15, respectively, for the southwest sector and in Figs. 18, 19, 20, 21, and 22, respectively, for the northwest sector. Maps of contoured infrared digital count from the 0215 GMT and 0230 GMT GOES-East images for corresponding areas are presented for the southwest sector in Figs. 16 and 17 and for the northwest sector in Figs. 23 and 24.

a. Southwest Sector

Significant features to note in the digital radar data include the presence of strong line radar echoes to the south-southwest of TAMU in all of the digital radar maps. The two areas of heaviest convective activity are especially evident in the mid- and upper-level PVSZ maps (Figs. 13 and 14) and in the VIL map (Fig. 15). The two strong cells exhibit very little "tilt" in the vertical in a comparison of Figs. 12 through 14. Maxima in the VIL map also correspond well

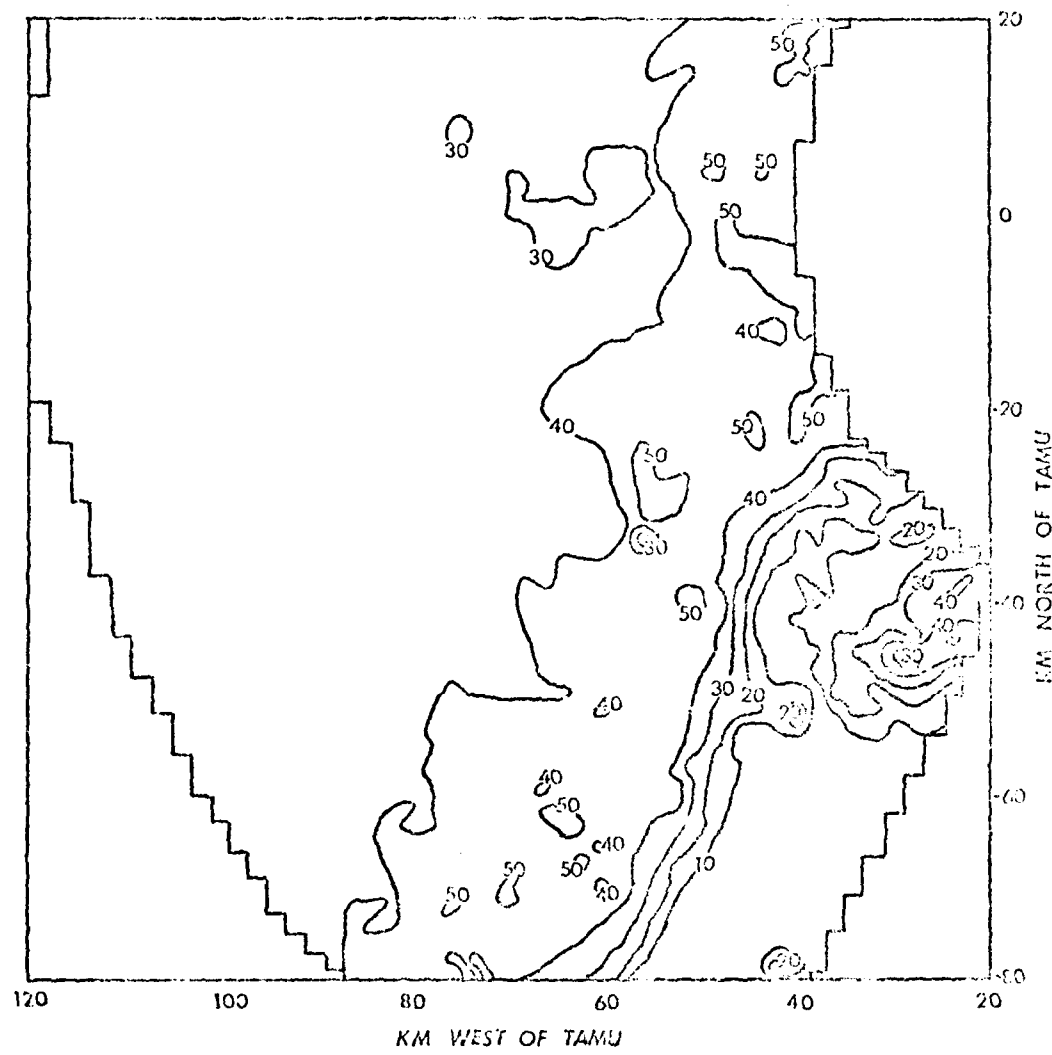


Fig. 11. Tilt-sequence ten, southwest sector, zero-tilt reflectivity (dBZ). Data collected on 3 May 1978 at 0216 GMT.

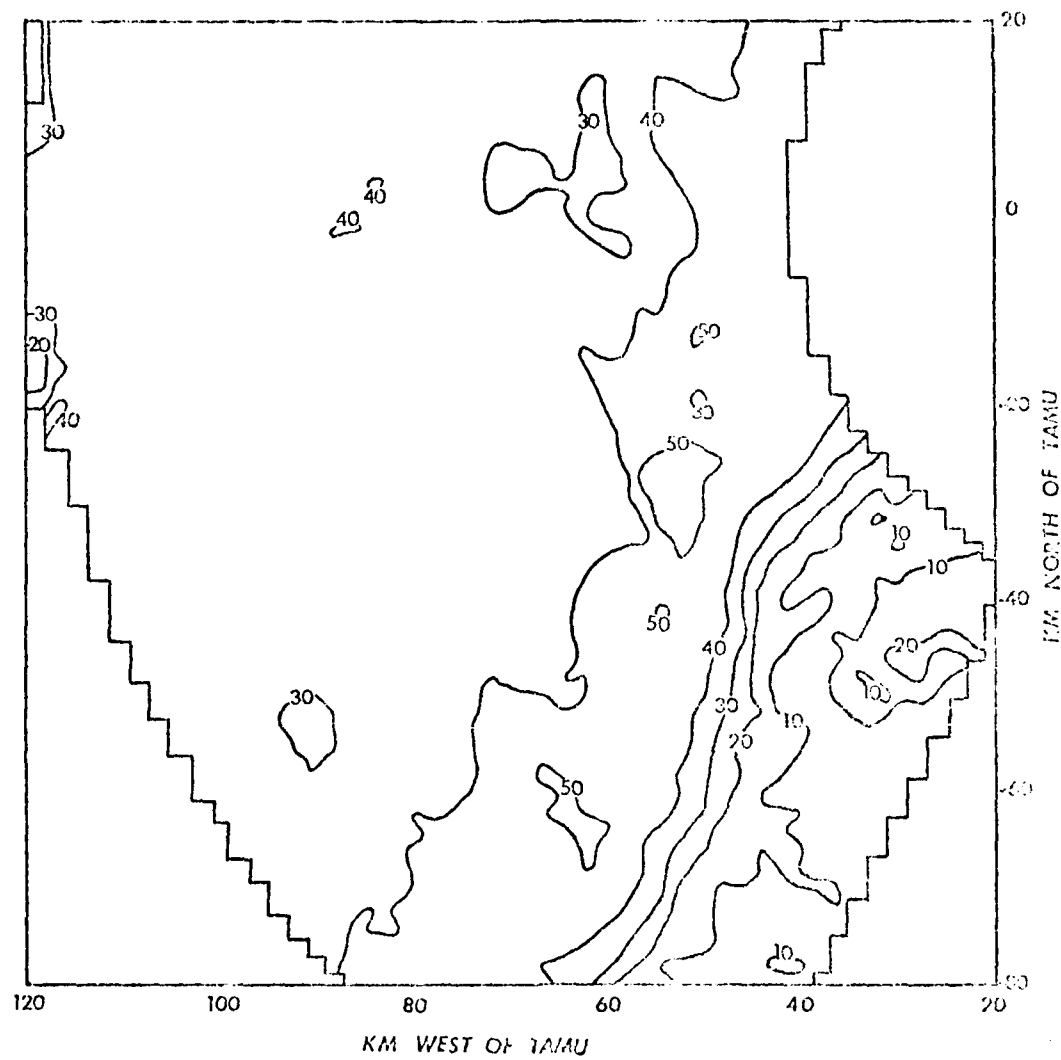


Fig. 12. Tilt-sequence ten, southwest sector, low-level PVSZ (dBZ). Data collected on 3 May 1978 at 0216 GMT to 0233 GMT.

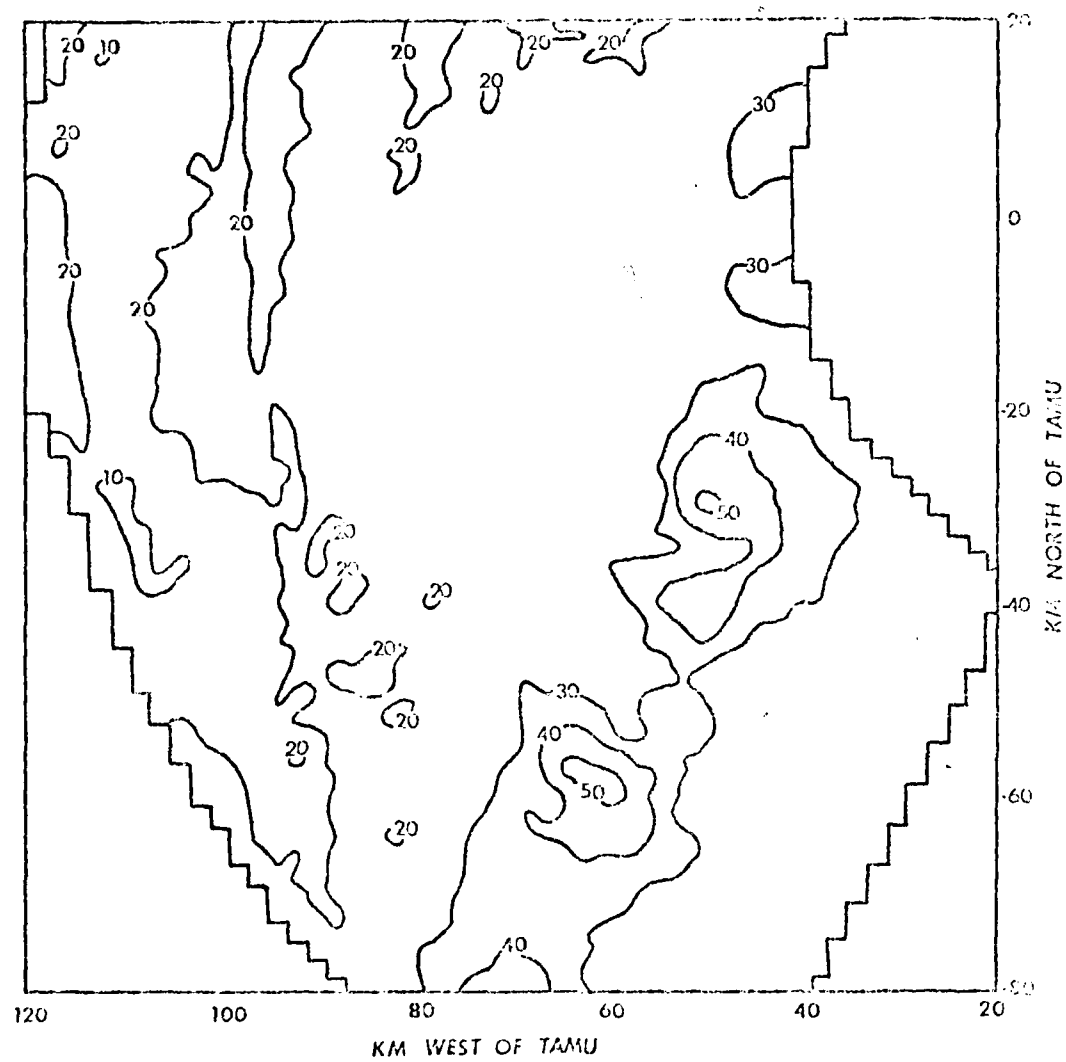


Fig. 13. Tilt-sequence ten, southwest sector, mid-level PVSZ (dBZ). Data collected on 3 May 1978 from 0216 GMT to 0233 CMT.

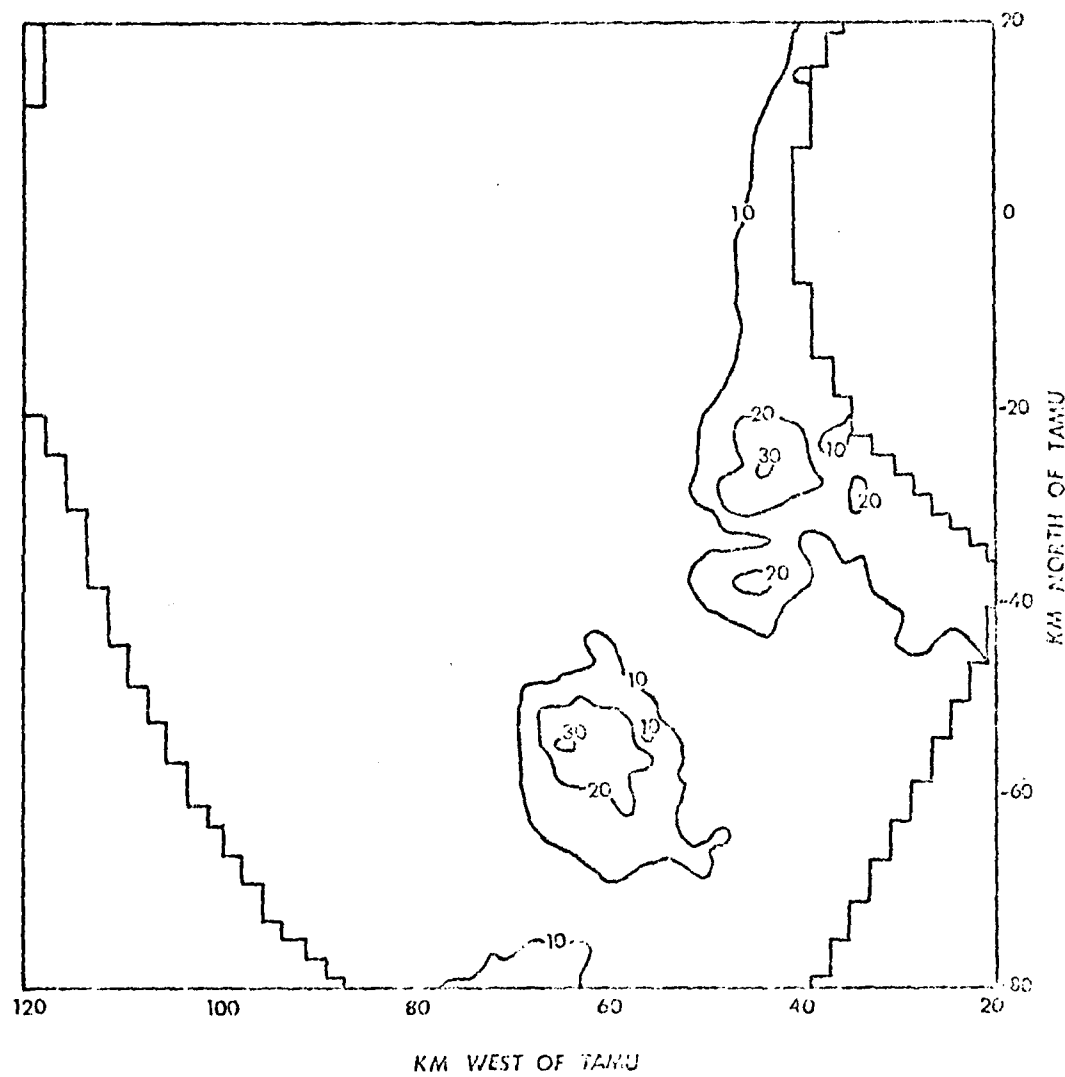


Fig. 14. Tilt-sequence ten, southwest sector, upper-level PVSZ (dBZ). Data collected on 3 May 1978 from 0216 GMT to 0233 GMT.

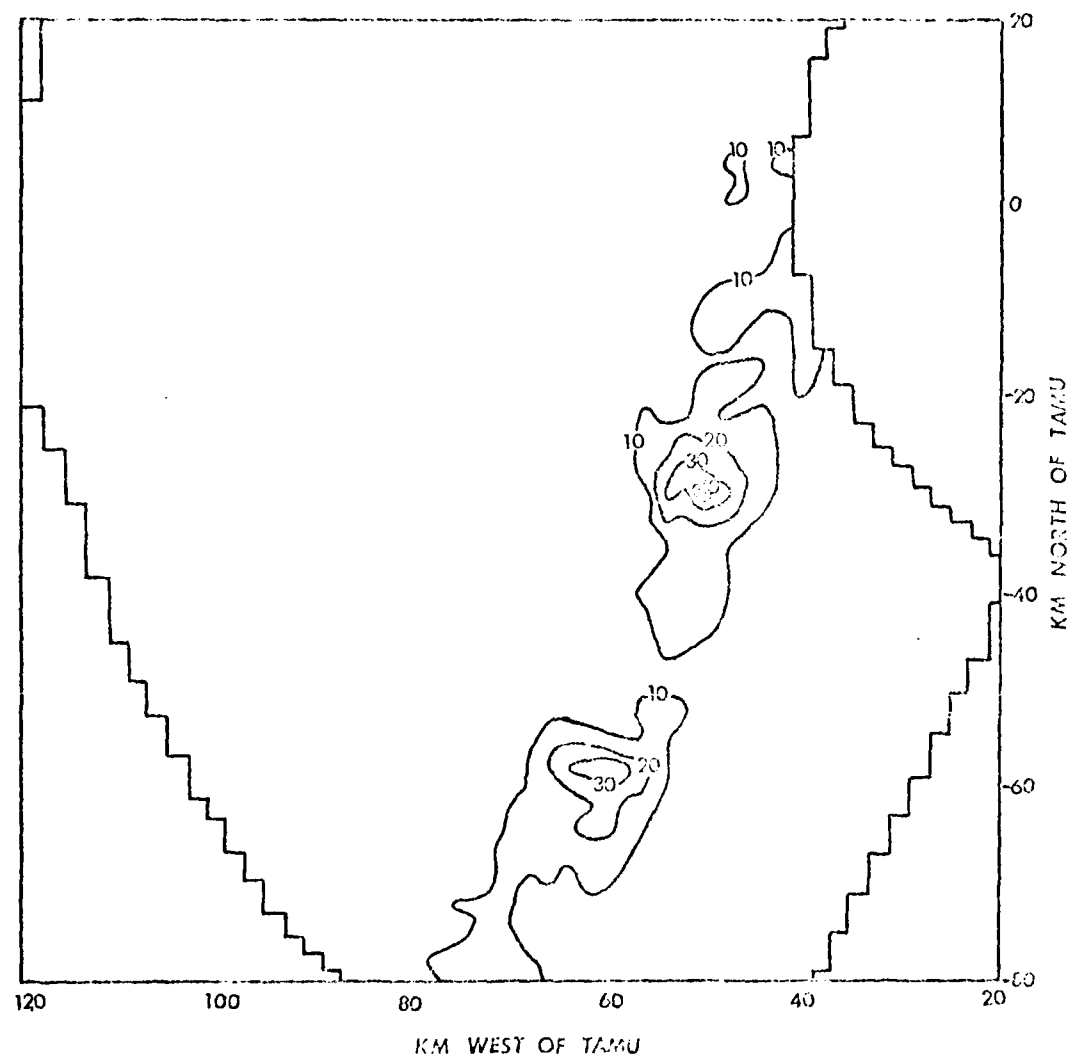


Fig. 15. Tilt-sequence ten, southwest sector, VIL (kg m^{-2}). Data collected on 3 May 1978 from 0216 GMT to 0233 GMT.

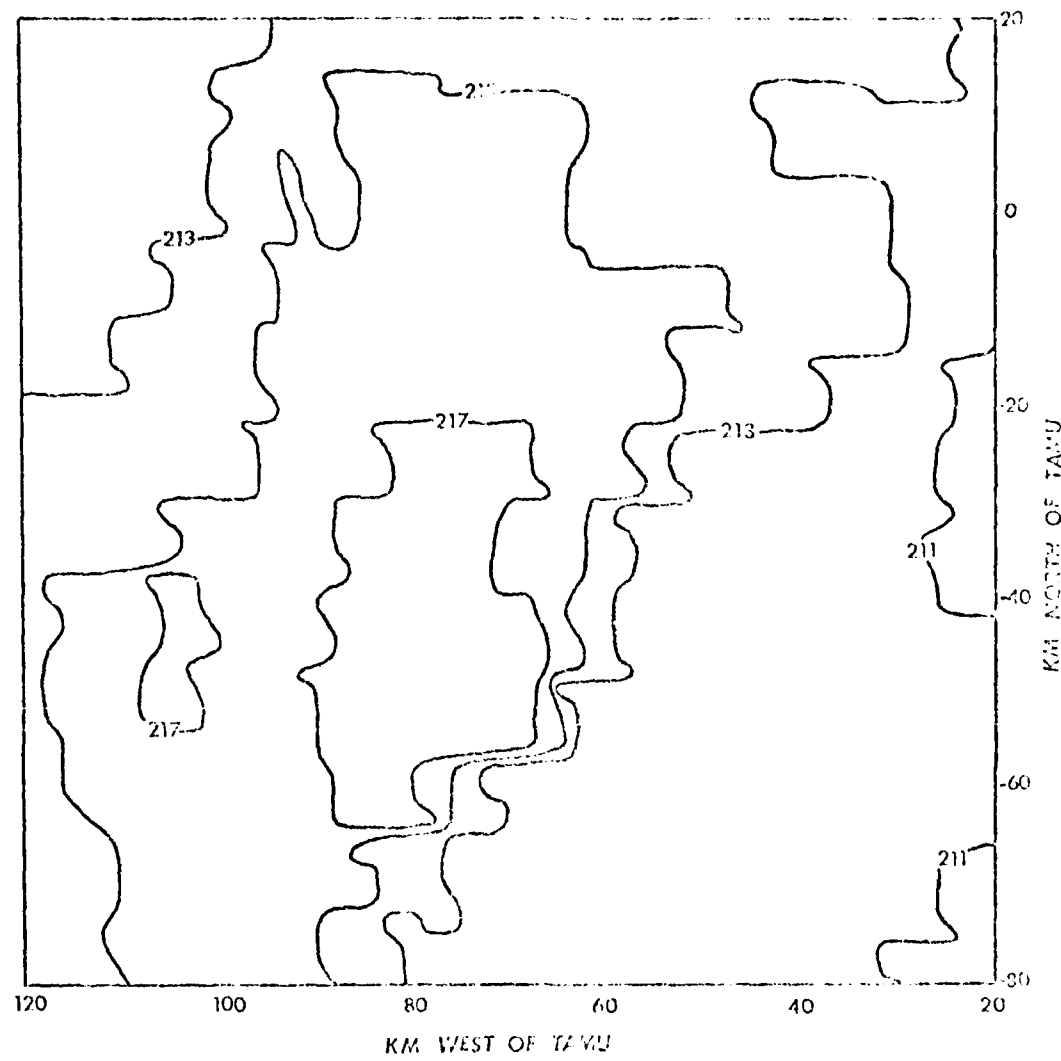


Fig. 16. 0215 GMT, 3 May 1978 infrared image,
southwest sector.

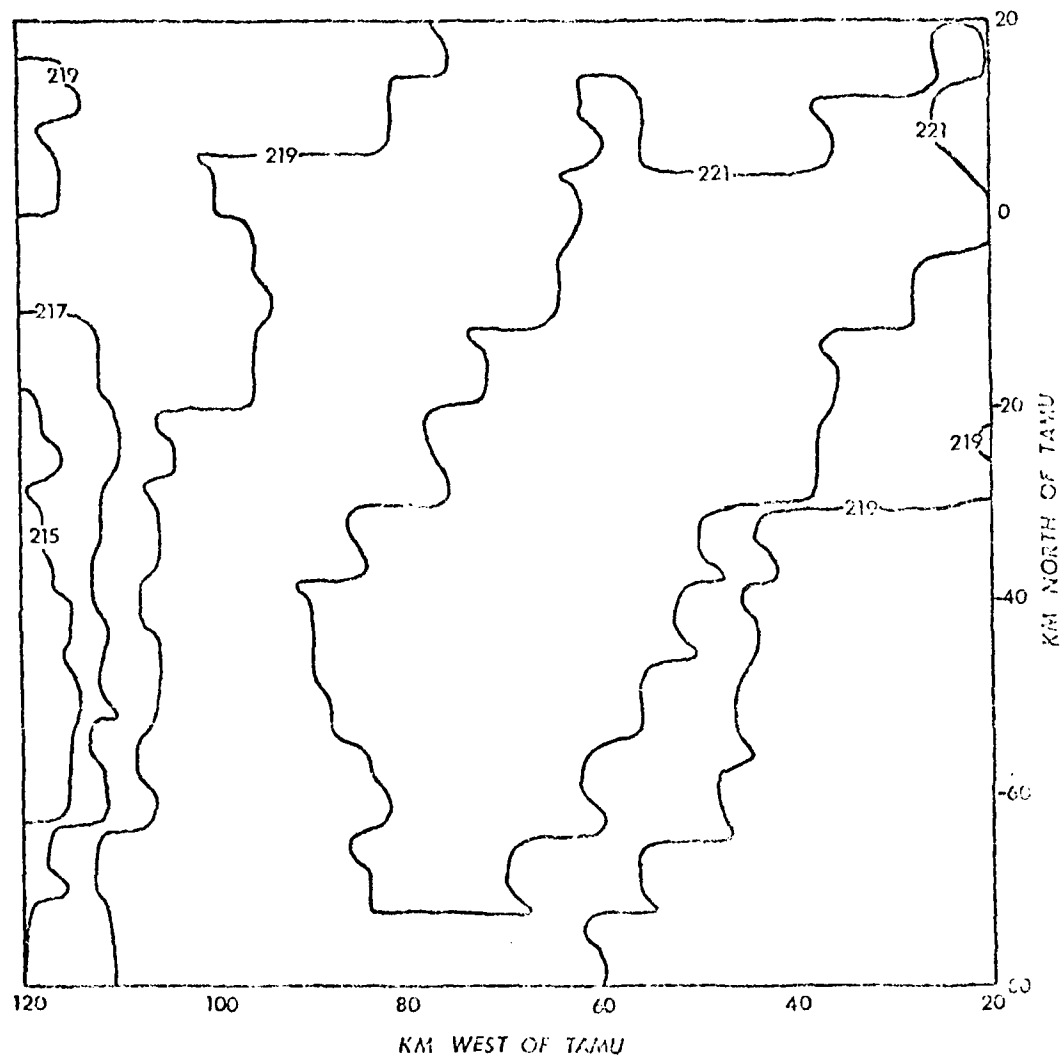


Fig. 17. 0230 GMT, 3 May 1978 infrared image,
southwest sector.

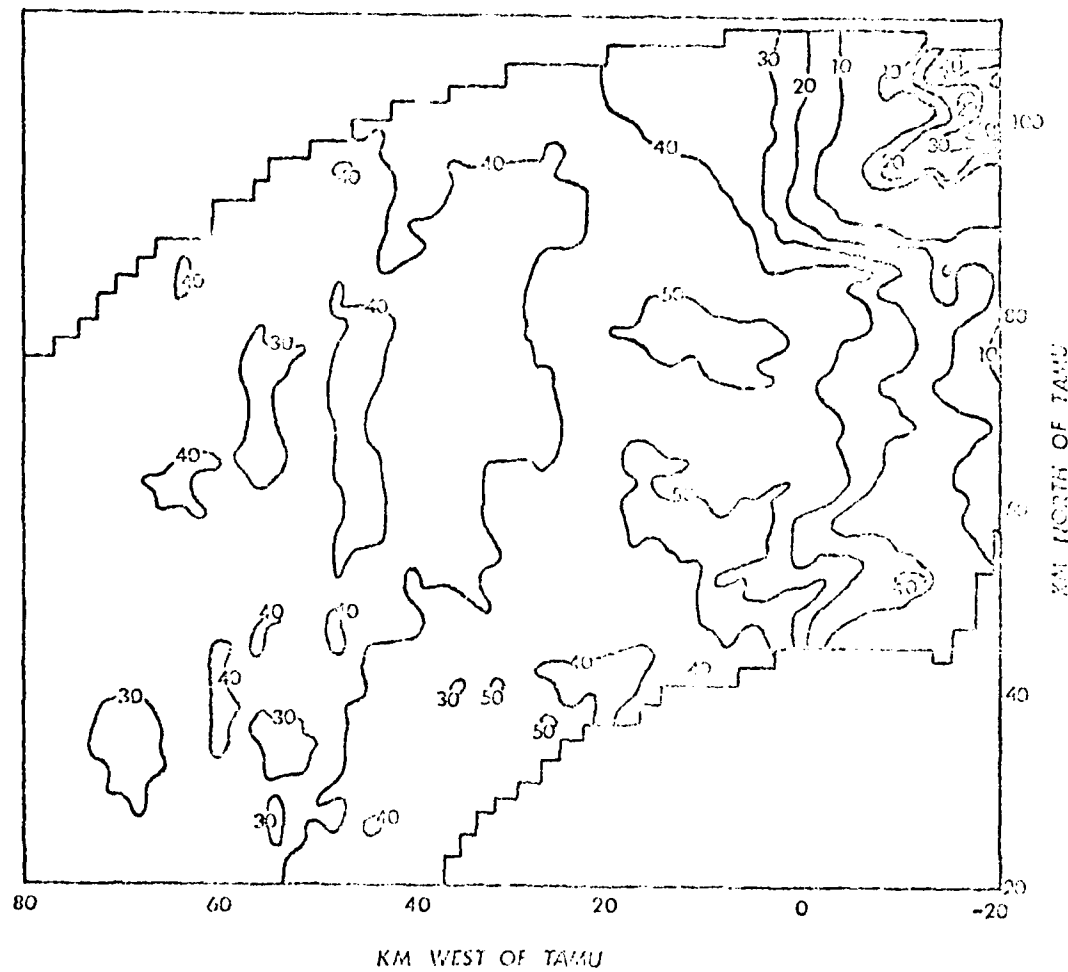


Fig. 18. Tilt-sequence ten, northwest sector, zero-tilt reflectivity (dBZ). Data collected on 3 May 1978 at 0216 GMT.

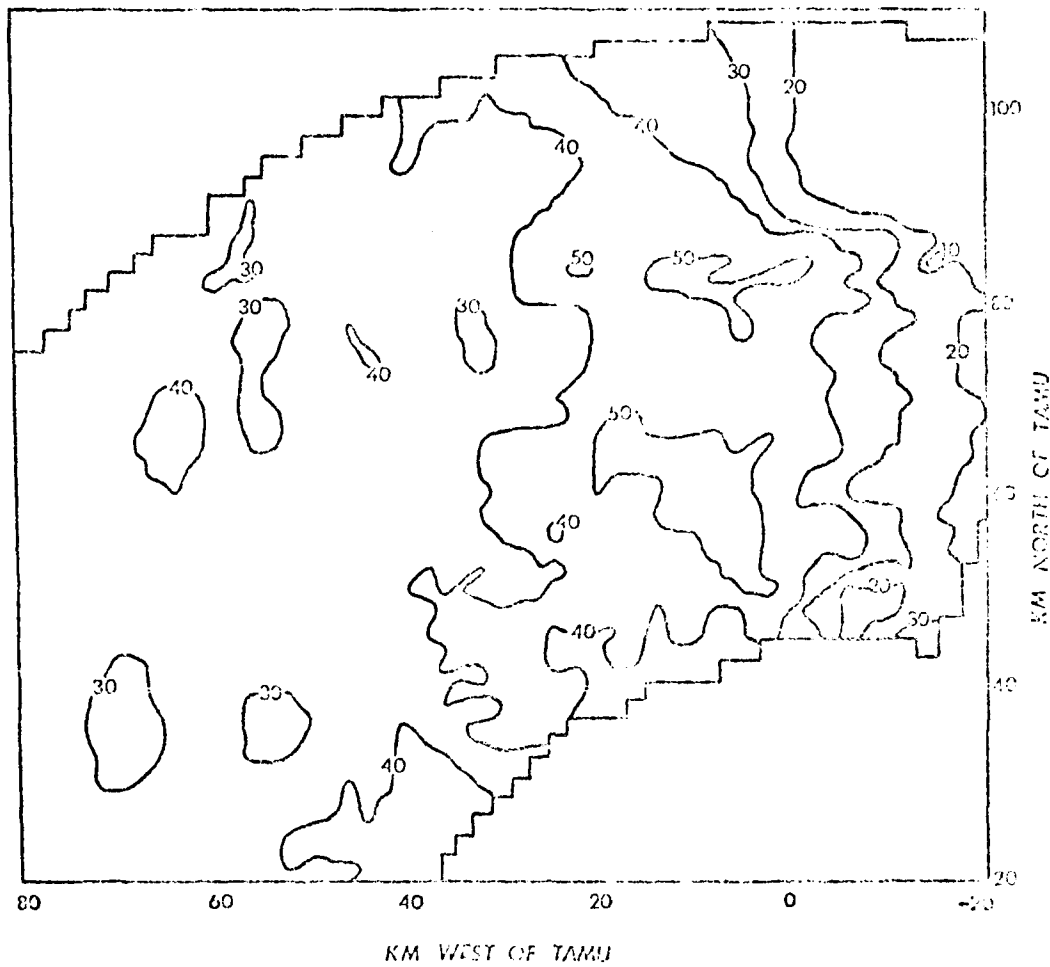


Fig. 19. Tilt-sequence ten, northwest sector, low-level PVSZ (dBZ). Data collected on 3 May 1978 from 0216 GMT to 0233 GMT.

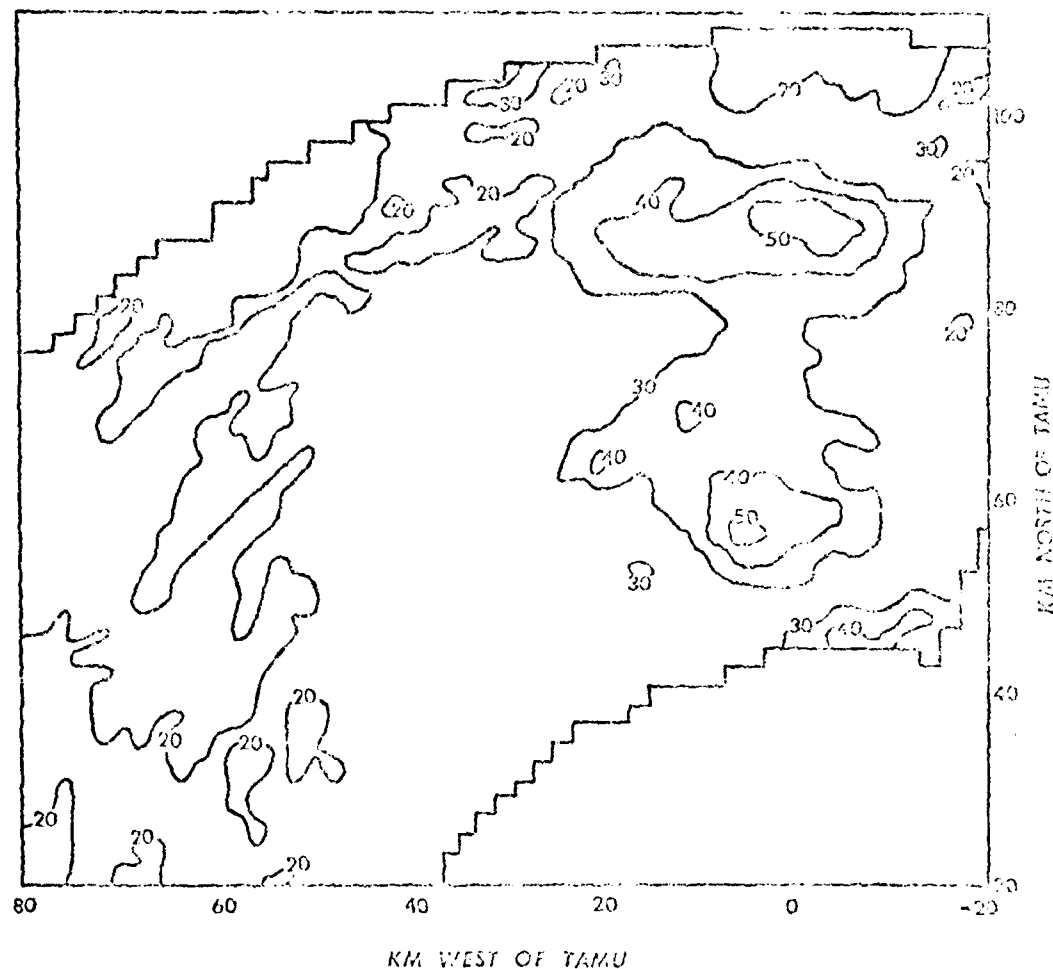


Fig. 20. Tilt-sequence ten, northwest sector, mid-level
PWSZ (dBZ). Data collected on 3 May 1978 from 0216
GMT to 0233 CMT.

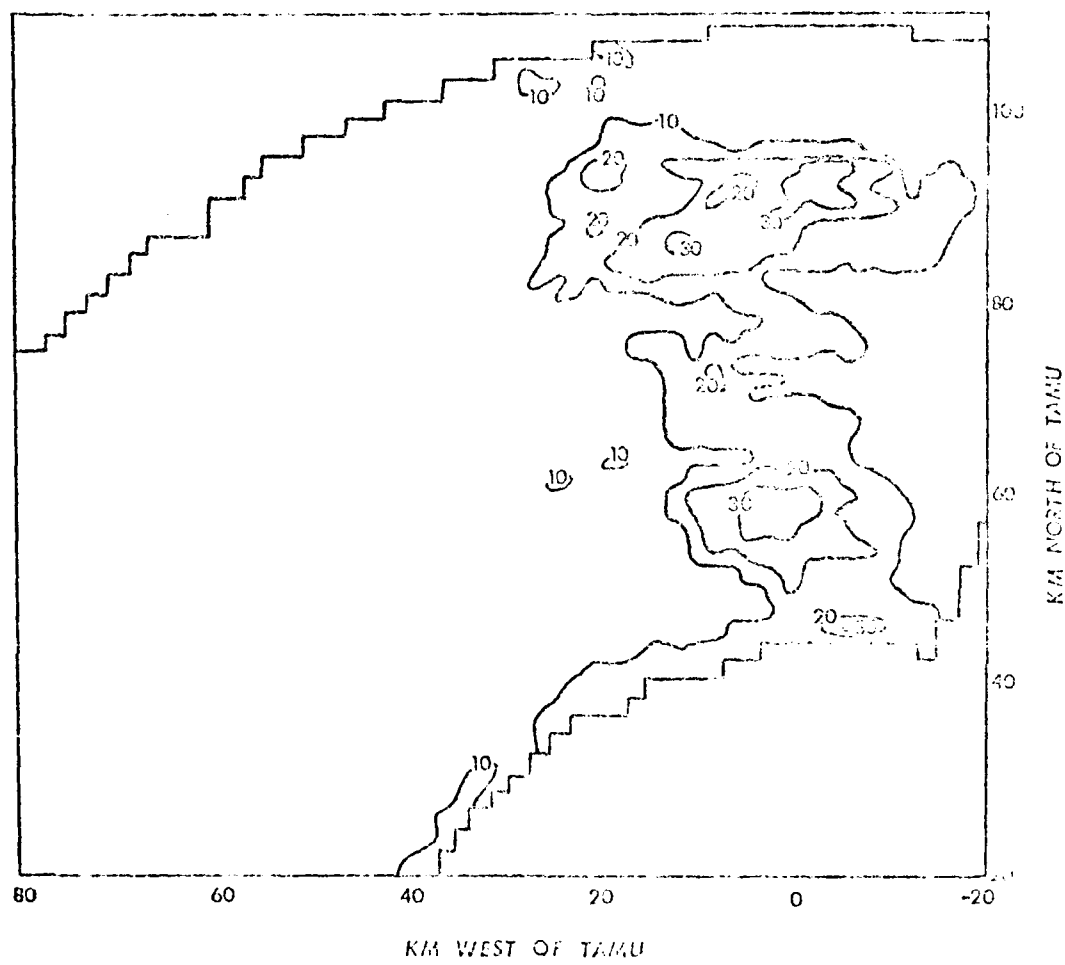


Fig. 21. Tilt-sequence ten, northwest sector, upper-level PVSZ (GBZ). Data collected on 3 May 1978 from 0216 GMT to 0233 GMT.

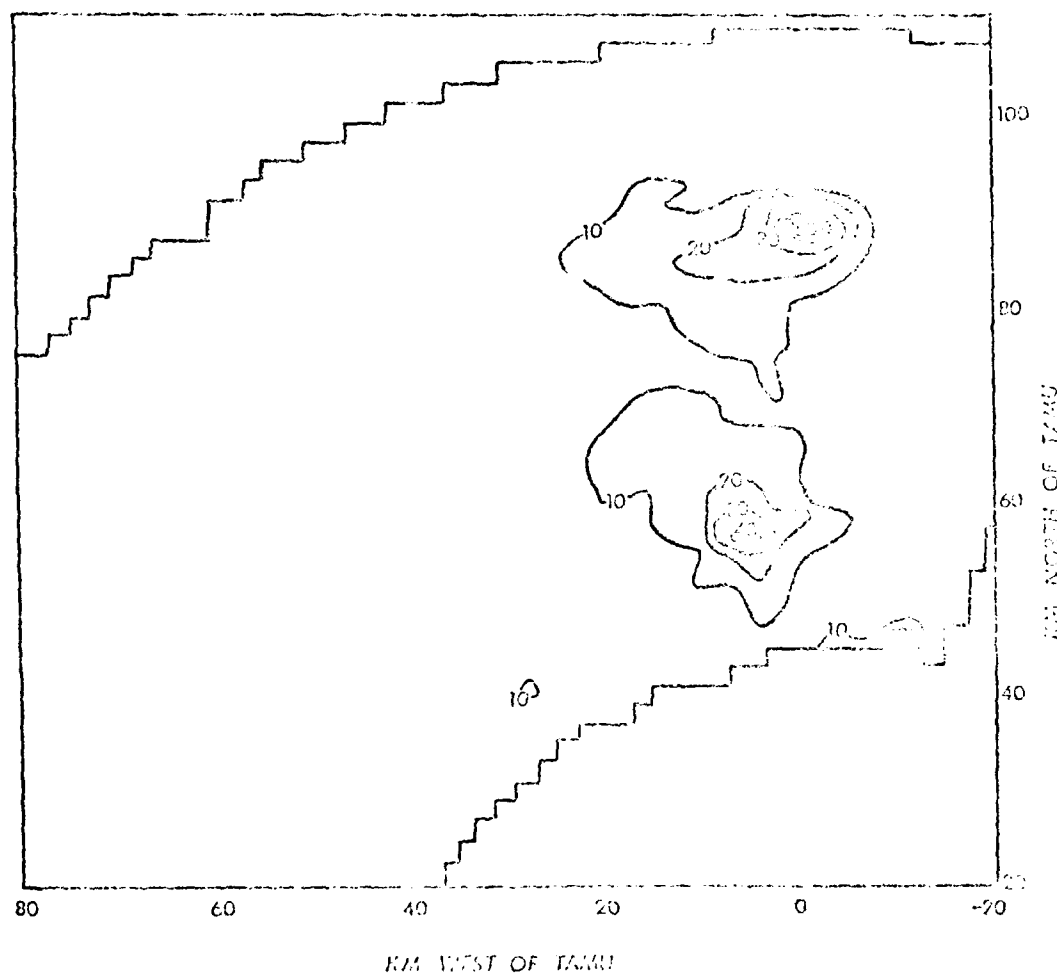


Fig. 22. Tilt-sequence ion, northwest sector, VIL (kg m^{-2}).
Data collected on 3 May 1978 from 0316 GMT to 0233 GMT.

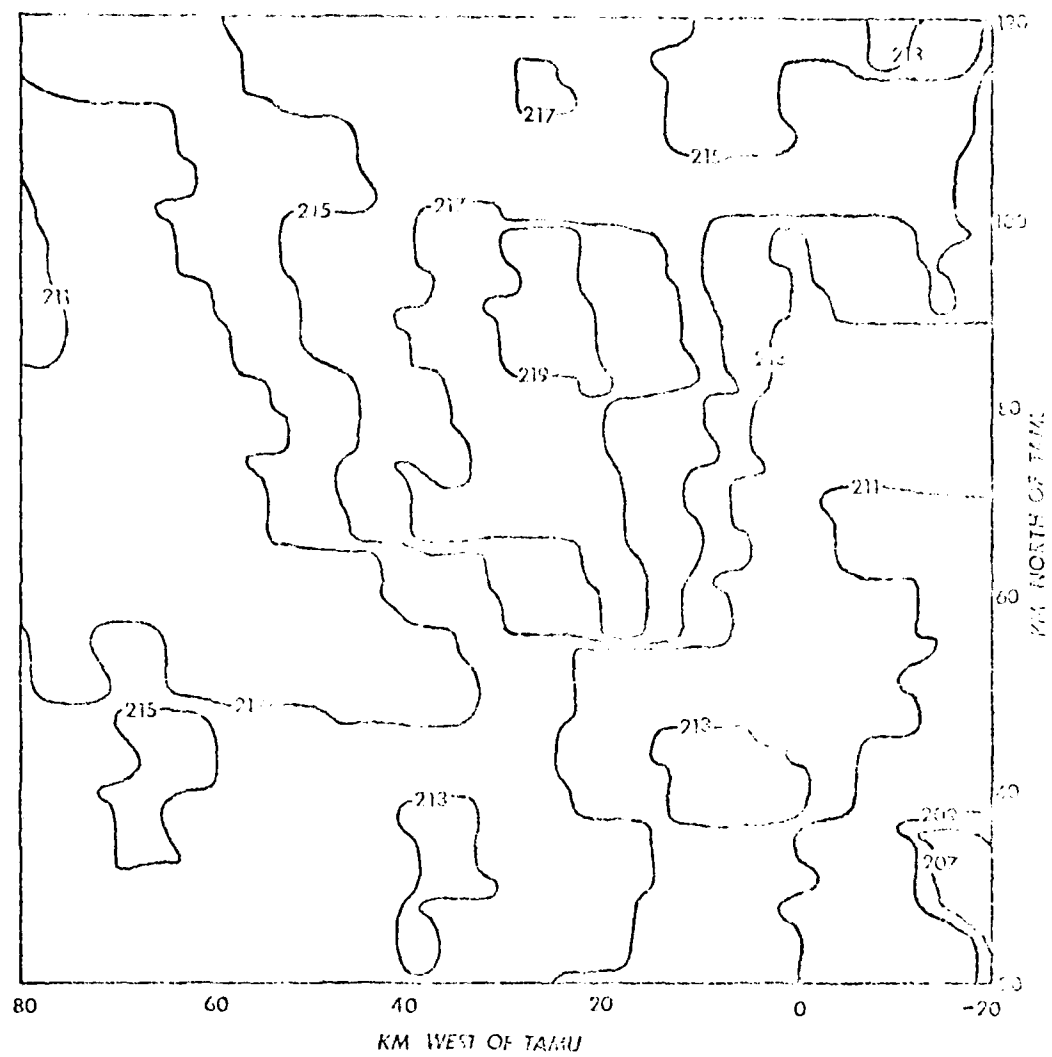


Fig. 23. 0215 GMT, 3 May 1978 infrared image,
northwest sector.

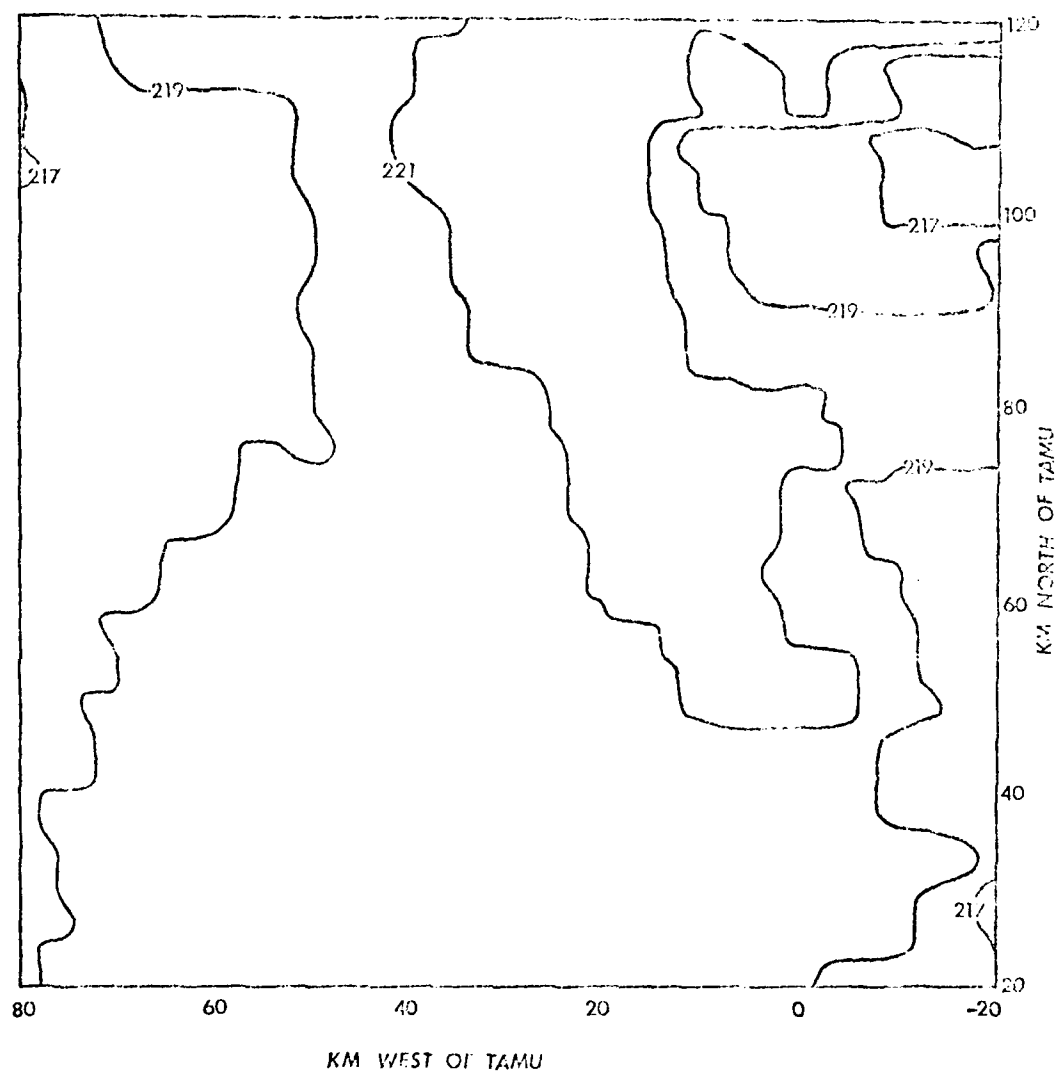


Fig. 24. 0230 GMT, 3 May 1978 infrared image,
northwest sector.

with the location of reflectivity maxima in these same figures.

High values of infrared digital count in both the 0215 GMT and 0230 GMT images (Figs. 16 and 17) lie some 10 km to the west-northwest of radar activity indicated in Figs. 11 through 15. The increase in maximum digital count in going from the 0215 GMT image to the 0230 GMT image is indicative of the strong upper-level outflow associated with the line of convective activity. Regions of maximum digital count in both images lie overlap the maxima in the radar fields, especially in the later infrared image (Fig. 17).

b. Northwest Sector

Strong echo activity is also evident in the radar data for the northwest sector. Strong echoes are present to the north of TAMU with cells in the line activity becoming more evident in the mid- and upper-level PWSZ maps (Figs. 20 and 21). Two cells stand out very well in the VIL map (Fig. 22). Very little tilt is evident in the cells to the north of TAMU although the area of reflectivity associated with each cell in Figs. 19 through 21 is broader with merging of the cells apparently occurring at all levels. The VIL map (Fig. 22) exhibits two sharply bounded cells almost due north of TAMU.

Maximum values of digital count in the 0215 GMT infrared image (Fig. 23) lie 10-15 km to the west of maxima in the radar maps.

Maximum values of digital count in the 0230 GMT infrared image lie slightly to the west of maxima in the digital radar fields. The increase in maximum digital count from 0215 GMT to 0230 GMT again indicates the strong upper-level outflow associated with the convective line.

4. Correlations Between the Radar and Satellite Data

Correlation analysis provides a measure of the degree of association between variables. The correlation used as a measure of association in the remainder of this investigation is Pearson's product-moment correlation with the correlation coefficient, r , being given by

$$r = \frac{\sum_{i=1}^N (X_i - \bar{X})(Y_i - \bar{Y})}{\left[\sum_{i=1}^N (X_i - \bar{X})^2 \sum_{i=1}^N (Y_i - \bar{Y})^2 \right]^{0.5}} \quad (1)$$

where the (X_i, Y_i) represent paired observations of the variables, \bar{X} and \bar{Y} represent arithmetic means of the variables, and N is the total number of paired observations of X and Y . The value of the coefficient, r , is a measure of the degree of association of the variables with a perfect positive association indicated by $r = 1$, a perfect negative correlation indicated by $r = -1$, and a complete lack of correlation between the variables indicated by $r = 0$.

Correlation coefficients were computed using procedures implemented by the SAS 76 statistical analysis system which also returned significance probabilities of the correlation coefficients. The significance probability, p , of a correlation coefficient is the probability that a value of the correlation coefficient as large or larger in absolute value than the one calculated would have arisen by chance were the two random variables truly uncorrelated (Barrett et al., 1976). Correlation coefficients were calculated for three basic data sets: the first tilt-sequence and associated GOES images, the tenth tilt-sequence, southwest sector, and associated GOES images, and the tenth tilt-sequence, northwest sector, and associated images. All values of r were computed using point values of the radar and satellite variables.

An additional satellite data variable was artificially created for each data set by subtracting point values of the digital count of the later GOES image from corresponding values of digital count in the earlier GOES image. Correlation coefficients also were computed between this difference in digital count, d , and the digital radar data.

a. First Tilt-sequence and Corresponding GOES Images

The results of the correlations of the 0015 GMT infrared data, the 0030 GMT infrared data, and d with corresponding digital radar data are tabulated in Table 3. The best correlations were found

Table 3. Values of r and p for the first tilt-sequence and corresponding COMS images.

Satellite Data	Radar Data	r	p
0015 GMT Image	Zero-tilt reflectivity	-0.177	0.0001
	Low-level PV _{0.5}	-0.058	0.0004
	Mid-level PV _{0.5}	0.372	0.0001
	Upper-level PV _{0.5}	0.105	0.0001
	VIL	0.128	0.0001
0030 GMT Image	Zero-tilt reflectivity	0.019	0.393*
	Low-level PV _{0.5}	0.120	0.0001
	Mid-level PV _{0.5}	0.496	0.0001
	Upper-level PV _{0.5}	0.184	0.0001
	VIL	0.247	0.0001
Difference, d	Zero-tilt, 0015-0030 PV	0.216	0.0001
	Low-level PV _{0.5}	0.105	0.0001
	Mid-level PV _{0.5}	-0.295	0.0001
	Upper-level PV _{0.5}	-0.070	0.0005
	VIL	-0.079	0.0003
Number of Obs. (n) = 1063			

between the 0015 GMT and 0030 GMT images and mid-level PVSZ data. Weak and sometimes negative correlation coefficients were found between both infrared images and zero-tilt reflectivity and low-level PVSZ. Weak positive correlations are indicated for both images and upper-level PVSZ and VIL. The results for the point differences in digital counts between images and the radar data are ambiguous with a weak positive correlation between d and zero-tilt reflectivity and low-level PVSZ and negative correlations with the remaining radar data fields.

b. Tenth Tilt-sequence, Southwest Sector, and Corresponding GOES Images

The results of correlations of the 0315 GMT infrared data, the 0230 GMT infrared data, and d with the corresponding digitized radar data from the southwest sector of the tenth tilt-sequence are tabulated in Table 4. The best correlations in this data set were between mid-level and upper-level PVSZ and d , the difference between digital counts for the 0230 GMT and 0215 GMT images. Fair positive correlations also were found between d and VIL and between the 0230 GMT image and zero-tilt reflectivity and low-level PVSZ. Somewhat weaker correlations were found between the 0230 GMT image and mid- and upper-level PVSZ and VIL. Weak positive correlations were found between the 0215 GMT image and zero-tilt reflectivity and low-level

Table 4. Values of r and p for the tenth tilt-sequence and corresponding GOES images (southwest sector).

Satellite Data	Radar Data	r	p
0215 GMT Image	Zero-tilt reflectivity	0.317	0.0001
	Low-level PVSZ	0.332	0.0001
	Mid-level PVSZ	-0.344	0.0001
	Upper-level PVSZ	-0.399	0.0001
	VIL	-0.221	0.0001
0230 GMT Image	Zero-tilt reflectivity	0.541	0.0001
	Low-level PVSZ	0.530	0.0001
	Mid-level PVSZ	0.389	0.0001
	Upper-level PVSZ	0.275	0.0001
	VIL	0.401	0.0001
Difference, d	Zero-tilt reflectivity	0.063	0.0050
	Low-level PVSZ	0.037	0.1034
	Mid-level PVSZ	0.648	0.0001
	Upper-level PVSZ	0.624	0.0001
	VIL	0.527	0.0001

Number of Observations = 1986

PVSZ. Negative correlations existed between the 0215 GMT image and mid-level and upper-level PVSZ and VIL. Zero-tilt reflectivity and low-level PVSZ were essentially uncorrelated with d .

c. Tenth Tilt-sequence, Northwest Sector, and Corresponding CCWS Images

Table 5 lists the results of correlations of 0215 GMT infrared data, 0230 GMT infrared data, and d with the corresponding digital radar data from the northwest sector of the tenth tilt-sequence. The best correlations in this data set were between the 0230 GMT infrared data and zero-tilt reflectivity and low-level PVSZ. Weaker positive correlations were found between the 0230 GMT infrared data and the remaining digital radar fields. Correlations between d and the digital radar fields, while positive and significant, were weaker than those found for the same data fields in the northeast sector. Except for weak positive correlations between the 0230 GMT infrared data and zero-tilt reflectivity and low-level PVSZ, the 0230 GMT infrared data were uncorrelated with the digital radar data.

5. The Effect of Thresholding the Data

Enhanced infrared imagery from meteorological satellites has proved useful in detecting the presence of severe convective activity, in examining the structure of convective storm systems, and in estimating the amount of precipitation from convective storm systems.

Table 5. Values of r and p for the tenth tilt-sequence and corresponding GOES images (northwest sector).

Satellite Data	Radar Data	r	p
0215 CMT Image	Zero-tilt reflectivity	0.138	0.0001
	Low-level PVSZ	0.167	0.0001
	Mid-level PVSZ	-0.014	0.5557
	Upper-level PVSZ	-0.091	0.0001
	VIL	0.003	0.7559
0230 CMT Image	Zero-tilt reflectivity	0.598	0.0001
	Low-level PVSZ	0.592	0.0001
	Mid-level PVSZ	0.373	0.0001
	Upper-level PVSZ	0.205	0.0001
	VIL	0.387	0.0001
Difference, d	Zero-tilt reflectivity	0.179	0.0001
	Low-level PVSZ	0.196	0.0001
	Mid-level PVSZ	0.246	0.0001
	Upper-level PVSZ	0.270	0.0001
	VIL	0.232	0.0001
Number of Observations = 1721			

Enhancing infrared images requires selecting various "thresholds" in the data and assigning various shades of grey in the "grey scale" to data bounded by the thresholds. These thresholds may then be used to produce patterns in the infrared data characteristic of various stages in the development of phenomena such as hurricanes and squall lines.

An example of an enhancement applied to infrared imagery is the MB enhancement curve shown in Fig. 25 and tabulated in Table 6. The MB enhancement is applied to GOES infrared imagery as a means of delineating areas of thunderstorm activity in the images. The very cold tops typically associated with areas of intense convective activity are thresholded in the grey scale as areas of dark and black tones seen against the lighter background of lower-level, warmer clouds in the hard copy imagery. A reversal of the scale from black to white is used to identify the strongly penetrative tops indicative of severe thunderstorm activity (Cerbell *et al.*, 1976).

a. Thresholding the Infrared Data

Selected digital count thresholds corresponding to levels employed in the MB enhancement curve were applied to the data used in this investigation. All infrared data having digital counts less than the threshold digital count and corresponding radar data were excluded from that step in the analysis. Due to the limited range of

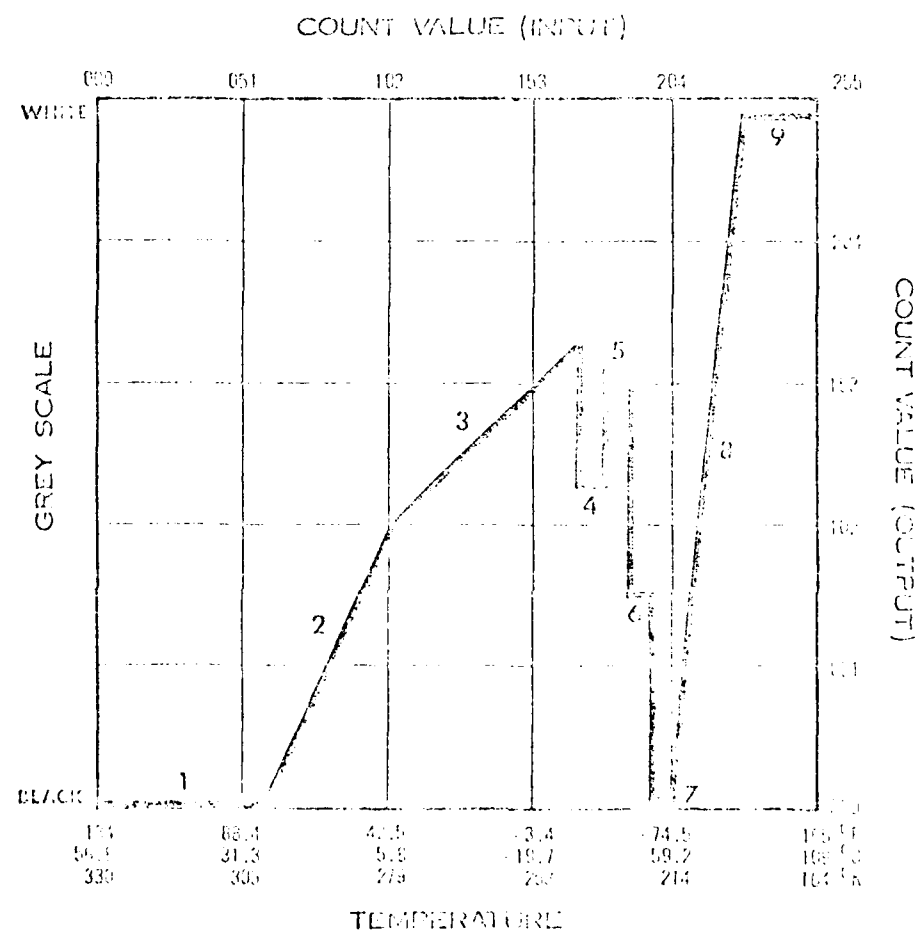


Fig. 25. MB enhancement curve (after Corbell *et al.*, 1976).

Table 6. MB enhancement (after Corbelli et al., 1975).

Digital Count Threshold	Temperature (K)	Remarks (Grey Scale Shade)
057	301.5	Low level/no surface difference
100	280.0	Middle level - no enhancement
177	241.0	First level of four (Medium grey)
187	231.0	Thunderstorm enhancement (Light grey)
198	220.0	Thunderstorm enhancement (Dark grey)
204	214.0	Thunderstorm enhancement (Black)
208	210.0	Overshooting tops enhancement (White)
226	192.0	

digital count values associated with the portions of the 0215 GMT and 0230 GMT infrared images used and the high values of digital count in the images, the data for the tenth tilt-sequence and corresponding infrared data were excluded from this portion of the analysis. The remaining data set, the first tilt-sequence and 0015 GMT and 0030 GMT infrared images, was examined using four threshold values of infrared digital count. Table 7 presents the correlation coefficients resulting from the correlation of thresholded infrared data with corresponding digital radar data.

Thresholding the 0015 GMT infrared image improved the correlation between the infrared data and the digital radar data for threshold digital counts of 187 and 193. The correlations between infrared image data and all radar data except upper-level PVSZ were markedly improved when the 193 digital count threshold was evaluated. Increasing the threshold digital count for this image to 204 worsened the correlation, possibly due to reduced sample size as well as other factors. Thresholding the 0030 GMT results produced similar results for the 193 digital count threshold in that all correlations were somewhat improved. The 204 and 208 digital count thresholds improved correlations with zero-tilt reflectivity and low-level PVSZ, while the correlation with mid-level PVSZ diminished. The correlation with upper-level PVSZ remained essentially the same.

AD-A110 365 AIR FORCE INST OF TECH WRIGHT-PATTERSON AFB OH
DIGITAL METEOROLOGICAL RADAR DATA COMPARED WITH DIGITAL INFRARE--ETC(U)
MAY 79 R S HENDERSON
UNCLASSIFIED AFIT-CI-79-278T-5 F/6 4/2

-NL

2 OF 2

AD-A110 365

END
03-182
DTIC

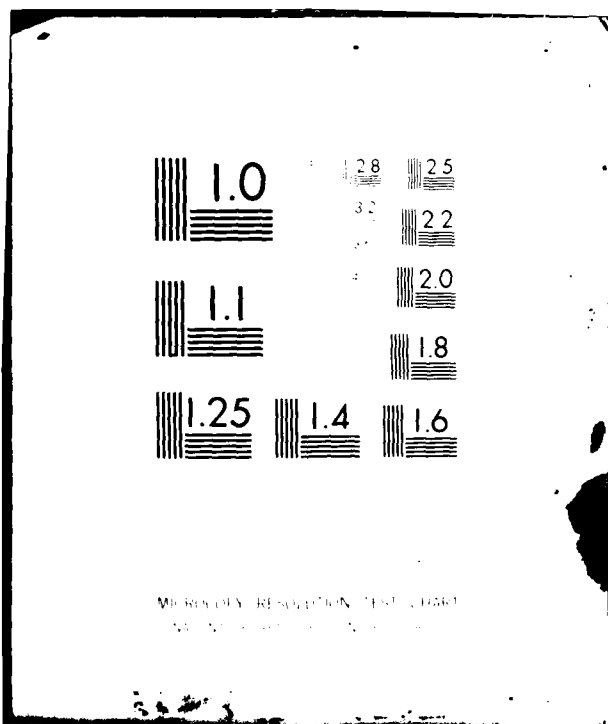


Table 7. Values of r and σ for the first tilt-sequence and thresholded GONS images.

Digital Count Threshold	Infrared Image Time (GMT)	Radar Data	r	σ	Number of Observations
187	0015	Zero-tilt reflectivity	0.109	0.0001	
		Low-level PVSZ	0.121	0.0001	
		Mid-level PVSZ	0.141	0.0001	
		Upper-level PVSZ	0.121	0.0001	
		VIL	0.233	0.0001	
0030	0030	Zero-tilt reflectivity	0.019	0.3837	
		Low-level PVSZ	0.120	0.0001	
		Mid-level PVSZ	0.125	0.0001	
		Upper-level PVSZ	0.124	0.0001	
		VIL	0.247	0.0001	
198	0015	Zero-tilt reflectivity	0.476	0.0001	
		Low-level PVSZ	0.454	0.0001	
		Mid-level PVSZ	0.520	0.0001	
		Upper-level PVSZ	0.167	0.0001	
		VIL	0.388	0.0001	
0030	0030	Zero-tilt reflectivity	0.038	0.0002	
		Low-level PVSZ	0.131	0.0001	
		Mid-level PVSZ	0.569	0.0001	
		Upper-level PVSZ	0.186	0.0001	
		VIL	0.382	0.0001	

Table 7. (Continued)

Digital Count Threshold	Infrared Image Time (GMT)	Radar Data	r	p	Number of Observations
198	0030	VIL	0.255	0.0001	2652
204	0015	Zero-tilt reflectivity Low-level PVSZ Mid-level PVSZ Upper-level PVSZ VIL	0.448 0.335 0.167 0.056 0.259	0.0001 0.0001 0.0001 0.1652 0.0001	505
	0030	Zero-tilt reflectivity Low-level PVSZ Mid-level PVSZ Upper-level PVSZ VIL	0.176 0.192 0.369 0.197 0.251	0.0001 0.0001 0.0001 0.0001 0.0001	1675
208	0015	Zero-tilt reflectivity Low-level PVSZ Mid-level PVSZ Upper-level PVSZ VIL	-0.494 -0.673 -0.551 -0.113 -0.644	0.0002 0.0001 0.0001 0.4207 0.0001	53
	0030	Zero-tilt reflectivity Low-level PVSZ Mid-level PVSZ Upper-level PVSZ VIL	0.306 0.385 0.261 0.143 0.355	0.0001 0.0001 0.0001 0.6932 0.0001	343

the thresholding process. The correlation with VIL was generally improved by the thresholding process with the best correlation at digital counts at and above 208.

b. Thresholding the Digital Radar Data

The thresholding process was extended to the digital radar data as well and correlation coefficients were computed between the radar and satellite data. The initial thresholding was performed by examining only radar data with nonzero values for the variables. In a few isolated cases a slight improvement in correlations between the satellite data and zero-tilt reflectivity was observed. In all other cases the correlation was diminished, markedly so in some instances.

To examine further the effect of thresholding the digital radar data, arbitrary thresholds were selected and correlation coefficients computed between the radar and satellite data. Threshold levels of 10 dBZ were selected for zero-tilt reflectivity, low-level PVSZ, and mid-level PVSZ data. A threshold level of 5 dBZ was selected for the upper level PVSZ data and of 5 kg m^{-2} for the VIL data. Correlation coefficients computed for the thresholded radar data and corresponding infrared images are listed in Table 8.

Thresholding the radar data in the first tilt-sequence improved the correlation between zero-tilt reflectivity, low-level PVSZ, and mid-level PVSZ and both infrared images. No improvement was

Table 8. Values of r and p for thresholded radar data and GOES images.

Tilt-sequence	Infrared Data	Radar Data	r	p	Number of Observations
First	0015 GMT Image	Zero-tilt reflectivity Low-level PvSZ Mid-level PvSZ Upper-level PvSZ VIL	0.072 0.299 0.247 0.293 0.081	0.0136 0.0001 0.0001 0.0257 0.5009	1186 1173 1311 53 72
	0030 GMT Image	Zero-tilt reflectivity Low-level PvSZ Mid-level PvSZ Upper-level PvSZ VIL	0.142 0.356 0.310 0.397 -0.123	0.0001 0.0001 0.0001 0.0009 0.3022	1186 1173 1311 53 72
Difference, d		Zero-tilt reflectivity Low-level PvSZ Mid-level PvSZ Upper-level PvSZ VIL	-0.049 -0.256 -0.265 -0.201 0.032	0.0023 0.0001 0.0001 0.1307 0.749	1186 1173 1311 58 72
Tenth, Southwest Sector	0215 GMT Image	Zero-tilt reflectivity Low-level PvSZ Mid-level PvSZ Upper-level PvSZ VIL	0.035 0.155 -0.357 -0.304 -0.301	0.1073 0.0001 0.0001 0.0004 0.0004	1841 1860 1968 724 433
	0230 GMT Image	Zero-tilt reflectivity Low-level PvSZ	0.500 0.454	0.0001 0.0003	1841 1860

Table 8. (Continued)

Tilt-sequence	Infrared Data	Radar Data	r	p	Number of Observations
Tenth, Southwest Sector	0230 GMT Image	Mid-level Upper-level VIL	0.367 0.092 0.117	0.0001 0.0131 0.0150	1958 724 433
Difference, d		Zero-tilt reflectivity	0.314	0.0001	1841
		Low-level PvSZ	0.132	0.0001	1660
		Mid-level PvSZ	0.617	0.0001	1969
		Upper-level PvSZ	0.452	0.0001	724
		VIL	0.406	0.0001	433
Tenth, Northwest Sector	0215 GMT Image	Zero-tilt reflectivity	0.261	0.0001	1663
		Low-level PvSZ	0.222	0.0001	1684
		Mid-level PvSZ	-0.514	0.5557	1721
		Upper-level PvSZ	-0.623	0.5674	501
		VIL	-0.138	0.6365	475
0230 GMT		Zero-tilt reflectivity	0.603	0.0001	1663
Image		Low-level PvSZ	0.537	0.0001	1684
		Mid-level PvSZ	0.273	0.0001	1721
		Upper-level PvSZ	0.519	0.0002	601
		VIL	0.006	0.8639	475
Difference, d		Zero-tilt reflectivity	0.099	0.0001	1663
		Low-level	0.116	0.0001	1684
		Mid-level	0.245	0.0001	1721
		Upper-level	0.038	0.0001	601
		VIL	0.151	0.0010	475

obtained in the other correlations or for correlations of the radar data with d.

Thresholding the radar data in the southwest sector of the tenth tilt-sequence improved the correlation of d with zero-tilt reflectivity and low-level PVSZ but did not improve any other correlation in the data set. Thresholding the radar data in the northwest sector of the tilt-sequence improved the correlation of both infrared images with zero-tilt reflectivity and of the 0215 GMT image with low-level PVSZ. The remaining correlations were not improved by the thresholding process.

Simultaneous thresholding of both the digital radar and digital satellite data was not attempted since only data from the first tilt-sequence and corresponding imagery could have been used. Reduced sample size in such thresholding probably would have resulted in misleading or erroneous results, particularly for comparisons with upper-level PVSZ and VIL.

CHAPTER V

CONCLUSIONS AND RECOMMENDATIONS

1. Conclusions

The primary objective of this investigation was to compare digital meteorological radar data with infrared imagery from a meteorological satellite in geostationary orbit by determining the correlation between point values of infrared digital count and point values of radar reflectivity and vertically integrated liquid water content (VIL). Digital data from the 10 cm radar of the Department of Meteorology at TAMU were processed by a modified version of Sigeland's (1977) computer program and displayed as output maps of point values of zero-tilt reflectivity, low-, mid-, and upper-level PWSZ, and VIL. Digital GOES-East infrared satellite data from McIDAS image save types were processed to produce maps of point values of infrared digital count mapped to the same projection and grid interval used for the digital radar data. The maps of digital radar and digital satellite images formed the basis for comparisons between the two types of data.

This investigation has led to the following conclusions:

- 1) Large-scale features evident in the digital radar data are also apparent in the infrared imagery. The obscuring of low and middle level convection by cirrus overcast and the different

resolutions of the infrared GOES imagery (~ 8 km) and the digital radar (~ 1 km interpolated to a 2-km grid spacing) make areas of weak convection that are apparent in the radar data difficult or impossible to locate in the infrared imagery. This problem is probably more important to rainfall-estimation efforts than to efforts to locate and measure the intensity of severe convective activity. The fair correlation between mid-level PWSZ and the infrared data in such an instance may provide a way to partially eliminate this problem, particularly when the infrared data are enhanced by thresholding.

2) Although only one set of 2061 observations could be examined, thresholding the infrared data significantly improved the correlation between the radar and satellite data, especially the correlation with zero-tilt reflectivity and low-level PWSZ. Cheng and Roderhuis (1977) compared NOAA 2 infrared imagery with radar rainfall and determined that thresholding the satellite imagery did not improve the correlation. The results of this investigation suggest that thresholding the infrared GOES imagery should improve the correlation between the satellite data and radar rainfall. The difference in results may be due to procedural differences or to differences in the satellite sensors since the infrared sensor aboard the NOAA 2 satellite has a higher resolution than the GOES VISSR.

3) Correlations between the radar and satellite data, while

weak to fair, are in the main positive, and the correlation coefficients obtained suggest that the variability in one set of data is at least partially "explained by" the variability in the other set of data. As an example, a correlation coefficient of 0.5 suggests that 25 per cent of the variability in the dependent variable beyond its mean is explained by the independent variable. Correlation coefficients of the order of 0.4 to 0.6 were obtained in this study.

4) Thresholding the digital radar data may reduce correlation between the infrared images and zero-tilt reflectivity, low-level PVSZ, and mid-level PVSZ, thereby suggesting that such a process might be useful in situations where census of census low and mid-level convective. Caution must be exercised in such thresholding, however, since the correlation between the two types of data can be markedly diminished by this process if carried too far.

5) Thresholding the infrared imagery beyond a certain digital count diminishes the correlation between the infrared data and some of the radar data. The exact level at which this effect occurs was not determined in this study, but the results from the comparison of the first tilt-sequence with the infrared data suggest that thresholding above a digital count of 198 produces this effect with some of the digital radar variables and the infrared imagery. It is considered likely that a different enhancement than the MB curve used in this

investigation would produce better correlations of the data, since the MB curve is designed for use with hard copy imagery rather than digital data.

6) The resolution of the infrared data produced by the GOES VISSR is not sufficient to determine the strength of the correlation of infrared satellite data with digital radar data to the degree that might be desired. Given the results of Cheng and Rodenbush, who used a higher resolution sensor, the strength of the correlations obtained in this study is somewhat surprising and encouraging. The two investigations are not directly comparable, since Cheng and Rodenbush used radar rainfall derived from digital radar reflectivity in their analysis, but the results of this investigation suggest that a stronger relationship may exist between digital radar data and infrared satellite imagery than they discovered.

7) The best correlations between infrared images and radar data in the tenth tilt-sequence comparisons were obtained for the infrared image at the conclusion of the tilt-sequence, thus suggesting a significant time-dependence in comparisons of this type. Correlations between d and the digital radar data also indicate such a time-dependence.

2. Recommendations

The results of this investigation and its coincident review of the

Literature in this area suggest the following recommendations concerning the comparison of digital radar and digital satellite imagery:

- 1) The TAMU Weather Radar System possess a dual-wavelength capability that should be exploited in this type of investigation. Both 3-cm and 10-cm digital radar should be compared with infrared images at coincident times. Blended fields of radar data, obtained by sum, weighted sums, or functions of the 3-cm and 10-cm data, should be compared to the satellite imagery.
- 2) Smith and Reynolds (1978) have discussed digital composites of radar and satellite data for use in developing models of convective development, precipitation studies, and determining severe storm signatures. The relatively unique dual-wavelength capability of the TAMU digital weather radar should be exploited in studies of the type suggested by Smith and Reynolds by forming composites of the digital radar and digital satellite data. The blending of two different perspectives of the same storm system by combining the different types of data could shed new light on our understanding of convective processes and severe storm development.
- 3) The time-dependence in comparisons of digital satellite and digital radar data should be investigated to determine how great a difference can be tolerated before the correlations become too weak for valid analysis.

- 4) The remaining tile sequence from the 3 May 1978 study situation should be compared with corresponding CUSB infrared imagery to examine the development of the fields and to confirm the correlations between the digital radar and digital satellite data.
- 5) The effect of the blurring the infrared imagery in comparisons of radar and satellite data needs further investigation.
- 6) A control and comparison program developed at TAMD to digitize radar and digital and PIRE data simultaneously should be developed to permit rapid and efficient comparison of the data sets.
- 7) Comparisons of visible satellite imagery and digital radar data should be developed to determine the degree of correlation between the data types and fields in which they limit and complement. Brightness normalization techniques should be developed to permit such correlations to be made even at different solar zenith angles to facilitate comparisons between different areas and different images.
- 8) A capability to navigate digital satellite imagery using basic satellite orbital data should be developed at TAMD to minimize dependence on outside sources for such support and to facilitate the use of data from many different sources. Such a capability is required for the efficient use of data sources such as the experimenter's tapes from the AOIPS (Atmospheric and Oceanic Information Processing System) (McKown, 1977).

9) The time involved in this investigation suggests that more efficient utilization of resources can be obtained by using an interactive data handling system similar to the MCITS or the AOTRS. Development of such a system at TALM should be undertaken to enhance both the research and teaching capabilities within the College of Geosciences. The cost of developing such a system should be offset by maximizing the utility of such a system to handle different data fields from any different types of remote sensing data. To wider its applicability to include related scientific problems in other academic disciplines while retaining a basic orientation toward applications in meteorology and oceanography.

REFERENCES

Adler, R. F. and D. D. Penn, 1977: Satellite-derived thunderstorm intensity parameters. Preprints 10th Conf. on Severe Local Storms, Omaha, Amer. Meteor. Soc., 8-15.

Barr, A. J., J. H. Goodman, J. P. Stoll, and J. T. Holwitz, 1976: A User's Guide to SMS-76. SSEC Institute, Inc., Raleigh, 329 pp.

Barton, L. J., 1973: Radar Observation of Thunderstorms, University of Chicago, 324 pp.

Blocker, R. H., Jr., 1961: Satellite observations of cumulonimbus thunderstorms. Prepr. 5th Symp. Meteor. Conf., Kansas City, Amer. Meteor. Soc., 76-82.

_____, 1975: Correlation of cloud brightness and radiance with precipitation intensity. Tech. Rpt. NEPR-TR 6-75 (S.1), Contract N60314-71-0-2350, Stamford Research Institute, 134 pp.

_____, and S. M. Schubert, 1969: Analysis of maritime precipitation using radar data and satellite cloud photography. J. Appl. Meteor., 7, 122-131.

Boucher, R. J., 1967: Relationships between the size of satellite-observed cirrus fields and the severity of thunderstorm complexes. J. Appl. Meteor., 6, 564-572.

Cheng, N. and D. Rodenbush, 1977: An intercomparison of satellite images and radar rainfall rates. Preprints 10th Technical Conf. on Hurricanes and Tropical Meteorology, Miami Beach, Amer. Meteor. Soc., 224-226.

Corbell, R. P., C. J. Callahan, and W. J. Rotsch, 1976: The GOES/SMS User's Guide, National Environmental Satellite Service, Washington, 118 pp.

Fujita, T. T., 1977: Meteorological satellite observations and army operations. Tech. Rpt. ECOM 77-6, University of Chicago, 37 pp.

Gerrish, H. P., 1970: Satellite and radar analysis of mesoscale features in the tropics. Tech. Rpt. TCOM-0005-1, University of Miami, 45 pp.

—, 1975: Satellite and radar analysis of mesoscale weather systems. Tech. Rpt. TCOM-0014-1, University of Miami, 34 pp.

Greene, D. R., 1971: Numerical techniques for the analysis of digital radar data with applications to convoluted hydrometeors. Ph.D. dissertation, Texas A&M University, 124 pp.

—, 1964: An investigation of precipitation after rain and its application in a dual-doppler frequency morphology of subcategorical precipitation. M. S. thesis, Texas A&M University, 108 pp.

Griffith, G. G. and W. L. Wooley, 1973: On the variation with height of the top brightness of precipitating convective cells. *J. Appl. Meteor.*, 12, 1086-1089.

—, W. L. Wooley, P. G. Gruber, D. W. Martin, L. Stout, and D. N. Sildor, 1978: Rain estimation from geosynchronous satellite imagery - visible and infrared studies. *Mem. Meteor.*, Rev., 116, 1153-1171.

Gruber, A., 1973: Estimating rainfall in regions of active convection. *J. Appl. Meteor.*, 12, 110-118.

Haig, T. O., 1978, Private communication.

Haltiner, G. J., and F. L. Martin, 1957: Dynamical and Physical Meteorology, McGraw-Hill, New York, pp. 80-81.

McAnelly, R. L., 1979: Private communication.

McKowan, P. L., 1977: VISSR Data Processing Plan for Synchronous Meteorological and Geostationary Operational Environmental Satellites (SMS/GOES). NASA/Goddard Space Flight Center, Greenbelt, 220 pp.

Nagle, R. E., 1963: Comparisons of time integrated radar detected precipitation with satellite observed cloud patterns. Proc. 10th Radar Meteor. Conf., Washington, Amer. Meteor. Soc., 13-16.

_____, and S. M. Soroobay, 1962: Radar precipitation echo and satellite cloud observations of a maritime cyclone. *J. Appl. Meteor.*, **1**, 279-295.

Negri, A. J., D. W. Reynolds, and R. A. Maddux, 1970: Measurements of cumulonimbus clouds using quantitative satellite and radar data. *Proc. 7th Conf. on Applications of Environmental Meteorology and Symp. on Applications of Satellite Data to the Amer. Meteor. Soc.*, 119-124.

Neyland, M. A., 1978: An analysis of the data collection and use of a digital weather radar system with respect to significant severe weather features. *M. S. thesis, Texas A&M University*, 151 pp.

Phillips, J. P., 1975: Cloud structure from Defense Meteorological Satellite data. *M. S. thesis, Texas A&M University*, 147 pp.

Probert-Jones, J. R., 1963: The radar equation in meteorology. *Quart. J. Roy. Meteor. Soc.*, **88**, 486-505.

Reynolds, D. W., 1970: An inferential analysis of digital radar, rain gauge, and digital satellite data for a convective cloud system on the High Plains of Montana. *Proceedings of Symp. on Meteorological Observations and Applications*, *Joint Dept. of the Amer. Meteor. Soc.*, 310-317.

_____, and T. H. Vonder Haar, 1973: A comparison of radar-derived cloud height and reflected solar radiation measured from the geosynchronous satellite ATS-3. *J. Appl. Meteor.*, **12**, 1082-1090.

_____, T. H. Vonder Haar, and L. O. Grant, 1973: Meteorological satellites in support of weather modification. *Bull. Amer. Meteor. Soc.*, **54**, 269-281.

Siclend, T. E., 1977: Real-time computer techniques in the detection and analysis of severe storms from digital radar data. *Ph. D. dissertation, Texas A&M University*, 141 pp.

Sikdar, D. N., 1972: ATS-3 observed cloud brightness field related to a meso-synoptic scale rainfall pattern. *Tellus*, **24**, 400-413.

Smith, E. A., 1975: The McIDAS system. *IEEE Trans. Geosci. Electron.*, **GE-13**, 123-136.

_____, and D. W. Reynolds, 1978: The generation and display of digital radar-satellite composites using analytic mapping techniques and solid state video refresh technology. Preprints Conf. on Weather Forecasting and Analysis and Applications, Silver Spring, Amer. Meteor. Soc., 201-205.

Vonder Haar, T. H., 1969: Meteorological applications of reflected radiance measurements from ATS 1 and ATS 3. *J. Geophys. Res.*, **74**, 5404-5412.

_____, and R. S. Cram, 1970: A pilot study on the application of geosynchronous meteorological satellite data to very short range terminal forecasting. Tech. Rpt. AFGR-70-0493, Space Sciences and Engineering Center, University of Wisconsin, 116 pp.

Weiss, G. R., 1978: Cloud-location correction in the horizon of an SMS image. Satellite Applications Information Note 78-3, National Environmental Satellite Service, Washington, 5 pp.

Wexler, R., and R. J. Allison, 1972: Radar and infrared AV infrared measurements of the Oklahoma City tornado, 30 April 1970. Preprints 15th Radar Meteor. Conf., Chipping Barnet, Brit. Meteor. Soc., 77-82.

Young, J. T., 1978. Private communication.

APPENDIX A

THE MACMAP 3 AND MACIR COMPUTER PROGRAMS

This appendix contains copies of the MACMAP 3 and MACIR computer programs used to analyze the GOES images for this study.

```

C   READS MACIN
C   VERSION OF FACTIS WITH CHANNELS TO USE MAPPED DATA
C   PRECIPX READS DATA FOR A SELECTED IMAGE FROM RADAR SAVT TAPE 1 OR 2
C   AND PLAYS THE DATA INTO THE RADAR GRID USING EQUATIONS FROM MACIN3
C   FOR THE MAPPING FUNCTIONS
C   INPUT PARAMETERS
C   INPUT IMAGE NUMBER ON THE TAPE
C   ZLLX= LEFT HAND X COORD IN THE PORTION OF THE RADAR GRID TO BE
C   MAPPED X=0 AT ZERO, +VE EAST
C   ZLLY= LEFT HAND Y COORD TOP MAPPED GRID Y=0 AT TAPE, +VE NORTH
C   LMX= NUMBER OF GRID POINTS IN X DIRECTION (MAXIMUM 140)
C   LMN= NUMBER OF GRID POINTS IN Y-DIRECTION (MAX 240)
C   LCMX= LEFT COORD VERT IN COORDS OF CURRENT RADAR IMAGE
C   IFCNT= ELEMENT COUNT UPON THE COORDS OF CURRENT RADAR IMAGE
C   NLLX= NUMBER OF LINES FOR EACH
C   NLLY= NUMBER OF PICTURES PER IMAGE
C   NTLLX= NUMBER OF LINES PER IMAGE
C   NTLLY= NUMBER OF PICTURES PER IMAGE
C   NTLLY= (1+X*Y*Z) * CNTS = CONSTANT TIMES NUMBER MAPPING FUNCTIONS
C   NTLLY= NUMBER OF PICTURES TO BE READ FROM TAPE TO THE FIRST TAPE 3 SAVT
C   LMX=1, LMN=1, ID(2,3)
C   REAL X1,X2
C   INTEGER*2 KSLVTP(0,100),TSCUD(240,240)
C   COMMON /TSCUD/SL,TC1,TC2,TC3,TC4,TC5,TC6,TC7,TC8,TC9,TC10,TC11,TC12,TC13,TC14,TC15,TC16,TC17,TC18,TC19,TC20,TC21,TC22,TC23,TC24,TC25,TC26,TC27,TC28,TC29,TC30,TC31,TC32,TC33,TC34,TC35,TC36,TC37,TC38,TC39,TC40,TC41,TC42,TC43,TC44,TC45,TC46,TC47,TC48,TC49,TC50,TC51,TC52,TC53,TC54,TC55,TC56,TC57,TC58,TC59,TC60,TC61,TC62,TC63,TC64,TC65,TC66,TC67,TC68,TC69,TC70,TC71,TC72,TC73,TC74,TC75,TC76,TC77,TC78,TC79,TC80,TC81,TC82,TC83,TC84,TC85,TC86,TC87,TC88,TC89,TC90,TC91,TC92,TC93,TC94,TC95,TC96,TC97,TC98,TC99,TC100,TC110,TC120,TC130,TC140,TC150,TC160,TC170,TC180,TC190,TC200,TC210,TC220,TC230,TC240,TC250,TC260,TC270,TC280,TC290,TC300,TC310,TC320,TC330,TC340,TC350,TC360,TC370,TC380,TC390,TC400,TC410,TC420,TC430,TC440,TC450,TC460,TC470,TC480,TC490,TC500,TC510,TC520,TC530,TC540,TC550,TC560,TC570,TC580,TC590,TC600,TC610,TC620,TC630,TC640,TC650,TC660,TC670,TC680,TC690,TC700,TC710,TC720,TC730,TC740,TC750,TC760,TC770,TC780,TC790,TC800,TC810,TC820,TC830,TC840,TC850,TC860,TC870,TC880,TC890,TC900,TC910,TC920,TC930,TC940,TC950,TC960,TC970,TC980,TC990,TC1000,TC1100,TC1200,TC1300,TC1400,TC1500,TC1600,TC1700,TC1800,TC1900,TC2000,TC2100,TC2200,TC2300,TC2400,TC2500,TC2600,TC2700,TC2800,TC2900,TC3000,TC3100,TC3200,TC3300,TC3400,TC3500,TC3600,TC3700,TC3800,TC3900,TC4000,TC4100,TC4200,TC4300,TC4400,TC4500,TC4600,TC4700,TC4800,TC4900,TC5000,TC5100,TC5200,TC5300,TC5400,TC5500,TC5600,TC5700,TC5800,TC5900,TC6000,TC6100,TC6200,TC6300,TC6400,TC6500,TC6600,TC6700,TC6800,TC6900,TC7000,TC7100,TC7200,TC7300,TC7400,TC7500,TC7600,TC7700,TC7800,TC7900,TC8000,TC8100,TC8200,TC8300,TC8400,TC8500,TC8600,TC8700,TC8800,TC8900,TC9000,TC9100,TC9200,TC9300,TC9400,TC9500,TC9600,TC9700,TC9800,TC9900,TC10000,TC11000,TC12000,TC13000,TC14000,TC15000,TC16000,TC17000,TC18000,TC19000,TC20000,TC21000,TC22000,TC23000,TC24000,TC25000,TC26000,TC27000,TC28000,TC29000,TC30000,TC31000,TC32000,TC33000,TC34000,TC35000,TC36000,TC37000,TC38000,TC39000,TC40000,TC41000,TC42000,TC43000,TC44000,TC45000,TC46000,TC47000,TC48000,TC49000,TC50000,TC51000,TC52000,TC53000,TC54000,TC55000,TC56000,TC57000,TC58000,TC59000,TC60000,TC61000,TC62000,TC63000,TC64000,TC65000,TC66000,TC67000,TC68000,TC69000,TC70000,TC71000,TC72000,TC73000,TC74000,TC75000,TC76000,TC77000,TC78000,TC79000,TC80000,TC81000,TC82000,TC83000,TC84000,TC85000,TC86000,TC87000,TC88000,TC89000,TC90000,TC91000,TC92000,TC93000,TC94000,TC95000,TC96000,TC97000,TC98000,TC99000,TC100000,TC110000,TC120000,TC130000,TC140000,TC150000,TC160000,TC170000,TC180000,TC190000,TC200000,TC210000,TC220000,TC230000,TC240000,TC250000,TC260000,TC270000,TC280000,TC290000,TC300000,TC310000,TC320000,TC330000,TC340000,TC350000,TC360000,TC370000,TC380000,TC390000,TC400000,TC410000,TC420000,TC430000,TC440000,TC450000,TC460000,TC470000,TC480000,TC490000,TC500000,TC510000,TC520000,TC530000,TC540000,TC550000,TC560000,TC570000,TC580000,TC590000,TC600000,TC610000,TC620000,TC630000,TC640000,TC650000,TC660000,TC670000,TC680000,TC690000,TC700000,TC710000,TC720000,TC730000,TC740000,TC750000,TC760000,TC770000,TC780000,TC790000,TC800000,TC810000,TC820000,TC830000,TC840000,TC850000,TC860000,TC870000,TC880000,TC890000,TC900000,TC910000,TC920000,TC930000,TC940000,TC950000,TC960000,TC970000,TC980000,TC990000,TC1000000,TC1100000,TC1200000,TC1300000,TC1400000,TC1500000,TC1600000,TC1700000,TC1800000,TC1900000,TC2000000,TC2100000,TC2200000,TC2300000,TC2400000,TC2500000,TC2600000,TC2700000,TC2800000,TC2900000,TC3000000,TC3100000,TC3200000,TC3300000,TC3400000,TC3500000,TC3600000,TC3700000,TC3800000,TC3900000,TC4000000,TC4100000,TC4200000,TC4300000,TC4400000,TC4500000,TC4600000,TC4700000,TC4800000,TC4900000,TC5000000,TC5100000,TC5200000,TC5300000,TC5400000,TC5500000,TC5600000,TC5700000,TC5800000,TC5900000,TC6000000,TC6100000,TC6200000,TC6300000,TC6400000,TC6500000,TC6600000,TC6700000,TC6800000,TC6900000,TC7000000,TC7100000,TC7200000,TC7300000,TC7400000,TC7500000,TC7600000,TC7700000,TC7800000,TC7900000,TC8000000,TC8100000,TC8200000,TC8300000,TC8400000,TC8500000,TC8600000,TC8700000,TC8800000,TC8900000,TC9000000,TC9100000,TC9200000,TC9300000,TC9400000,TC9500000,TC9600000,TC9700000,TC9800000,TC9900000,TC10000000,TC11000000,TC12000000,TC13000000,TC14000000,TC15000000,TC16000000,TC17000000,TC18000000,TC19000000,TC20000000,TC21000000,TC22000000,TC23000000,TC24000000,TC25000000,TC26000000,TC27000000,TC28000000,TC29000000,TC30000000,TC31000000,TC32000000,TC33000000,TC34000000,TC35000000,TC36000000,TC37000000,TC38000000,TC39000000,TC40000000,TC41000000,TC42000000,TC43000000,TC44000000,TC45000000,TC46000000,TC47000000,TC48000000,TC49000000,TC50000000,TC51000000,TC52000000,TC53000000,TC54000000,TC55000000,TC56000000,TC57000000,TC58000000,TC59000000,TC60000000,TC61000000,TC62000000,TC63000000,TC64000000,TC65000000,TC66000000,TC67000000,TC68000000,TC69000000,TC70000000,TC71000000,TC72000000,TC73000000,TC74000000,TC75000000,TC76000000,TC77000000,TC78000000,TC79000000,TC80000000,TC81000000,TC82000000,TC83000000,TC84000000,TC85000000,TC86000000,TC87000000,TC88000000,TC89000000,TC90000000,TC91000000,TC92000000,TC93000000,TC94000000,TC95000000,TC96000000,TC97000000,TC98000000,TC99000000,TC100000000,TC110000000,TC120000000,TC130000000,TC140000000,TC150000000,TC160000000,TC170000000,TC180000000,TC190000000,TC200000000,TC210000000,TC220000000,TC230000000,TC240000000,TC250000000,TC260000000,TC270000000,TC280000000,TC290000000,TC300000000,TC310000000,TC320000000,TC330000000,TC340000000,TC350000000,TC360000000,TC370000000,TC380000000,TC390000000,TC400000000,TC410000000,TC420000000,TC430000000,TC440000000,TC450000000,TC460000000,TC470000000,TC480000000,TC490000000,TC500000000,TC510000000,TC520000000,TC530000000,TC540000000,TC550000000,TC560000000,TC570000000,TC580000000,TC590000000,TC600000000,TC610000000,TC620000000,TC630000000,TC640000000,TC650000000,TC660000000,TC670000000,TC680000000,TC690000000,TC700000000,TC710000000,TC720000000,TC730000000,TC740000000,TC750000000,TC760000000,TC770000000,TC780000000,TC790000000,TC800000000,TC810000000,TC820000000,TC830000000,TC840000000,TC850000000,TC860000000,TC870000000,TC880000000,TC890000000,TC900000000,TC910000000,TC920000000,TC930000000,TC940000000,TC950000000,TC960000000,TC970000000,TC980000000,TC990000000,TC1000000000,TC1100000000,TC1200000000,TC1300000000,TC1400000000,TC1500000000,TC1600000000,TC1700000000,TC1800000000,TC1900000000,TC2000000000,TC2100000000,TC2200000000,TC2300000000,TC2400000000,TC2500000000,TC2600000000,TC2700000000,TC2800000000,TC2900000000,TC3000000000,TC3100000000,TC3200000000,TC3300000000,TC3400000000,TC3500000000,TC3600000000,TC3700000000,TC3800000000,TC3900000000,TC4000000000,TC4100000000,TC4200000000,TC4300000000,TC4400000000,TC4500000000,TC4600000000,TC4700000000,TC4800000000,TC4900000000,TC5000000000,TC5100000000,TC5200000000,TC5300000000,TC5400000000,TC5500000000,TC5600000000,TC5700000000,TC5800000000,TC5900000000,TC6000000000,TC6100000000,TC6200000000,TC6300000000,TC6400000000,TC6500000000,TC6600000000,TC6700000000,TC6800000000,TC6900000000,TC7000000000,TC7100000000,TC7200000000,TC7300000000,TC7400000000,TC7500000000,TC7600000000,TC7700000000,TC7800000000,TC7900000000,TC8000000000,TC8100000000,TC8200000000,TC8300000000,TC8400000000,TC8500000000,TC8600000000,TC8700000000,TC8800000000,TC8900000000,TC9000000000,TC9100000000,TC9200000000,TC9300000000,TC9400000000,TC9500000000,TC9600000000,TC9700000000,TC9800000000,TC9900000000,TC10000000000,TC11000000000,TC12000000000,TC13000000000,TC14000000000,TC15000000000,TC16000000000,TC17000000000,TC18000000000,TC19000000000,TC20000000000,TC21000000000,TC22000000000,TC23000000000,TC24000000000,TC25000000000,TC26000000000,TC27000000000,TC28000000000,TC29000000000,TC30000000000,TC31000000000,TC32000000000,TC33000000000,TC34000000000,TC35000000000,TC36000000000,TC37000000000,TC38000000000,TC39000000000,TC40000000000,TC41000000000,TC42000000000,TC43000000000,TC44000000000,TC45000000000,TC46000000000,TC47000000000,TC48000000000,TC49000000000,TC50000000000,TC51000000000,TC52000000000,TC53000000000,TC54000000000,TC55000000000,TC56000000000,TC57000000000,TC58000000000,TC59000000000,TC60000000000,TC61000000000,TC62000000000,TC63000000000,TC64000000000,TC65000000000,TC66000000000,TC67000000000,TC68000000000,TC69000000000,TC70000000000,TC71000000000,TC72000000000,TC73000000000,TC74000000000,TC75000000000,TC76000000000,TC77000000000,TC78000000000,TC79000000000,TC80000000000,TC81000000000,TC82000000000,TC83000000000,TC84000000000,TC85000000000,TC86000000000,TC87000000000,TC88000000000,TC89000000000,TC90000000000,TC91000000000,TC92000000000,TC93000000000,TC94000000000,TC95000000000,TC96000000000,TC97000000000,TC98000000000,TC99000000000,TC100000000000,TC110000000000,TC120000000000,TC130000000000,TC140000000000,TC150000000000,TC160000000000,TC170000000000,TC180000000000,TC190000000000,TC200000000000,TC210000000000,TC220000000000,TC230000000000,TC240000000000,TC250000000000,TC260000000000,TC270000000000,TC280000000000,TC290000000000,TC300000000000,TC310000000000,TC320000000000,TC330000000000,TC340000000000,TC350000000000,TC360000000000,TC370000000000,TC380000000000,TC390000000000,TC400000000000,TC410000000000,TC420000000000,TC430000000000,TC440000000000,TC450000000000,TC460000000000,TC470000000000,TC480000000000,TC490000000000,TC500000000000,TC510000000000,TC520000000000,TC530000000000,TC540000000000,TC550000000000,TC560000000000,TC570000000000,TC580000000000,TC590000000000,TC600000000000,TC610000000000,TC620000000000,TC630000000000,TC640000000000,TC650000000000,TC660000000000,TC670000000000,TC680000000000,TC690000000000,TC700000000000,TC710000000000,TC720000000000,TC730000000000,TC740000000000,TC750000000000,TC760000000000,TC770000000000,TC780000000000,TC790000000000,TC800000000000,TC810000000000,TC820000000000,TC830000000000,TC840000000000,TC850000000000,TC860000000000,TC870000000000,TC880000000000,TC890000000000,TC900000000000,TC910000000000,TC920000000000,TC930000000000,TC940000000000,TC950000000000,TC960000000000,TC970000000000,TC980000000000,TC990000000000,TC1000000000000,TC1100000000000,TC1200000000000,TC1300000000000,TC1400000000000,TC1500000000000,TC1600000000000,TC1700000000000,TC1800000000000,TC1900000000000,TC2000000000000,TC2100000000000,TC2200000000000,TC2300000000000,TC2400000000000,TC2500000000000,TC2600000000000,TC2700000000000,TC2800000000000,TC2900000000000,TC3000000000000,TC3100000000000,TC3200000000000,TC3300000000000,TC3400000000000,TC3500000000000,TC3600000000000,TC3700000000000,TC3800000000000,TC3900000000000,TC4000000000000,TC4100000000000,TC4200000000000,TC4300000000000,TC4400000000000,TC4500000000000,TC4600000000000,TC4700000000000,TC4800000000000,TC4900000000000,TC5000000000000,TC5100000000000,TC5200000000000,TC5300000000000,TC5400000000000,TC5500000000000,TC5600000000000,TC5700000000000,TC5800000000000,TC5900000000000,TC6000000000000,TC6100000000000,TC6200000000000,TC6300000000000,TC6400000000000,TC6500000000000,TC6600000000000,TC6700000000000,TC6800000000000,TC6900000000000,TC7000000000000,TC7100000000000,TC7200000000000,TC7300000000000,TC7400000000000,TC7500000000000,TC7600000000000,TC7700000000000,TC7800000000000,TC7900000000000,TC8000000000000,TC8100000000000,TC8200000000000,TC8300000000000,TC8400000000000,TC8500000000000,TC8600000000000,TC8700000000000,TC8800000000000,TC8900000000000,TC9000000000000,TC9100000000000,TC9200000000000,TC9300000000000,TC9400000000000,TC9500000000000,TC9600000000000,TC9700000000000,TC9800000000000,TC9900000000000,TC10000000000000,TC11000000000000,TC12000000000000,TC13000000000000,TC14000000000000,TC15000000000000,TC16000000000000,TC17000000000000,TC18000000000000,TC19000000000000,TC20000000000000,TC21000000000000,TC22000000000000,TC23000000000000,TC24000000000000,TC25000000000000,TC26000000000000,TC27000000000000,TC28000000000000,TC29000000000000,TC30000000000000,TC31000000000000,TC32000000000000,TC33000000000000,TC34000000000000,TC35000000000000,TC36000000000000,TC37000000000000,TC38000000000000,TC39000000000000,TC40000000000000,TC41000000000000,TC42000000000000,TC43000000000000,TC44000000000000,TC45000000000000,TC46000000000000,TC47000000000000,TC48000000000000,TC49000000000000,TC50000000000000,TC51000000000000,TC52000000000000,TC53000000000000,TC54000000000000,TC55000000000000,TC56000000000000,TC57000000000000,TC58000000000000,TC59000000000000,TC60000000000000,TC61000000000000,TC62000000000000,TC63000000000000,TC64000000000000,TC65000000000000,TC66000000000000,TC67000000000000,TC68000000000000,TC69000000000000,TC70000000000000,TC71000000000000,TC72000000000000,TC73000000000000,TC74000000000000,TC75000000000000,TC76000000000000,TC77000000000000,TC78000000000000,TC79000000000000,TC80000000000000,TC81000000000000,TC82000000000000,TC83000000000000,TC84000000000000,TC85000000000000,TC86000000000000,TC87000000000000,TC88000000000000,TC89000000000000,TC90000000000000,TC91000000000000,TC92000000000000,TC93000000000000,TC94000000000000,TC95000000000000,TC96000000000000,TC97000000000000,TC98000000000000,TC99000000000000,TC100000000000000,TC110000000000000,TC120000000000000,TC130000000000000,TC140000000000000,TC150000000000000,TC160000000000000,TC170000000000000,TC180000000000000,TC190000000000000,TC200000000000000,TC210000000000000,TC2200000000
```


12 CO 12 6
 9 FNC(12,13)
 12 FNC(12,13,14,15)(31) GO TO 13
 13 GO TO 14
 14 SC(12,13,14)
 15 CO 15 7
 200 7 CO 15 8
 201 8 CO 15 9
 202 9 CO 15 10
 203 10 CO 15 11
 204 11 CO 15 12
 205 12 CO 15 13
 206 13 CO 15 14
 207 14 CO 15 15
 208 15 CO 15 16
 209 16 CO 15 17
 210 17 CO 15 18
 211 18 CO 15 19
 212 19 CO 15 20
 213 20 CO 15 21
 214 21 CO 15 22
 215 22 CO 15 23
 216 23 CO 15 24
 217 24 CO 15 25
 218 25 CO 15 26
 219 26 CO 15 27
 220 27 CO 15 28
 221 28 CO 15 29
 222 29 CO 15 30
 223 30 CO 15 31
 224 31 CO 15 32
 225 32 CO 15 33
 226 33 CO 15 34
 227 34 CO 15 35
 228 35 CO 15 36
 229 36 CO 15 37
 230 37 CO 15 38
 231 38 CO 15 39
 232 39 CO 15 40
 233 40 CO 15 41
 234 41 CO 15 42
 235 42 CO 15 43
 236 43 CO 15 44
 237 44 CO 15 45
 238 45 CO 15 46
 239 46 CO 15 47
 240 47 CO 15 48
 241 48 CO 15 49
 242 49 CO 15 50
 243 50 CO 15 51
 244 51 CO 15 52
 245 52 CO 15 53
 246 53 CO 15 54
 247 54 CO 15 55
 248 55 CO 15 56
 249 56 CO 15 57
 250 57 CO 15 58
 251 58 CO 15 59
 252 59 CO 15 60
 253 60 CO 15 61
 254 61 CO 15 62
 255 62 CO 15 63
 256 63 CO 15 64
 257 64 CO 15 65
 258 65 CO 15 66
 259 66 CO 15 67
 260 67 CO 15 68
 261 68 CO 15 69
 262 69 CO 15 70
 263 70 CO 15 71
 264 71 CO 15 72
 265 72 CO 15 73
 266 73 CO 15 74
 267 74 CO 15 75
 268 75 CO 15 76
 269 76 CO 15 77
 270 77 CO 15 78
 271 78 CO 15 79
 272 79 CO 15 80
 273 80 CO 15 81
 274 81 CO 15 82
 275 82 CO 15 83
 276 83 CO 15 84
 277 84 CO 15 85
 278 85 CO 15 86
 279 86 CO 15 87
 280 87 CO 15 88
 281 88 CO 15 89
 282 89 CO 15 90
 283 90 CO 15 91
 284 91 CO 15 92
 285 92 CO 15 93
 286 93 CO 15 94
 287 94 CO 15 95
 288 95 CO 15 96
 289 96 CO 15 97
 290 97 CO 15 98
 291 98 CO 15 99
 292 99 CO 15 100
 293 100 CO 15 101
 294 101 CO 15 102
 295 102 CO 15 103
 296 103 CO 15 104
 297 104 CO 15 105
 298 105 CO 15 106
 299 106 CO 15 107
 300 107 CO 15 108
 301 108 CO 15 109
 302 109 CO 15 110
 303 110 CO 15 111
 304 111 CO 15 112
 305 112 CO 15 113
 306 113 CO 15 114
 307 114 CO 15 115
 308 115 CO 15 116
 309 116 CO 15 117
 310 117 CO 15 118
 311 118 CO 15 119
 312 119 CO 15 120
 313 120 CO 15 121
 314 121 CO 15 122
 315 122 CO 15 123
 316 123 CO 15 124
 317 124 CO 15 125
 318 125 CO 15 126
 319 126 CO 15 127
 320 127 CO 15 128
 321 128 CO 15 129
 322 129 CO 15 130
 323 130 CO 15 131
 324 131 CO 15 132
 325 132 CO 15 133
 326 133 CO 15 134
 327 134 CO 15 135
 328 135 CO 15 136
 329 136 CO 15 137
 330 137 CO 15 138
 331 138 CO 15 139
 332 139 CO 15 140
 333 140 CO 15 141
 334 141 CO 15 142
 335 142 CO 15 143
 336 143 CO 15 144
 337 144 CO 15 145
 338 145 CO 15 146
 339 146 CO 15 147
 340 147 CO 15 148
 341 148 CO 15 149
 342 149 CO 15 150
 343 150 CO 15 151
 344 151 CO 15 152
 345 152 CO 15 153
 346 153 CO 15 154
 347 154 CO 15 155
 348 155 CO 15 156
 349 156 CO 15 157
 350 157 CO 15 158
 351 158 CO 15 159
 352 159 CO 15 160
 353 160 CO 15 161
 354 161 CO 15 162
 355 162 CO 15 163
 356 163 CO 15 164
 357 164 CO 15 165
 358 165 CO 15 166
 359 166 CO 15 167
 360 167 CO 15 168
 361 168 CO 15 169
 362 169 CO 15 170
 363 170 CO 15 171
 364 171 CO 15 172
 365 172 CO 15 173
 366 173 CO 15 174
 367 174 CO 15 175
 368 175 CO 15 176
 369 176 CO 15 177
 370 177 CO 15 178
 371 178 CO 15 179
 372 179 CO 15 180
 373 180 CO 15 181
 374 181 CO 15 182
 375 182 CO 15 183
 376 183 CO 15 184
 377 184 CO 15 185
 378 185 CO 15 186
 379 186 CO 15 187
 380 187 CO 15 188
 381 188 CO 15 189
 382 189 CO 15 190
 383 190 CO 15 191
 384 191 CO 15 192
 385 192 CO 15 193
 386 193 CO 15 194
 387 194 CO 15 195
 388 195 CO 15 196
 389 196 CO 15 197
 390 197 CO 15 198
 391 198 CO 15 199
 392 199 CO 15 200
 393 200 CO 15 201
 394 201 CO 15 202
 395 202 CO 15 203
 396 203 CO 15 204
 397 204 CO 15 205
 398 205 CO 15 206
 399 206 CO 15 207
 400 207 CO 15 208
 401 208 CO 15 209
 402 209 CO 15 210
 403 210 CO 15 211
 404 211 CO 15 212
 405 212 CO 15 213
 406 213 CO 15 214
 407 214 CO 15 215
 408 215 CO 15 216
 409 216 CO 15 217
 410 217 CO 15 218
 411 218 CO 15 219
 412 219 CO 15 220
 413 220 CO 15 221
 414 221 CO 15 222
 415 222 CO 15 223
 416 223 CO 15 224
 417 224 CO 15 225
 418 225 CO 15 226
 419 226 CO 15 227
 420 227 CO 15 228
 421 228 CO 15 229
 422 229 CO 15 230
 423 230 CO 15 231
 424 231 CO 15 232
 425 232 CO 15 233
 426 233 CO 15 234
 427 234 CO 15 235
 428 235 CO 15 236
 429 236 CO 15 237
 430 237 CO 15 238
 431 238 CO 15 239
 432 239 CO 15 240
 433 240 CO 15 241
 434 241 CO 15 242
 435 242 CO 15 243
 436 243 CO 15 244
 437 244 CO 15 245
 438 245 CO 15 246
 439 246 CO 15 247
 440 247 CO 15 248
 441 248 CO 15 249
 442 249 CO 15 250
 443 250 CO 15 251
 444 251 CO 15 252
 445 252 CO 15 253
 446 253 CO 15 254
 447 254 CO 15 255
 448 255 CO 15 256
 449 256 CO 15 257
 450 257 CO 15 258
 451 258 CO 15 259
 452 259 CO 15 260
 453 260 CO 15 261
 454 261 CO 15 262
 455 262 CO 15 263
 456 263 CO 15 264
 457 264 CO 15 265
 458 265 CO 15 266
 459 266 CO 15 267
 460 267 CO 15 268
 461 268 CO 15 269
 462 269 CO 15 270
 463 270 CO 15 271
 464 271 CO 15 272
 465 272 CO 15 273
 466 273 CO 15 274
 467 274 CO 15 275
 468 275 CO 15 276
 469 276 CO 15 277
 470 277 CO 15 278
 471 278 CO 15 279
 472 279 CO 15 280
 473 280 CO 15 281
 474 281 CO 15 282
 475 282 CO 15 283
 476 283 CO 15 284
 477 284 CO 15 285
 478 285 CO 15 286
 479 286 CO 15 287
 480 287 CO 15 288
 481 288 CO 15 289
 482 289 CO 15 290
 483 290 CO 15 291
 484 291 CO 15 292
 485 292 CO 15 293
 486 293 CO 15 294
 487 294 CO 15 295
 488 295 CO 15 296
 489 296 CO 15 297
 490 297 CO 15 298
 491 298 CO 15 299
 492 299 CO 15 300
 493 300 CO 15 301
 494 301 CO 15 302
 495 302 CO 15 303
 496 303 CO 15 304
 497 304 CO 15 305
 498 305 CO 15 306
 499 306 CO 15 307
 500 307 CO 15 308
 501 308 CO 15 309
 502 309 CO 15 310
 503 310 CO 15 311
 504 311 CO 15 312
 505 312 CO 15 313
 506 313 CO 15 314
 507 314 CO 15 315
 508 315 CO 15 316
 509 316 CO 15 317
 510 317 CO 15 318
 511 318 CO 15 319
 512 319 CO 15 320
 513 320 CO 15 321
 514 321 CO 15 322
 515 322 CO 15 323
 516 323 CO 15 324
 517 324 CO 15 325
 518 325 CO 15 326
 519 326 CO 15 327
 520 327 CO 15 328
 521 328 CO 15 329
 522 329 CO 15 330
 523 330 CO 15 331
 524 331 CO 15 332
 525 332 CO 15 333
 526 333 CO 15 334
 527 334 CO 15 335
 528 335 CO 15 336
 529 336 CO 15 337
 530 337 CO 15 338
 531 338 CO 15 339
 532 339 CO 15 340
 533 340 CO 15 341
 534 341 CO 15 342
 535 342 CO 15 343
 536 343 CO 15 344
 537 344 CO 15 345
 538 345 CO 15 346
 539 346 CO 15 347
 540 347 CO 15 348
 541 348 CO 15 349
 542 349 CO 15 350
 543 350 CO 15 351
 544 351 CO 15 352
 545 352 CO 15 353
 546 353 CO 15 354
 547 354 CO 15 355
 548 355 CO 15 356
 549 356 CO 15 357
 550 357 CO 15 358
 551 358 CO 15 359
 552 359 CO 15 360
 553 360 CO 15 361
 554 361 CO 15 362
 555 362 CO 15 363
 556 363 CO 15 364
 557 364 CO 15 365
 558 365 CO 15 366
 559 366 CO 15 367
 560 367 CO 15 368
 561 368 CO 15 369
 562 369 CO 15 370
 563 370 CO 15 371
 564 371 CO 15 372
 565 372 CO 15 373
 566 373 CO 15 374
 567 374 CO 15 375
 568 375 CO 15 376
 569 376 CO 15 377
 570 377 CO 15 378
 571 378 CO 15 379
 572 379 CO 15 380
 573 380 CO 15 381
 574 381 CO 15 382
 575 382 CO 15 383
 576 383 CO 15 384
 577 384 CO 15 385
 578 385 CO 15 386
 579 386 CO 15 387
 580 387 CO 15 388
 581 388 CO 15 389
 582 389 CO 15 390
 583 390 CO 15 391
 584 391 CO 15 392
 585 392 CO 15 393
 586 393 CO 15 394
 587 394 CO 15 395
 588 395 CO 15 396
 589 396 CO 15 397
 590 397 CO 15 398
 591 398 CO 15 399
 592 399 CO 15 400
 593 400 CO 15 401
 594 401 CO 15 402
 595 402 CO 15 403
 596 403 CO 15 404
 597 404 CO 15 405
 598 405 CO 15 406
 599 406 CO 15 407
 600 407 CO 15 408
 601 408 CO 15 409
 602 409 CO 15 410
 603 410 CO 15 411
 604 411 CO 15 412
 605 412 CO 15 413
 606 413 CO 15 414
 607 414 CO 15 415
 608 415 CO 15 416
 609 416 CO 15 417
 610 417 CO 15 418
 611 418 CO 15 419
 612 419 CO 15 420
 613 420 CO 15 421
 614 421 CO 15 422
 615 422 CO 15 423
 616 423 CO 15 424
 617 424 CO 15 425
 618 425 CO 15 426
 619 426 CO 15 427
 620 427 CO 15 428
 621 428 CO 15 429
 622 429 CO 15 430
 623 430 CO 15 431
 624 431 CO 15 432
 625 432 CO 15 433
 626 433 CO 15 434
 627 434 CO 15 435
 628 435 CO 15 436
 629 436 CO 15 437
 630 437 CO 15 438
 631 438 CO 15 439
 632 439 CO 15 440
 633 440 CO 15 441
 634 441 CO 15 442
 635 442 CO 15 443
 636 443 CO 15 444
 637 444 CO 15 445
 638 445 CO 15 446
 639 446 CO 15 447
 640 447 CO 15 448
 641 448 CO 15 449
 642 449 CO 15 450
 643 450 CO 15 451
 644 451 CO 15 452
 645 452 CO 15 453
 646 453 CO 15 454
 647 454 CO 15 455
 648 455 CO 15 456
 649 456 CO 15 457
 650 457 CO 15 458
 651 458 CO 15 459
 652 459 CO 15 460
 653 460 CO 15 461
 654 461 CO 15 462
 655 462 CO 15 463
 656 463 CO 15 464
 657 464 CO 15 465
 658 465 CO 15 466
 659 466 CO 15 467
 660 467 CO 15 468
 661 468 CO 15 469
 662 469 CO 15 470
 663 470 CO 15 471
 664 471 CO 15 472
 665 472 CO 15 473
 666 473 CO 15 474
 667 474 CO 15 475
 668 475 CO 15 476
 669 476 CO 15 477
 670 477 CO 15 478
 671 478 CO 15 479
 672 479 CO 15 480
 673 480 CO 15 481
 674 481 CO 15 482
 675 482 CO 15 483
 676 483 CO 15 484
 677 484 CO 15 485
 678 485 CO 15 486
 679 486 CO 15 487
 680 487 CO 15 488
 681 488 CO 15 489
 682 489 CO 15 490
 683 490 CO 15 491
 684 491 CO 15 492
 685 492 CO 15 493
 686 493 CO 15 494
 687 494 CO 15 495
 688 495 CO 15 496
 689 496 CO 15 497
 690 497 CO 15 498
 691 498 CO 15 499
 692 499 CO 15 500
 693 500 CO 15 501
 694 501 CO 15 502
 695 502 CO 15 503
 696 503 CO 15 504
 697 504 CO 15 505
 698 505 CO 15 506
 699 506 CO 15 507
 700 507 CO 15 508
 701 508 CO 15 509
 702 509 CO 15 510
 703 510 CO 15 511
 704 511 CO 15 512
 705 512 CO 15 513
 706 513 CO 15 514
 707 514 CO 15 515
 708 515 CO 15 516
 709 516 CO 15 517
 710 517 CO 15 518
 711 518 CO 15 519
 712 519 CO 15 520
 713 520 CO 15 521
 714 521 CO 15 522
 715 522 CO 15 523
 716 523 CO 15 524
 717 524 CO 15 525
 718 525 CO 15 526
 719 526 CO 15 527
 720 527 CO 15 528
 721 528 CO 15 529
 722 529 CO 15 530
 723 530 CO 15 531
 724 531 CO 15 532
 725 532 CO 15 533
 726 533 CO 15 534
 727 534 CO 15 535
 728 535 CO 15 536
 729 536 CO 15 537
 730 537 CO 15 538
 731 538 CO 15 539
 732 539 CO 15 540
 733 540 CO 15 541
 734 541 CO 15 542
 735 542 CO 15 543
 736 543 CO 15 544
 737 544 CO 15 545
 738 545 CO 15 546
 739 546 CO 15 547
 740 547 CO 15 548
 741 548 CO 15 549
 742 549 CO 15 550
 743 550 CO 15 551
 744 551 CO 15 552
 745 552 CO 15 553
 746 553 CO 15 554
 747 554 CO 15 555
 748 555 CO 15 556
 749 556 CO 15 557
 750 557 CO 15 558
 751 558 CO 15 559
 752 559 CO 15 560
 753 560 CO 15 561
 754 561 CO 15 562
 755 562 CO 15 563
 756 563 CO 15 564
 757 564 CO 15 565
 758 565 CO 15 566
 759 566 CO 15 567
 760 567 CO 15 568
 761 568 CO 15 569
 762 569 CO 15 570
 763 570 CO 15 571
 764 571 CO 15 572
 765 572 CO 15 573
 766 573 CO 15 574
 767 574 CO 15 575
 768 575 CO 15 576
 769 576 CO 15 577
 770 577 CO 15 578
 771 578 CO 15 579
 772 579 CO 15 580
 773 580 CO 15 581
 774 581 CO 15 582
 775 582 CO 15 583
 776 583 CO 15 584
 777 584 CO 15 585
 778 585 CO 15 586
 779 586 CO 15 587
 780 587 CO 15 588
 781 588 CO 15 589
 782 589 CO 15 590
 783 590 CO 15 591
 784 591 CO 15 592
 785 592 CO 15 593
 786 593 CO 15 594
 787 594 CO 15 595
 788 595 CO 15 596
 789 596 CO 15 597
 790 597 CO 15 598
 791 598 CO 15 599
 792 599 CO 15 600
 793 600 CO 15 601
 794 601 CO 15 602
 795 602 CO 15 603
 796 603 CO 15 604
 797 604 CO


```

2      ICODE(I,J)=FCRWT(L,IPTRK,KEY(I,J))
3      CONTINUE
4      CONTINUE
500      FORMAT(' ','DATAEND')
501      FOPEN(' ',0112)
502      READ(*,*)END
503      END

SUBROUTINE OUTPUT(IMAGE,IP,ICODE)
C
C      OUTPUTS THE MAPPS TO PLOT LOGS
C
      INTEGER,PARAMETER::L=1,241
      DIMENSION ICODE(L)
      COMMON /MAPPS/IMAGE(1:100,1:100),NOUT,NIN,NINP,NINR,NINL,NINR,
     COMMON /MAPPS/LINE(1:100),LXIN,LXINR,LXINL,LXINR,
     WRITE(1,100)
      INT((L+LINE-1)*10)*2
      IP=1,IP1=IP
      LYOUT=LINE*2
      LYOUTR=LINE,LYOUT,LXOUT,LXOUTR
      WRITE(1,101)LYOUT,LYOUTR,LXOUT,LXOUTR,LXOUT,LXOUTR
      WRITE(1,102)LYOUT,LYOUTR,LXOUT,LXOUTR,LXOUT,LXOUTR
      ISUM=0
      DO 301 I=1,LINE
      DO 301 J=1,LINE
      ISUM=ISUM+ICODE(I,J)
301      CONTINUE
300      CONTINUE
      LX=LXIN,LY=LYIN
      IAVG=LINE/2+1
      WRITE(1,103)IAVG
      WRITE(1,104)IAVG
      LY=LYIN
      WRITE(1,105)LY,LYOUT
      N=N+1
      DO 1 J=1,LINE,2
      WRITE(6,106)(ICODE(1,J),J=NIE,NOUT,2)
      IF (N.IE.5) GO TO 190
      WRITE(6,107)
      WRITE(6,108)
      WRITE(6,109)
      IF (N.IE.5) GO TO 1
      N=0
1      CONTINUE
      WRITE(6,105)
      WRITE(6,2000)
      NIN=NIN+50
      NOUT=NOUT+50
      LX=LXIN/NIN-1
      IF (NIN.LT.LINX) GO TO 200
      IF (NIN.GT.LINX) GO TO 201
      NOUT=LINE
      GO TO 200
201      WRITE(6,2000)
2000      FORMAT(1I1)
100      FORMAT(' ','IMAGE TIME=',16,'IMAGE NUMBER=',16/' ','START LINE=',16,
     X6,'END LINE=',16,'START ELEMENT=',16,'END ELEMENT=',16/' ','OUTPUT
     X X POINTS=',16,'OUTPUT Y POINTS=',16)
101      FORMAT(' ','LOWER LEFT HAND X=',16,'LOWER LEFT HAND Y=',16,'ADD X=
     X',16,'ADD Y=',16)
103      FORMAT(' ','INITIAL POINT IN SATELLITE DATA CORRESPONDS TO X=',16,
     X'Y=',16,'IN RADAR GRID')
102      FORMAT(' ',26I9)

```


VITA

Rodney S. Henderson was born in Fort, , Oklahoma, 11 May, 1947, to Thomas Tracy and Anna (Kerr) Henderson. He graduated from Campbell High School in 1965, the equivalent of the eighth grade of Technology, and graduated with a Bachelor of Technology in Electrical degree in June 1970.

Rod was commissioned a 2nd Lt. in the USAF in July 1970 and entered the Basic Military Pilot course at the Air Academy at Oklahoma City. Subsequently, he spent time in the USAF Photo Division, factories at Hamilton AFB, California, and Tinker AFB, Oklahoma, performing duty with the 54th and 366th Weather Reconnaissance Squadrons at Anderson AFB and Keesler AFB, respectively. Rod also served as an augmentee to the 91st Weather Reconnaissance Group (Reserve) while stationed at Keesler AFB.

In September 1974 Rod entered Texas Tech University to pursue a Master of Science degree in Meteorology under Air Force Institute of Technology sponsorship. His permanent mailing address is in care of his sister at 2642 Highland Avenue, Smyrna, Georgia, 30086.

Rod Henderson is married to the former Sandra Leggins of Marietta, Georgia, and has two sons, Bryan and Jeremy.

